A High Resolution Study of the Structure and Mass of Rhenium-190

by

Mark Richard Griffiths

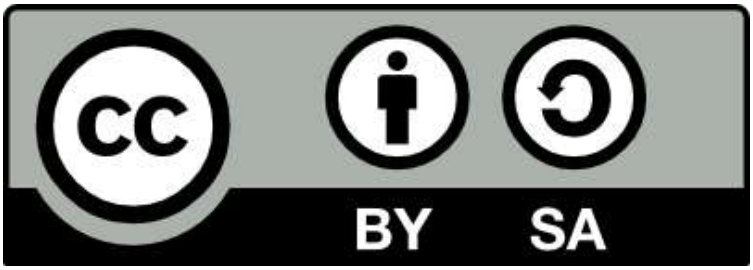


A thesis submitted to
The University of Birmingham
for the degree of
Doctor of Philosophy

School of Physics and Astronomy
College of Engineering and Physical Sciences
University of Birmingham
United Kingdom
May 2023

UNIVERSITY OF BIRMINGHAM

University of Birmingham Research Archive
e-theses repository



This unpublished thesis/dissertation is under a Creative Commons Attribution-ShareAlike 4.0 International (CC BY-SA 4.0) licence.

You are free to:

Share — copy and redistribute the material in any medium or format

Adapt — remix, transform, and build upon the material for any purpose, even commercially.

The licensor cannot revoke these freedoms as long as you follow the license terms.

Under the following terms:



Attribution — You must give appropriate credit, provide a link to the license, and indicate if changes were made. You may do so in any reasonable manner, but not in any way that suggests the licensor endorses you or your use.



ShareAlike — If you remix, transform, or build upon the material, you must distribute your contributions under the same license as the original.

No additional restrictions — You may not apply legal terms or technological measures that legally restrict others from doing anything the license permits.

Notices:

You do not have to comply with the license for elements of the material in the public domain or where your use is permitted by an applicable exception or limitation.

No warranties are given. The license may not give you all of the permissions necessary for your intended use. For example, other rights such as publicity, privacy, or moral rights may limit how you use the material.

Unless otherwise stated, any material in this thesis/dissertation that is cited to a third party source is not included in the terms of this licence. Please refer to the original source(s) for licencing conditions of any quotes, images or other material cited to a third party.

Abstract

The study of neutron-rich isotopes in the $A \approx 170$ - 190 region of the nuclear chart is of interest due to their production in nuclear astrophysical processes, such as the rapid-neutron capture process, as well as due to this region containing large numbers of metastable nuclear isomers. In this thesis, a study of the structure of such an isotope, Rhenium-190, is detailed. An experiment was performed using the Q3D magnetic spectrograph at the Maier-Leibnitz Laboratory (MLL) in Munich with the objectives of reducing the uncertainty in the atomic mass and analysing the nuclear energy levels of this isotope. This was achieved using the $^{192}\mathrm{Os}(\vec{d},\alpha)^{190}\mathrm{Re}$ reaction. The results demonstrate a reduction of the uncertainty of both the atomic mass and mass excess of ^{190}Re from $\pm\,70\,\mathrm{keV}$ to $\pm\,5\,\mathrm{keV}$. The energy of 57 states in the energy-level structure of ^{190}Re were determined and are presented, although spin and parity configurations for these states could not confidently be assigned. This thesis also presents the design and results of an experiment investigating the properties of the positron and positronium, a bound state of a positron and an electron, for use in undergraduate laboratories. The results of this experiment matches theory and the set-up has subsequently been used as part of the third year undergraduate nuclear laboratory at the University of Birmingham.

Dedicated to my parents, Christine and John Griffiths, for always believing in me and pushing me to do my best.

Acknowledgements

This thesis and the work that has gone into it would not have been possible if it were not for the help and support of so many people I have been privileged to have had in my life over these past few years. Firstly I want to thank both Carl and Tzany for believing in me and giving me the opportunity to do a PhD, something that has been a goal of mine for a long time, and also for their supervision and support throughout. Thank you too to Neil, Garry, Martin, Tony and various other members of the nuclear group not only for their academic advice and support, but also for making the group a pleasant place to work.

Thank you to everyone I have had the pleasure of sharing the nuclear group PhD office with: Emzo, Tony, Yiming, Ollie, Jakub, Stuart, Simone, Pedro, Beckie, Håkan, Ross, Angus, Sammy, Dawid, Stephen, Filippo, Kiran and of course the fourth-year gatecrashers Alex, Lucy, Cat, Max, Miriam/Mizza, Lewis, Morgan and Grace. Thank you too to my non-nuclear PhD pals Suzie and Chris, your support and friendship is and always will be greatly appreciated.

Thank you also goes to everyone who worked on the experiment at the Maier-Leibnitz Laboratory in Munich for providing me with some excellent data to analyse (without which I would have had very little to do during the pandemic!). In particular, thank you to Ralf Hertenberger for his clear and helpful responses to my questions about the experimental set-up, without which some of my analysis would have been a non-starter. Thanks also goes to Natasha Timofeyuk for her support and advice regarding my distorted-wave Born approximation calculations.

Thank you to all of my friends, both from home in Nottingham and also to those I met during my undergraduate studies in Birmingham (a special shout-out to all of the 27 Croydon Road crew). The times we have spent together have helped me through some of the toughest parts of my studies and your emotional support has been invaluable.

A huge thank you goes to my partner Emma who has been by my side throughout all my highs and lows, and who's support and belief in me has never faltered, even when I lost that belief myself. You always know how to calm me down and get me back on track and I can't ever thank you enough for that. Thank you too for taking care of our two guinea pigs, Ada and Rosa, who get their own dedication for being a never-ending source of happiness and contentment in my life.

A final thank you goes to my whole extended family, who have helped shaped me into the person I am today (which I would like to think is a good thing!). Special thanks goes to my parents, John and Christine, and my brother Steven. You have always been there for me and pushed me to make the most of my talents and achieve my goals. I hope that you are proud of me, just as I am proud to call you my parents and my brother.

"*Embrace it. Relish it. Try to thrive off it. Just because it is my most difficult challenge does not mean it is not a positive one.*"
- Steve Cooper

Contents

1 Introduction **1**

1.1 Thesis Work 3

2 Background and Theoretical Overview **6**

2.1 Nuclear Structure 7

2.1.1 Nuclear Shell Model 7

2.1.2 Isomeric Nuclear States 13

2.1.3 Binding Energy and Mass Excess 16

2.1.4 The Semi-Empirical Mass Formula 19

2.1.5 The Nilsson Model 23

2.2 Nuclear Reactions 27

2.2.1 Cross Sections 29

2.2.2 Analysing Powers 30

2.2.3 Optical Models 31

2.2.4 The Distorted-Wave Born Approximation 32

2.3 Nuclear Astrophysics 34

2.3.1 The Rapid Neutron-Capture Process 36

2.3.2 Isomers in an Astrophysical Context 40

3 Review of Current Literature on Rhenium-190 **41**

3.1 Historical Overview 41

3.1.1 Level-Structure 41

3.1.2 Atomic Mass and Binding Energy 46

3.2 Recent Studies and Future Outlook 47

4 Experimental Details **51**

4.1 Experimental Requirements and Observables 51

4.2 Instrumentation and Set-up 54

4.2.1 Ion Production and Acceleration 55

4.2.2 Q3D Magnetic Spectrograph . . . 57
4.2.3 Focal-Plane Detector . . . 59
4.3 Run Information . . . 60
4.4 Data Analysis . . . 63
4.4.1 Event Selection . . . 63
4.4.2 Energy Calibration . . . 67
4.4.3 Energy Spectra of Rhenium-190 . . . 70

5 Atomic Mass Measurement **75**
5.1 Data Analysis . . . 75
5.1.1 Mass Excess Calculations . . . 75
5.1.2 Kinematics and Recoil Energy . . . 78
5.1.3 Low-Energy Rhenium-190 Structure . . . 80
5.1.4 Combined Spectrum . . . 82
5.2 Results and Discussion . . . 85
5.2.1 Atomic Mass Results . . . 85
5.2.2 Uncertainty Calculations . . . 86
5.3 Discussion and Outcomes . . . 88

6 Energy-Level Structure Investigations **90**
6.1 Excitation Energies . . . 90
6.2 Spin and Parity . . . 97
6.2.1 Experimental Measurements . . . 98
6.2.2 Theoretical Calculations and DWUCK4 . . . 100
6.2.3 Differential Cross Sections and Analysing Powers . . . 104
6.3 Discussion and Outcomes . . . 125

7 Positronium Investigations **126**
7.1 Theoretical Background . . . 126
7.2 Positrons in Aluminium . . . 128
7.2.1 Method . . . 128
7.2.2 Analysis and Results . . . 133

7.3 Ortho-positronium Measurement 135
7.3.1 Method 135
7.3.2 Analysis and Results 136
7.3.3 Improvements and Future Plans 137
7.4 Discussion and Outcomes 139

8 Summary and Conclusions **141**
8.1 Summary and Outlook 141
8.2 Conclusions 144

A Recoil Energy Calculations **146**

B Publications and Presentations **150**

References **156**

List of Figures

2.1 A figure showing the low energy region of the nuclear shell model. Both nuclear shells and sub-shells are shown and labelled. Closed shells, regions where a large gap between shells leads to increased nuclear stability, are shown alongside the magic numbers of nuclei present in each closed shell. 12

2.2 Chart of nuclides showing isomeric states with a half life greater than 100 ns. If multiple isomers exist for a given isotope, only the longest-lived state is shown. Figure taken from reference [9] (figure 2). 14

2.3 A diagram showing oblate (left) and prolate (right) spherical deformations. Figure taken from reference [14]. 16

2.4 Plot showing the measured binding energy per nucleon for a range of stable nuclei. Data taken from reference [17] (table 1). 18

2.5 A figure showing how each additional term in the semi-empirical mass formula improves how the binding energy per nucleon compared to measured data, also shown on the figure. Data taken from references [17, 20] (table 1 and section 11.3 respectively). 22

2.6 A diagram showing the projection of single-particle orbits on the deformation axis, Ω, for different orientations of the angular momentum, j, for a prolate deformed nucleus. Diagram modified from reference [22] (figure 7.2). 24

2.7 A diagram showing how the magnitude of the projection of the angular momentum on the deformation axis, Ω, affects the energies of states for prolate and oblate deformed nuclei. Diagram modified from from reference [5] (figure 5.27). 24

2.8 A diagram showing the energy-level structure of ^{177}Hf. This diagram clearly shows the rotational band structure for the different values of Ω. Figure modified from reference [5] (figure 5.28). 25

2.9 A Nilsson diagram for protons or neutrons showing how the energy of shell model levels varies as a function of the quadrupole deformation parameter ε_2 around the $N = Z = 20$ region. See text for an explanation of the quantum number labels for the orbitals shown on the right of the figure. The shaded numbers highlight regions where energy gaps appear for a given value of N or Z. Figure taken from reference [23]. 26

2.10 Diagram showing an incident beam impinging on a target and an outgoing beam incident on a space that subtends a solid angle of $d\Omega$ at θ,ϕ. Figure adapted from reference [5] (figure 11.6). 29

2.11 Coordinate system for the initial and final states of the $A(a,b)B$ transfer reaction. In this notation, A denotes the target, a the beam, b the ejectile and B the residual nucleus. Figure adapted from reference [34] (figure 14.1). 33

2.12 Chart showing the stable and neutron-rich nuclides. Stable nuclides are coloured in black and magenta (nuclides coloured magenta are produced as a result of a series of beta decays from a nuclide on the r-process path), with unstable nuclides coloured according to their lifetime. Nuclides further from the line of stable isotopes (known as the valley of stability) have shorter lifetimes. The black bars indicate the locations of closed shells due to magic numbers of nucleons. The magenta line in the centre of the chart shows a typical r-process path predicted by calculations. Figure taken from reference [44] (figure 1). 38

2.13 Abundances of heavy elements produced via the r-process and s-process in the solar system, as a function of mass number. Elements of particular interest have been labelled. The values on the y-axis are $12 + log_{10}$ of abundance relative to that of hydrogen. Figure taken from reference [44] (figure 2). 39

3.1 Chart showing the β^- decay scheme of ^{190}W into ^{190}Re. Energies of states and transitions are given in units of keV. Figure taken from reference [55] (page 31). 45
3.2 Diagram showing the energy-level structure of ^{190}Re, including half-lives and decay schemes where known. Energies of states and transitions are given in units of keV. Data taken from reference [55] (page 29). . 49

4.1 Schematic diagram showing a basic overview of the experimental set-up. The value of θ was was set to several angles between 10° and 45° in order to measure data on the differential cross section of the chosen reactions. 54
4.2 Schematic view of a generic tandem Van de Graaff accelerator, where the acceleration is from right to left. Figure adapted from reference [74] (figure 1). 56
4.3 Schematic view of the Q3D magnetic spectrograph with the magnetic components labelled. The path charged particles take through the detector is highlighted in green. Figure taken from reference [76] (figure 1). 58
4.4 Diagram showing how the different components of the Q3D's focal-plane detector are used to detect incoming particles. This diagram shows the detector from above, resulting in the two anode wires in the second proportional counter appearing as a single wire. Figure taken from [78] (figure 2). 60

4.5 Plots showing how charged particles, in this case α-particles, were identified using properties measured by the Q3D magnetic spectrograph. A heat-map colour scheme is used to show intensities, with a colour scale shown beside each plot. Regions (known as "windows") corresponding to α-particles are denoted by red dashed lines. All three plots show the energy loss as measured by the anode wires on the y-axis. On the x-axis is the residual energy measured by the scintillator (a), the energy loss measured by the first anode wire (b) and the position on the focal plane (c). Note that position on the focal plane is proportional to the energy of the detected particle. 64

4.6 Spectra corresponding to the measurement of the energies of α-particle ejectiles from the ^{192}Os(d,α)^{190}Re with different gating applied. No gating was used in spectrum a). In spectrum b), the window corresponding to the residual energy measured by the scintillator of the Q3D was used. For spectrum c), the window corresponding to the energy loss as measured by the first anode wire was added. Spectrum d) was produced using all three windows described in the text. 66

4.7 Plot showing the fitted low-energy region of the ^{192}Ir spectrum. As the detector was used to measure the energy of α-particle ejectiles produced in the ^{194}Pt(d,α)^{192}Ir reaction, a high channel number (and therefore high α-particle energy) corresponds to a low excitation energy for the residual ^{192}Ir nucleus. Each peak is labelled with its corresponding assigned energy in units of keV [70]. The typical uncertainty in the centroid energy of the peaks from the fit is roughly 1 keV. Peaks omitted from the calibration due to comprising several close-lying energy levels are labelled in brackets with energies obtained after calibrating. 68

4.8 Plot showing the energy calibration for the focal-plane detector of the Q3D magnetic spectrograph, with measured data points shown and the calibration parameters given. The second plot gives the residuals of the calibration. 69

4.9 Plot showing the raw low-energy region of the ^{190}Re spectrum. As this is an α-particle ejectile spectrum a high channel number (and therefore high α-particle energy) corresponds to a low excitation energy for the residual ^{190}Re nucleus. 72

4.10 Plot showing the raw low-energy region of the ^{190}Re spectrum, measured with the Q3D magnetic spectrograph placed at 10° and 27° with respect to the beam axis. The spectra have *not* been normalised for the different beam exposures. 73

4.11 Plot showing the raw low-energy region of the ^{190}Re spectrum, measured with the Q3D magnetic spectrograph placed at 27° with respect to the beam axis with spin-up and spin-down deuteron beams used. The spectra have *not* been normalised for the different beam exposures. . 74

5.1 The low energy region of the ^{190}Re spectrum, measured using α-particle ejectiles from the ^{192}Os(d,α)^{190}Re reaction. The rightmost two peaks have been fitted as skewed Gaussians, with the other peaks fitted as standard Gaussians. 82

5.2 Fitted low-energy region of the ^{192}Ir energy spectrum, with the excitation energies of peaks used in the calibration labelled in keV [70, 85] and those omitted due to comprising multiple close-lying resonances labelled in brackets. The plot shows both the ejectile (α-particle) energy and the corresponding channel number for the focal plane detector on the x-axes. Here, a higher value of channel number corresponds to a lower excitation energy since ejectile energy is being measured. The fitted ground-state and first excited-state peaks in ^{190}Re have been overlaid and labelled in red. The position of the ^{192}Ir ground state (found using the calibration) is also indicated, but was not populated due to its $I^{\pi} = 4^{+}$ configuration being incompatible with the ^{194}Pt target ground-state configuration [28]. Figure and caption taken from reference [86]. 84

6.1 Plot showing the updated energy calibration for the focal plane detector of the Q3D magnetic spectrograph, including known energy levels in ^{190}Re. These states have been given energies corresponding to equivalent α-particle ejectile energies for the ^{194}Pt(d,α)^{192}Ir so that they are consistent with the rest of the points in the calibration. The second plot gives the residuals of the calibration. 93

6.2 Plot showing fitted regions of the ^{190}Re spectrum. As the detector was used to measure the energy of α-particle ejectiles produced in the ^{192}Os(d,α)^{Re}Re reaction, a high channel number (and therefore high α-particle energy) corresponds to a low excitation energy for the residual ^{190}Re nucleus. Each peak is labelled with its calibrated energy. Shown are the a) $\sim$0 - 250 keV, b) $\sim$250 - 500 keV, c) $\sim$500 - 750 keV and d) $\sim$750 - 1000 keV regions of the spectrum. 95

6.3 Comparisons between measured data for the differential cross section and analysing power for the $E = 119.12$ keV state in ^{190}Re, produced via the ^{192}Os($\vec{d}$,α)^{190}Re reaction, and theoretical calculations performed using DWUCK4 corresponding to a $J^{\pi} = 3^{-}$ state in the recoil ^{190}Re nucleus. 105

6.4 Differential cross section and analysing power distributions for all observed peaks in the ^{190}Re spectrum. Each set of plots is presented with the energy of the peak given by the calibration. 125

7.1 Decay information for ^{22}Na. Data taken from reference [100] (page 88). 128

7.2 The electronic set-up used in this experiment to set the thresholds on the constant-fraction discriminators. In this set-up Scionix $CeBr_3$ detectors, Ortec 572 amplifiers, Ortec 584 CFDs and Ortec 416A G&DGs were used. Here, HV represents a high-voltage power supply. Preampliers were not used in this set-up. 131

7.3 The electronic set-up used in this experiment. In this set-up Scionix $CeBr_3$ detectors, Ortec 584 CFDs and a single-width Ortec 566 TAC unit were used. Here, HV represents a high-voltage power supply. Preamplifiers were not used in this set-up. 132
7.4 Timing spectrum for the lifetime of positrons within aluminium. The fit, denoted by the red dashed line, is a convolution of a Gaussian with an exponential decay on top of a linear background. 134
7.5 Timing spectrum for the lifetime of ortho-positronium within fumed silica. The fit, denoted by the blue dashed line, is a convolution of a Gaussian with an exponential decay on top of a linear background. . 137

List of Tables

3.1 Theoretical estimates for spin, parity and energies of excited levels below 1 MeV in ^{190}Re, based on the proton and neutron Nilsson configurations. The energies, given in brackets, are in units of keV. Data taken from reference [54] (table 2). 46

3.2 The mass excess, binding energy and atomic mass of ^{190}Re given by all atomic mass evaluations. Here, the unit u refers to an atomic mass unit. 47

4.1 A table showing details for each of the twenty-nine experimental runs performed as part of this study. For each run details of the specific experimental set-up and properties of the beam are given. Red and blue rows have been used to easily distinguish runs corresponding to the production of ^{190}Re and ^{192}Ir respectively, with lighter to darker shades of each colour corresponding to no beam polarisation, a spin-down beam and a spin-up beam. 62

4.2 Details of the experimental runs combined in order to study the energy-level structure of ^{190}Re. 71

5.1 Values used to calculate the mass excess of ^{190}Re using equation 5.5. The value for ΔQ_{IrRe} was found in this experiment, with the mass excess values taken from reference [64]. These values are unchanged in the most up to date atomic mass evaluation [87]. 85

5.2 Properties of ^{190}Re calculated using the results of this experiment [86], shown alongside known literature values from reference [64]. These values are unchanged in the most recent atomic mass evaluation [87]. 86

6.1 Table showing the measured energy levels in ^{190}Re and the corresponding channel numbers from the fit of figure 6.2. The calibration used to convert between these values is shown in figure 6.1. 96

6.2 The relation between spin/parity (J^π) configurations of states in ^{190}Re and allowed L transfers in the ^{192}Os($\vec{d}$,α)^{190}Re reaction. Here, states of natural parity are populated by the $L = J$ transfer and states of unnatural parity are populated by both the $L = J + 1$ and $L = J - 1$ transfers. 101

6.3 Optical model parameters provided to DWUCK4 in order to calculate observables for the ^{192}Os($\vec{d}$,α)^{190}Re reaction using DWBA calculations. The parameters for the incoming d + ^{192}Os channel and bound d + ^{190}Re state are taken from reference [91] with the parameters for the outgoing α + ^{190}Re channel taken from reference [92]. 103

A.1 Table showing how calculations for the recoil energy of the ^{190}Re nucleus vary over the literature range of atomic masses for ^{190}Re prior to this study. The previous centroid literature value for ^{190}Re [64] is shown in bold. 148

Chapter 1

Introduction

One of the main goals of research in physics is to better understand and explain the world around us, both on a microscopic and macroscopic scale, and to use this knowledge to advance and improve society. This requires researchers with a wide range of expertise to collaborate and work together, from theoretical physicists developing ab-initio theories aiming to describe physical systems from a fundamental level, to experimental physicists making observations in order to gather evidence for theories and change the way problems are approached. All of this work can be combined in order to explain and understand the universe to a greater degree, as well as produce devices and techniques to solve a wide variety of real world problems. This is particularly true in the field of nuclear physics.

Nuclear physics concerns the study of the atomic nuclei which lie at the centre of every atom. Although the nucleus is around five orders of magnitude smaller than the atom itself, the nucleus contributes over 99% of the atomic mass. Atomic nuclei comprise protons and neutrons (collectively known as nucleons) which can exhibit both independent and collective behaviour. This behaviour determines the properties of nuclei as a whole, such as their structure and stability. Although protons and neutrons are not fundamental particles, in turn comprising quarks and gluons, in low-energy nuclear physics studies they are treated as such.

The study of nuclear physics is important for a variety of reasons. On a more general scale it plays a large role in both modern energy production and medicine, two fields that are vitally important to a society facing a global-warming crisis with a growing and aging population putting increased demand on healthcare services. To drive progress in these areas forward research of the more fundamental areas of the field, such as the form of the nuclear (strong) force which holds nuclei together and determines their shape, is important. Nuclear physics is also important from a more purely curiosity-driven standpoint, satisfying the human desire to know more about the world around us. Improved knowledge of certain nuclei can improve understanding of the astrophysical processes which formed the universe as it is today. This in turn can be used to explain the abundances of the elements and isotopes that have been observed by astrophysicists.

It is also important to know the properties of different nuclei to a high degree of precision. Nuclei are complex and producing a model which accurately describes their properties, such as their energy levels and mass, has been at the forefront of nuclear research for decades. Although there have been many great advances through the years due to the work of several exceptional scientists, there are always improvements to be made. As previously mentioned, experimental observations (new observations and improvements on previous measurements as fields advance) are key when investigating theoretical models as they can reveal shortcomings in the theory, as well as highlighting areas that are particularly well explained by certain

models. This makes experimental observations an extremely powerful tool not just in nuclear physics, but across all areas of physics and science as a whole.

1.1 Thesis Work

The first part of this thesis details an investigation into the atomic mass and excited states in the structure of the isotope ^{190}Re, which contains 75 protons and 115 neutrons. Nuclei with an unusually high number of neutrons, such as ^{190}Re, are of particular interest due to their role in astrophysical processes that occur in exotic parts of the universe such as neutron stars and supernovae. Better understanding the properties of such nuclei improves understanding of their role in these processes, leading to improvements in astrophysical models and of our understanding of the isotopic abundances arising from such processes. The aim of this experiment was to improve measurements of the properties of ^{190}Re to the level required for improvement of astrophysical models.

It is known that nuclei in the $A \simeq$ 170-190 region of the nuclear chart, that is to say nuclei with a combined number of protons and neutrons between 170 and 190, exhibit a large number of excited states that demonstrate increased stability and therefore lifetime. Knowledge of these metastable nuclear states, known as isomeric states, is also important for astrophysical models as their increased lifetime can affect the rate of astrophysical processes. If such long-lived states do participate and have an effect, they are known as astrophysical waiting points. As ^{190}Re lies in the $A \simeq$ 170-190 region of the nuclear chart and has already been observed to

have at least one isomeric state, further study into its structure may elucidate further isomeric states and improve knowledge of the structure of the currently known state.

The study of ^{190}Re is also important from a nuclear data point of view. The properties of nuclei in the same regions of the Segre chart are interrelated, so an improvement in the measurement of one property of a certain isotope may lead to a reduction in the uncertainty of properties of other nuclei. For example, a reduction in the uncertainty of the mass of a particular isotope may lead to a reduction in the uncertainty of the Q-value (the amount of energy absorbed or released during a nuclear reaction) of reactions involving that isotope. Subsequently, studies involving these reactions can utilise these more accurate values.

In order to study the atomic mass and energy of excited states in the structure of the isotope ^{190}Re, an experiment was performed at the Maier-Leibnitz Laboratory in Munich. A beam of vector polarised deuterons, produced using a tandem Van de Graaff accelerator, was produced incident on a target of ^{192}Os in order to induce the ^{192}Os($\vec{d}$,α)^{190}Re reaction. The α particle ejectiles emitted were then subsequently detected at various angles by the Q3D magnetic spectrograph in order to observe their energy spectra. These spectra were subsequently used to investigate the properties of ^{190}Re. Polarised deuterons were used in order to investigate the spin and parity of excited states in ^{190}Re.

This thesis also details a secondary project investigating the properties of the positron and positronium, an exotic atomic formed by a positron and an electron orbiting each other. This project was undertaken during the COVID-19 pandemic in order to gain experience designing and subsequently improving an experimental set-up. The project was performed using equipment commonly found in an undergraduate nuclear physics laboratory with the idea that, should the project be successful, it would be offered to undergraduate students as part of their studies going forward. The project involved measuring the lifetime of positrons, produced in the β^+ decay of ^{22}Na, in aluminium as well as measuring the lifetime of a spin-aligned bound state, ortho-positronium.

Chapter 2

Background and Theoretical Overview

In the simplest terms, nuclear physics is the study of nuclei and their constituent nucleons, neutrons and protons. Although this initially sounds straightforward, the properties of these nucleons and how they interact with each other quickly becomes complex and theoretically challenging. In nuclear physics there are two main theoretical areas of interest: nuclear structure and nuclear reactions.

Nuclear structure concerns the properties of nuclei (such as their atomic mass, characteristic energy-level structure and shape) in isolation. Determination of these properties can elucidate more information about the nuclear potential and the nuclear force. The study of nuclear reactions investigates the behaviour of nuclei when colliding and interacting with each other. By observing properties of outgoing nuclei involved in nuclear reactions and comparing these results to theoretical calculations it is possible to better understand the structure of the nuclei involved and the processes by which they interact with each other. Studies of nuclear reactions can be extended and applied beyond earth, and this has led to the field of nuclear astrophysics. Much of the theoretical work in nuclear astrophysics involves modelling the nuclear reactions that occur in a wide range of different cosmic environments. These models can be used to explain the formation of astrophysical

objects and the abundances of different nuclei observed in the universe. In this section an overview of these fields will be given, with a particular focus on areas relevant to the experimental work detailed in chapter 4.

2.1 Nuclear Structure

As previously mentioned, studies of the nuclear structure can be used to further develop theoretical knowledge of both the nuclear potential and nuclear force. Different forms of the nuclear force will lead to different nuclear structures being energetically favourable, yielding information about the nuclear potential and subsequently models use this potential as their basis. By comparing theoretical predictions of these models using current nuclear potential and nuclear force theories with experimental observations, these theories can be expanded and improved upon.

2.1.1 Nuclear Shell Model

By treating each nucleon as being in an effective potential well generated by the nucleon-nucleon interactions of all other nucleons, energy eigenvalues of the Schrödinger equation lead to the formation of a nuclear shell structure, analogous to the structure exhibited by atomic electrons (albeit, the interactions between nucleons are more complicated than those between electrons). The nuclear shell model is a key theory of nuclear physics, as it provides an explanation for the well-defined energy levels exhibited by nucleons.

Nucleons (protons and neutrons) are composed of three quarks bound together by

gluons, the gauge bosons which mediate the strong force. Quarks are spin-$\frac{1}{2}$ particles which, by definition, implies that they are fermions. Logically, this means that both types of nucleon are also spin-$\frac{1}{2}$ fermions and therefore obey the Pauli exclusion principle which dictates that two fermions cannot occupy the same quantum state.

Quantum chromodynamics (QCD), the theory behind the interactions of the strong force, is more complex than its electromagnetic equivalent, quantum electrodynamics (QED). This is in part due to the fact that the gluons that mediate the strong force carry colour charge, the property that determines how particles interact with the strong force, whereas the photons which mediate the electromagnetic force do not carry the equivalent electric charge [1]. It is for this reason that modelling interactions within and between nuclei can quickly become very complex.

A common choice for the form of the potential within which the nucleons lie within nuclei, determined by their interaction with neighbouring nucleons, is known as the Woods-Saxon potential. This is given by:

$$V(r) = -\frac{V_0}{1 + \exp\left(\frac{r-R}{a}\right)}, \tag{2.1}$$

where r is the distance between the nucleon and the centre of the nucleus, V_0 is the depth of the potential well, R is the mean radius of the nucleus (usually taken as $R = r_0 A^{1/3}$ where $r_0 \approx 1.3\,\text{fm}$) and a is the diffuseness parameter, describing the thickness of the surface of the nucleus [2]. The parameter a is proportional to the distance over which the potential drops from 90% to 10% of the central value,

V_0. Units can vary as long as they are consistent, but V and V_0 are commonly in units of MeV and r, R and a in units of fm. This method of using an average potential produced by all other nucleons to describe the forces acting on a single nucleon is known as the mean-field approximation and results in the nucleus taking on a spherical form [3].

According to the Pauli Exclusion Principle, nucleons cannot all fill the lowest energy state in this potential as they would be in the same quantum state, which is forbidden. Instead, nucleons fill the potential in a series of discrete levels, giving rise to the nuclear shell structure. As protons and neutrons are distinguishable particles due to their differing quark content (*up-up-down* for protons and *up-down-down* for neutrons), both protons and neutrons have their own, independent shell structure.

Initially, the shells fill in order of orbital angular momentum, l, with spectroscopic notation being used so that $l = 0, 1, 2, 3...$ corresponds to shells $s, p, d, f...$ respectively. For each shell the orbital angular momentum label is preceded by a number, n, analogous to the principal quantum number in the atomic shell model. However, this number is not the principal quantum number, it can be thought of as a counter of the number of shells possessing a particular l value, but corresponds to the number of nodes in the radial part of the wave function. Therefore, there is no limitation that $l \leq (n-1)$ as in the atomic shell model. This leads to the lowest energy orbital being the $1s$ shell, followed by $1p$, $1d$, $2s$ etc.

Within shells, nucleons can arrange themselves in a manner that means several nucleons can occupy a single orbital while still obeying the Pauli exclusion principle. Firstly, there is degeneracy due to the projection of the orbital angular momentum, m_l. This can take integer values in the range $-l \leq m_l \leq l$, including zero, increasing the degeneracy of a given orbital to $2l + 1$. As each nucleon has spin of $s = \frac{1}{2}$, the projection of this spin can be in either the spin up ($m_s = +\frac{1}{2}$) or spin down ($m_s = -\frac{1}{2}$) configuration. This adds a factor of two to the degeneracy, making the maximum occupancy of each orbital $2(2l + 1)$. This model agrees with the first three observed 'magic numbers' ($2, 8$ and 20) but does not match the magic numbers observed at higher nucleon numbers. These magic numbers correspond to the number of nuclei required to form a closed shell. The energy gaps from these closed shells to the next shell are particularly large, leading to nuclei with a magic number of protons or neutrons exhibiting increased stability from closed shell structure. Some nuclei are 'doubly magic', having a magic number of both neutrons and protons [4]. These numbers have been observed experimentally, with large nucleon separation energies measured for nuclei with magic numbers of the corresponding nucleon, so reproducing these observations is an important test of the shell model. To do so the model must include another manifestation of the nucleon-nucleon force, the spin-orbit interaction.

There is strong experimental evidence for a spin-orbit force between nucleons from scattering experiments [5]. Such a force may cause the shells to split into sub-shells, again analogously to the atomic case where a spin-orbit interaction introduces the

fine structure of spectral lines. Simply put, the spin-orbit interaction takes into account whether the spins of a pair of interacting nucleons are aligned or anti-aligned with their relative orbital motion. For a description of the spin-orbit component, the total angular momentum, given by $\vec{j} = \vec{l} + \vec{s}$ needs to be considered. As the projection of the spin can either be $m_s = +\frac{1}{2}$ or $m_s = -\frac{1}{2}$, this implies that for each value of l there are two possible values for j resulting in each shell splitting into two sub-shells of different energies. Using reasoning similar to that used for the shells, the degeneracy of each sub-shell is given by $2(2j + 1) = 2[2(l + s) + 1]$. Consideration of the spin-orbit interaction alters the shell structure significantly due to the change in energy ordering that occurs for some of the orbitals. These differences alter the position at which some of the closed shells are predicted to form and result in the model accurately predicting a larger number of magic numbers that have been experimentally observed [6]. The first few closed shells of the nuclear shell model are shown in figure 2.1, which also shows how the spin-orbit interaction is used to explain the experimentally observed magic numbers.

Knowledge of these shells is important for experimental nuclear physics as nuclear excitations are often simply when a valence nucleon is given sufficient energy to 'jump' the energy gap to a higher energy shell or sub-shell. Nuclear excitations can also be due to the spin configuration of nucleons changing within the shells or due to collective effects such as rotation and vibration. When the inverse process happens and nucleons de-excite to a lower energy level, the energy difference is often emitted as a gamma ray. Through gamma spectroscopy, this process allows for the gaps

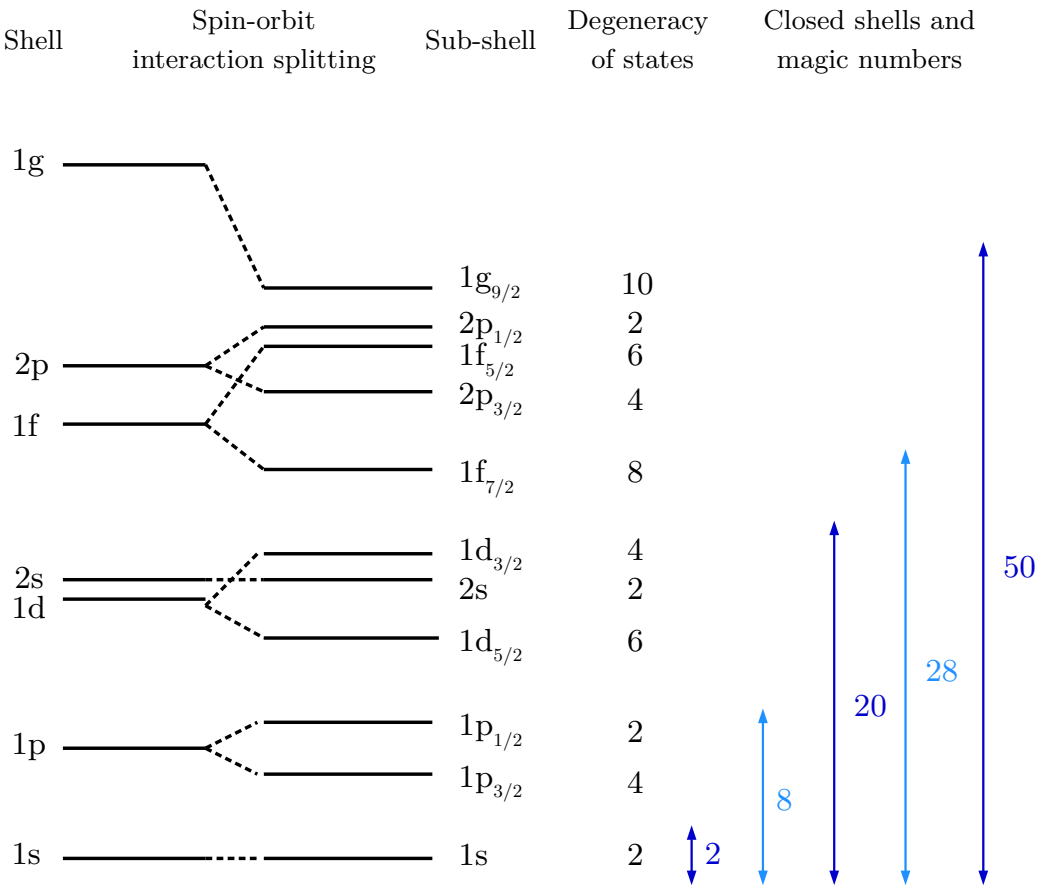


Figure 2.1: A figure showing the low energy region of the nuclear shell model. Both nuclear shells and sub-shells are shown and labelled. Closed shells, regions where a large gap between shells leads to increased nuclear stability, are shown alongside the magic numbers of nuclei present in each closed shell.

between energy levels for different nuclei to be measured, elucidating information about their structure, stability and potentially even atomic mass.

All nuclear states have associated values of spin and parity. The spin relates to the total angular momentum of the unpaired (usually high valence) nucleons within the shell structure. Parity describes how the nuclear wave function behaves under an inversion of spatial coordinates. If it is unchanged by such a transformation,

the parity is even (+) and if its sign changes the parity is odd (−). If all nucleons form anti-aligned spin pairs within the shell structure, as in the ground states of even-even nuclei, then the value for the spin-parity is $I^{\pi} = 0^{+}$ due to the spin and orbital angular momenta of all nucleon pairs cancelling out. If there is a single unpaired nucleon, then this usually determines the spin and parity of the entire nucleus, though exceptions can arise for non-spherical nuclei, for example the case of ^{21}Ne which has an intrinsic reflection-asymmetric structure [7]. In cases with several unpaired nucleons the interaction between these nucleons leads to several possible spin-parity configurations of varying energies, the higher energy cases being excited states. The nuclear shell model is reliable when predicting the spin and parity of ground state nuclei and single nucleon excited states, but is less reliable at predicting the spin and parity of deformed and excited states that involve collective motion, such as vibrations and rotational states, where more complex models that account for the nucleon-nucleon interaction are required [8].

2.1.2 Isomeric Nuclear States

In the most recent NUBASE evaluation, an extensive database of the properties of currently observed nuclides, recommended properties for the ground states of 3340 nuclides are listed. It also contains properties of 1938 metastable excited states, known as isomeric states, with a half-life of 100 ns or greater [9]. The position of these isomers on the chart of nuclides is shown in figure 2.2. In general, states where the lifetime is greater than expected (even if this lifetime is a few ns) are considered isomers, so it could be argued that the number of isomers is even larger.

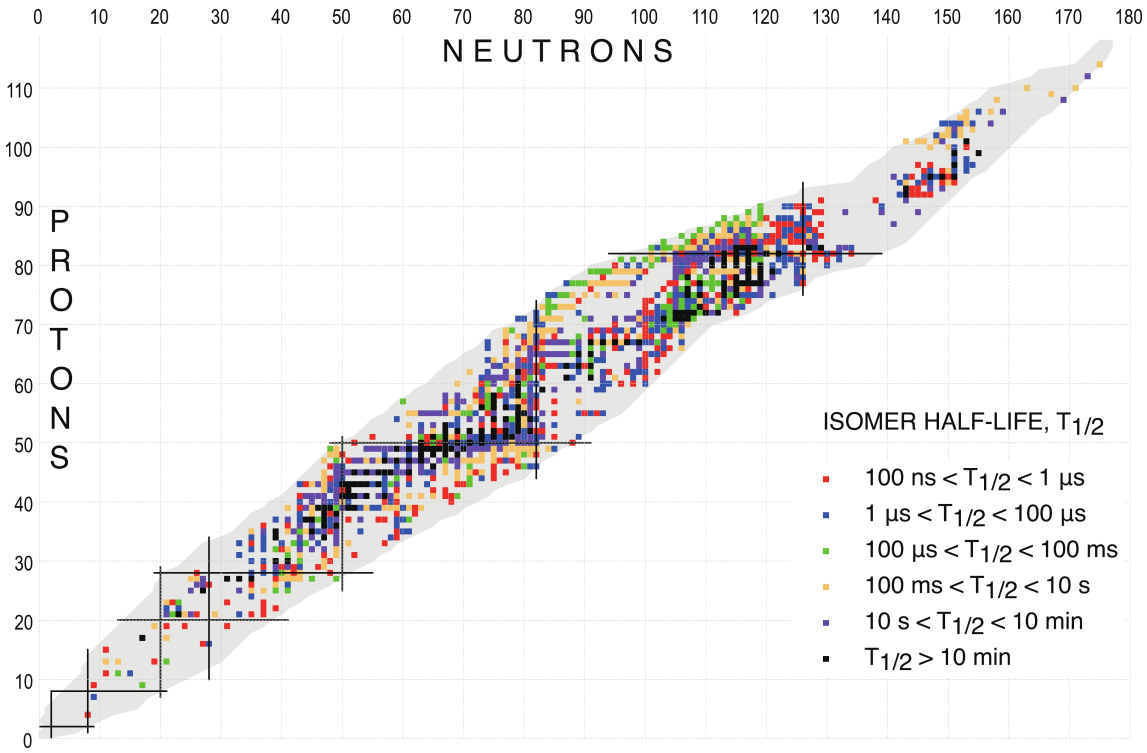


Figure 2.2: Chart of nuclides showing isomeric states with a half life greater than 100 ns. If multiple isomers exist for a given isotope, only the longest-lived state is shown. Figure taken from reference [9] (figure 2).

There are three principal classes of nuclear isomerism: spin isomers, K-isomers and nuclear shape based isomers [10]. Spin isomers, first proposed by von Weizsäcker in 1936 [11], occur when there is a large difference in spin/angular momentum between the isomeric state and all other states of a lower excitation energy. This, along with often low transition energies, leads to suppressed electromagnetic transition rates and therefore increased half-lives for the excited state.

For deformed nuclei, the angular momentum projection on the deformation axis (labelled K) is an approximately conserved quantity. The result of this is the

formation of so called K-isomers, named due to exhibiting a large angular momentum projection along the nuclear deformation axis. These isomers possess large half-lives due to hindered decays from their deformation aligned states to the rotationally aligned structures, discussed in section 2.1.5, of nuclear ground states. The reverse situation, where the ground state is deformation aligned and the isomeric state is rotationally aligned, also leads to the formation of K-isomers as there is still a large difference in the value of K for each state [12]. It is for this reason K-isomers are sometimes referred to as being an orientation effect of the angular momentum vector. Experimentally, large numbers of these K-isomers have been observed in the $A \approx 170$ - 190 region of the nuclide chart due to their large prolate (rugby-ball shaped) deformations coupled with the availability of high-K orbitals by valence nucleons [13]. Prolate and oblate (disk-shaped) quadrupole deformations are shown in figure 2.3. For shape isomers, the increased stability comes from the inhibited transitions due to the associated changes in nuclear shape. These decays require significant changes in the configuration of the nuclei involved, such as changes in a significant number of nucleon orbits.

Nuclear isomers are observed for a wide range of nuclear masses. However, they are not distributed uniformly. Isomers tend to favour nucleon numbers around magic numbers, as can be seen in figure 2.2, but some (mostly K-isomers) can also be seen to group together away from closed shells in regions where nuclei exhibit prolate deformations, as previously mentioned.

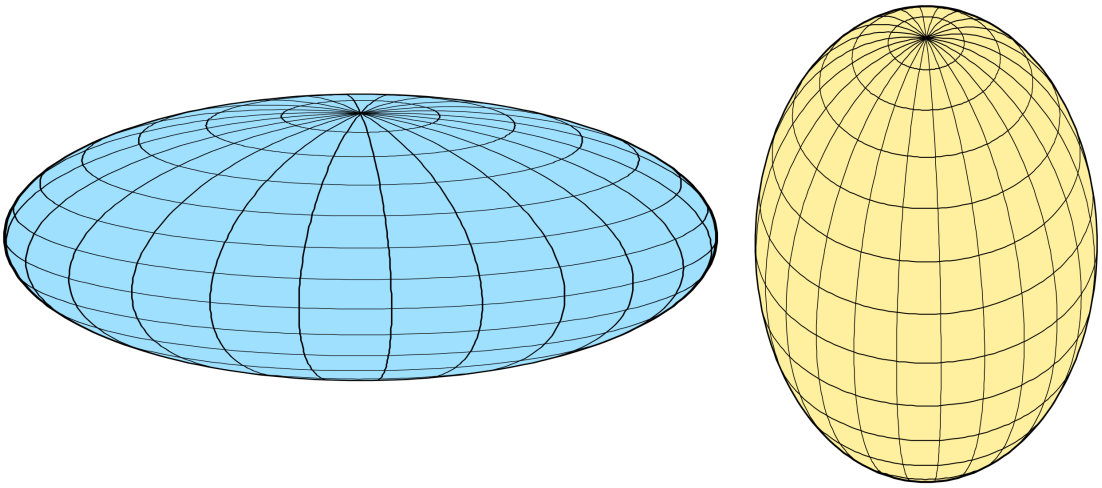


Figure 2.3: A diagram showing oblate (left) and prolate (right) spherical deformations. Figure taken from reference [14].

2.1.3 Binding Energy and Mass Excess

A characteristic property possessed by all nuclei is their binding energy, the energy required to separate the nucleus into its component nucleons. This energy is equivalent, through the mass-energy equivalence principle, to the difference in mass between the individual nucleons and the bound nucleus (the mass defect). Another nuclear property is the mass excess, not to be confused with the mass defect, which is the difference in the measured/calculated mass of a nucleus and its nucleon number in atomic mass units. The atomic mass of a neutral atom with N neutrons and Z protons is

$$m(Z,N) = Nm_n + Zm_H - \frac{1}{c^2}B(N,Z), \tag{2.2}$$

where m_n and m_H are the neutron and hydrogen atomic masses respectively and $B(N,Z)$ is the binding energy of the nucleus [15]. The mass excess is then simply

$$\Delta m(Z, N) = m(Z, N) - Au, \tag{2.3}$$

where u is the value of an atomic mass unit, commonly quoted as $\sim 931.5\,\mathrm{MeV/c^2}$ [5].

As binding energy increases roughly linearly with nucleon number, A, it can be more insightful to observe how the binding energy per nucleon, BE/A, varies with A. The larger the binding energy per nucleon, the more stable a nucleus is as more energy is required to remove a nucleon on average. In figure 2.4 the measured binding energy per nucleon for several nuclei has been plotted. As can be seen, the binding energy per nucleon peaks at an atomic mass number of $A \sim 60$ (specifically ^{62}Ni has the largest binding energy per nucleon, with ^{56}Fe having the lowest mass per nucleon due to a proportionally higher number of protons [16]). The binding energy per nucleon of nuclei with magic numbers of protons and/or neutrons, mentioned in section 2.1.1 is also increased compared to neighbouring non-magic nuclei, reflecting their increased stability.

Knowledge of the binding energy and mass excess of nuclei is important when studying nuclear reactions, which will be discussed further in section 2.2. This is because the binding energy of the reactants and products in a nuclear reaction affect the Q-value of said reaction. The Q-value is simply the amount of energy given off or taken in during a nuclear reaction. A large, positive Q-value suggests that a reaction will readily happen with a high rate where possible, whereas a negative Q-value suggests that a reaction will only happen with a net input of energy into

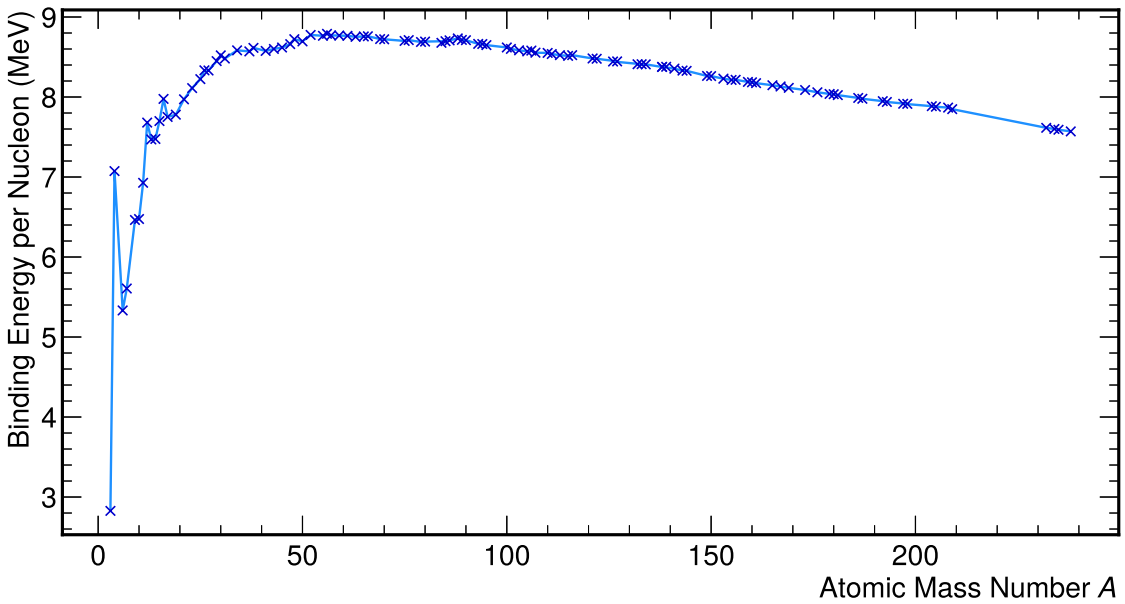


Figure 2.4: Plot showing the measured binding energy per nucleon for a range of stable nuclei. Data taken from reference [17] (table 1).

the system. The relation between the Q-value of a reaction and the mass excesses of the nuclei involved is given by

$$Q = \sum \Delta m_r - \sum \Delta m_p, \tag{2.4}$$

where Δm_r are the mass excesses for the reactants and Δm_p are the mass excesses for the products. Therefore, knowledge of the mass excess of nuclei can improve theoretical knowledge of reactions that these nuclei are involved in. Conversely, studying reactions involving certain nuclei can be used to improve knowledge of its mass excess and, subsequently, binding energy.

2.1.4 The Semi-Empirical Mass Formula

Nuclear models aim to accurately describe the properties of nuclei, such as their binding energy, mass and structure based on their proton and neutron numbers. These nuclear models vary in complexity and accuracy; the more basic models can be used to give approximate atomic masses but may show discrepancies in some areas of the nuclear chart. More involved models consider and account for many-body forces, such as the spin-orbit interaction, which increases their accuracy at the cost of them being more computationally intensive.

One of the more basic, but widely used, nuclear models is the liquid-drop model which was first proposed by George Gamow in 1930 [18]. As the name suggests, it involves treating the nucleus as an incompressible, uniform liquid drop of high density. While crude, this accounts for the nuclear force acting between nucleons and the fact that nucleons on the surface of the nucleus experience this force differently, similar to the effect of surface tension for a liquid drop. Also, the constant binding energy per nucleon in a nucleus is analogous to the concept of latent heat of vaporisation in a fluid. Due to the assumptions made in this model it is most accurate for spherical nuclei, but is less successful at modelling deformed nuclei. This is because the model is empirically motivated and does not make predictions based on underlying knowledge of the nucleon-nucleon force. Therefore, it is most accurate at describing nuclei in the data set that it has been fitted to, and therefore would not be considered a full model by some.

This model, combined with empirical measurements, was used to devise the semi-empirical mass formula (SEMF), also known as the Bethe-Weizsäcker formula, by Carl Friedrich von Weizsäcker in 1935 [19]. The formula can be used to approximate the binding energy, and therefore atomic mass, for nuclei. The formula is as follows:

$$B(Z,N) = a_v A - a_s A^{2/3} - a_c \frac{Z(Z-1)}{A^{1/3}} - a_{sym} \frac{(A-2Z)^2}{A} + \delta, \tag{2.5}$$

$$\delta = \begin{cases} a_p A^{-1/2}, & Z, N \text{ even} \\ 0, & A \text{ odd} \\ -a_p A^{-1/2}, & Z, N \text{ odd}, \end{cases} \tag{2.6}$$

where terms are physically motivated, but the associated constants, a_v, a_s, a_c, a_{sym} and δ, are adjusted to best fit to experimental data [5]. The motivation for each term is as follows:

- The Volume Term - $a_v A$: there is a near-linear relationship between the volume of the nucleus and the number of nucleons it contains. For a roughly equal numbers of protons and neutrons, a reasonable assumption for low mass nuclei, this subsequently leads to a linear increase in binding energy given by this term. This also assumes that, due to the short range of the nuclear force, nucleons only interact with their nearest neighbours. This is also the origin of the $R \sim A^{1/3}$ relationship for the nuclear radius. Assuming a spherical nucleus, its radius will be proportional to the cube root of its volume.

- The Surface Term - $a_s A^{2/3}$: this term is proportional to the surface area of the nucleus. It accounts for nucleons at the surface of the nucleus contributing less to the overall binding energy as they are in close contact with fewer other nucleons.

- The Coulomb Term - $a_c Z(Z-1)A^{-1/3}$: accounts for the fact that there is electrostatic repulsion between the protons and is therefore, the Coulomb self-energy of the nucleus.

- The Symmetry Term - $a_{sym}(A-2Z)^2 A^{-1}$: it is observed that nuclei with the same number of protons and neutrons are more stable than those with differing numbers of protons and neutrons due to the maximal overlap of the nucleon spatial wave functions. The symmetry term accounts for this observation.

- The Pairing Term - δ: spin anti-aligned nucleons can couple pairwise, leading to particularly stable configurations which are accounted for by this term.

The effect of each term in the SEMF is shown in figure 2.5, which shows how the binding energy per nucleon calculated by the SEMF varies with the addition of each subsequent correction and how this compares to experimentally observed data. It is clear that the addition of each successive term improves the accuracy of the SEMF, however the improvements become more subtle with each successive term. There are still some significant discrepancies between experimentally observed values for the binding energy per nucleon and those predicted by the SEMF, particularly at magic numbers (the SEMF does not consider the nuclear shell structure) and at low atomic mass numbers.

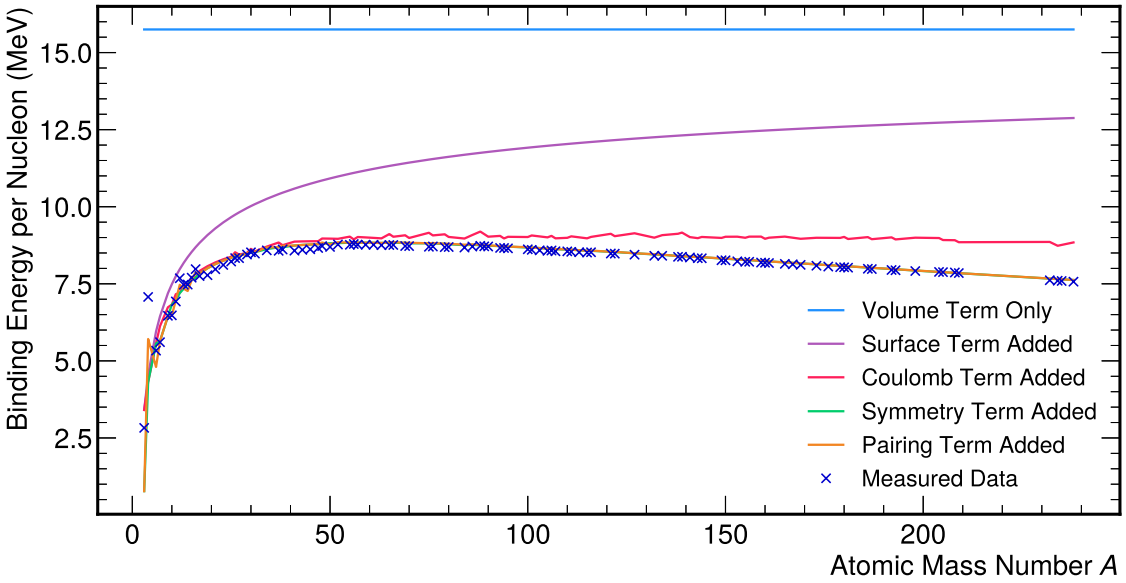


Figure 2.5: A figure showing how each additional term in the semi-empirical mass formula improves how the binding energy per nucleon compared to measured data, also shown on the figure. Data taken from references [17, 20] (table 1 and section 11.3 respectively).

More complex models, such as microscopic-macroscopic (MM) models and purely microscopic models do exist. Microscopic models are often motivated by density functional theory, whereas microscopic-macroscopic models combine macroscopic models (such as the SEMF) with microscopic corrections which account for effects like the nuclear shell structure. An example of one of these models is the Finite-Range Liquid-Drop Model (FRLDM) [21] which combines the macroscopic ideas of the liquid-drop model with microscopic contributions. These models are more accurate than more basic models for a large number of nuclei, but there are still significant discrepancies in some areas of the nuclear chart and many models still rely on fitting parameters to available data rather than starting from fundamental principles.

2.1.5 The Nilsson Model

In the nuclear shell model, calculations of energy levels assume that nuclei are spherical. For most nuclei this is not the case. In particular, those close to stability in the range $150 \leq A \leq 190$ and $A \geq 230$ are better represented as rotational ellipsoids [5]. Logically, when the nuclear shape is non-spherical a deformed potential should also be used. This leads to the angular momentum, l, no longer being a 'good' quantum number. A new quantum number is needed that gives the projection of the overall angular momentum of a single particle on the symmetry axis of the deformation. This projection is denoted by Ω and is shown pictorially in figure 2.6 for a prolate deformation.

The energy levels can be understood by examining the deformation and this angular momentum projection. For prolate nuclei, a particle in an orbit with a small angular momentum projection on the deformation axis (a small Ω value) will spend a greater amount of time closer to the centre of the nucleus. This results in a greater binding energy and therefore a lower excitation energy. Conversely, a particle in an orbit with a large Ω value will spend less time close to the centre of the nucleus and therefore will exhibit a higher excitation energy. This is reversed for oblate nuclei, with a large value of Ω corresponding to a lower excitation energy and vice-versa. This effect is shown in figure 2.7.

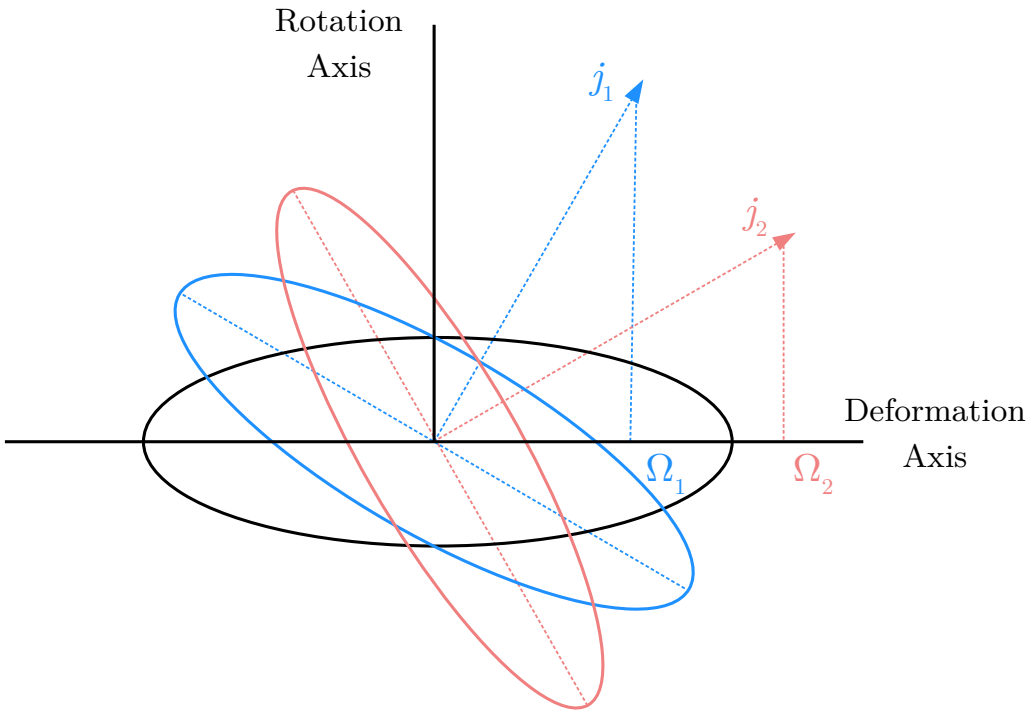


Figure 2.6: A diagram showing the projection of single-particle orbits on the deformation axis, Ω, for different orientations of the angular momentum, j, for a prolate deformed nucleus. Diagram modified from reference [22] (figure 7.2).

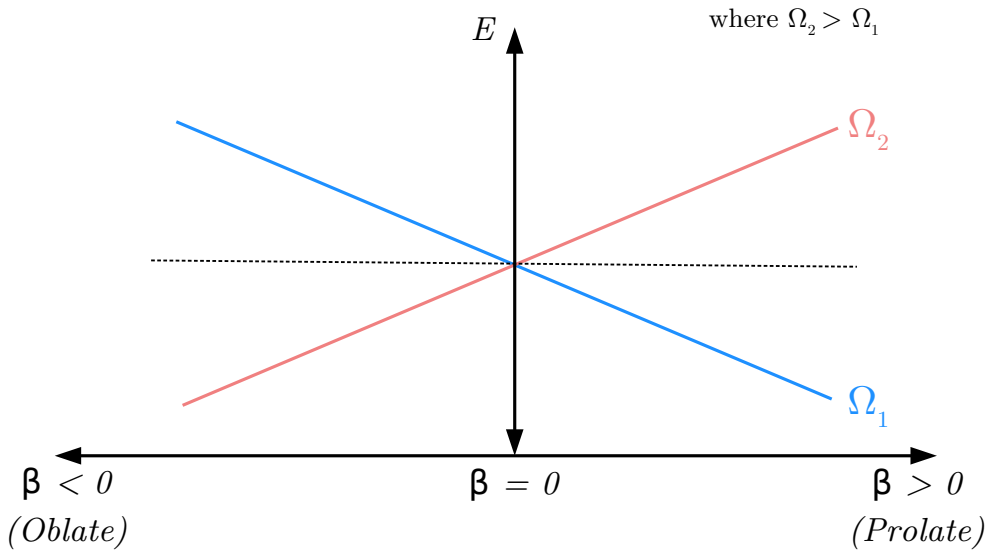


Figure 2.7: A diagram showing how the magnitude of the projection of the angular momentum on the deformation axis, Ω, affects the energies of states for prolate and oblate deformed nuclei. Diagram modified from from reference [5] (figure 5.27).

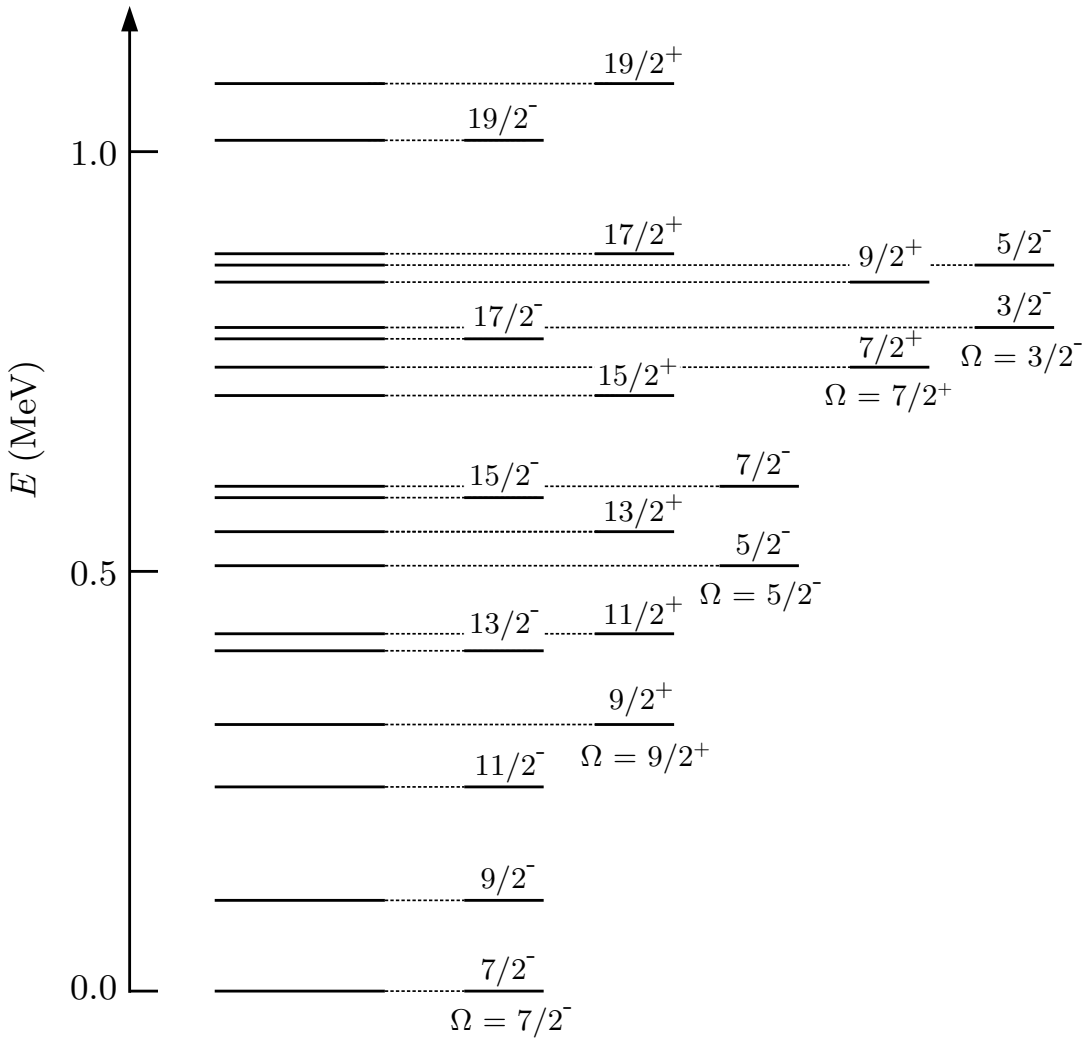


Figure 2.8: A diagram showing the energy-level structure of ^{177}Hf. This diagram clearly shows the rotational band structure for the different values of Ω. Figure modified from reference [5] (figure 5.28).

In the Nilsson model it is possible for more than one j configuration to contribute to the same value of Ω. States will exist as long as $j \geq \Omega$; this ensures that sub-states will exist where $m_j = \Omega$. An example of this is shown in figure 2.8, where rotational bands of states with the same values of Ω but differing values of j can be observed. These rotational bands typically begin at at a 'band-head' where $j = \Omega$ and the ith member of the band has $j = \Omega + i$ [5].

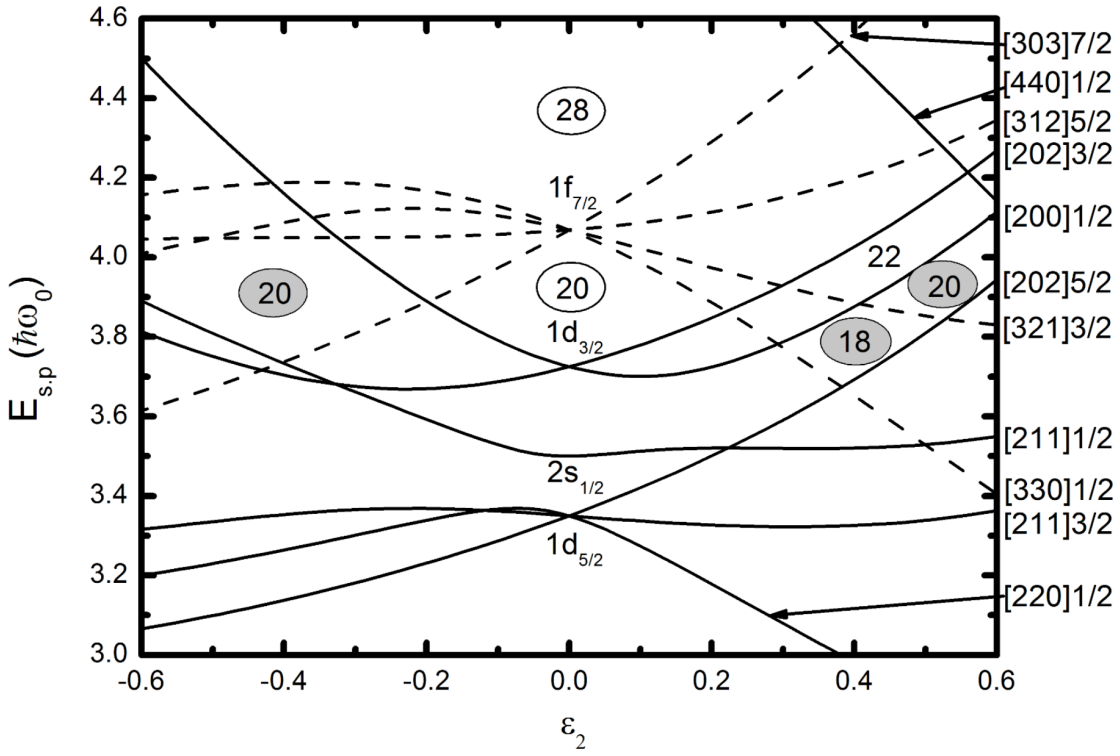


Figure 2.9: A Nilsson diagram for protons or neutrons showing how the energy of shell model levels varies as a function of the quadrupole deformation parameter ε_2 around the $N = Z = 20$ region. See text for an explanation of the quantum number labels for the orbitals shown on the right of the figure. The shaded numbers highlight regions where energy gaps appear for a given value of N or Z. Figure taken from reference [23].

When using the Nilsson model, the quantum numbers used to describe states are sometimes $|N, j, \Omega\rangle$, where j and Ω are previously defined and N is the harmonic oscillator label. However, commonly the notation $[N, n_Z, \Lambda]\Omega$ is used, where n_Z is the number of oscillator shell quanta along the deformation axis and Λ is the projection of the orbital angular momentum, l, onto the deformation axis. In more modern notation, Ω is often put before the square brackets rather than after. These are known as the asymptotic quantum numbers as they are often used for large deformations where use of the (n, l, j, Ω) quantum numbers is invalid [24]. A

Nilsson diagram, used to show how the energy of shell model levels varies for a deformed nucleus as a function of the quadrupole deformation parameter ε_2, using the $[N, N_Z, \Lambda]\Omega$ convention is shown in figure 2.9.

2.2 Nuclear Reactions

Nuclear reactions occur when energetic particles (often light nuclei such as protons, neutrons, deuterons and so on) interact with target nucleus. Such reactions can be expressed in two ways:

$$a + A \rightarrow B + b,$$

$$A(a, b)B,$$

where a is the energetic particle and A the target. It follows that b and B are the products of the reaction, with b often being a light ejectile and B a heavier residual nucleus that remains within the target. This notation is useful as it can be applied to a wide range of nuclear reactions. If the incident and outgoing particles are the same ($a = b$ and $A = B$) then the reaction is a scattering process. If b and B are produced in their ground state the reaction is elastic, but if either is produced in an excited state the reaction is inelastic [5]. If b is a gamma ray the reaction is classified as radiative capture, and if a is a gamma ray it is known as the nuclear photoeffect or photo-disintegration. There are also break-up reactions, where the projectile breaks up into two or more fragments on interaction with the target, resulting in a final state of three or more nuclei [25].

Another type of reaction, known as a transfer reaction, involves nucleons being transferred between the projectile and the target, for example an incident deuteron transferring a neutron onto a target resulting in a proton ejectile, such as in the $^{90}\mathrm{Zr}(d,p)^{91}\mathrm{Zr}$ reaction [26]. Transfer reactions are commonly used as a means to extract information about excited states in nuclei. Typically, to study nuclei via transfer reactions in the laboratory, stable beams are used to bombard a target foil resulting in ejectile particles being emitted. In these reactions, only a small number of nucleons take part in the reaction with the rest acting as passive observers and the interaction between nuclei is sufficiently weak to be treated as a first order perturbation. These are known as direct reactions, of which transfer reactions are a specific case.

The opposite case is compound reactions where an intermediate, compound nucleus is formed composed of the target and projectile nuclei. This intermediate state exists for a sufficient amount of time such that the energy from the original reaction is shared between all the constituents of the compound system and therefore the state is independent of the incoming channel [27]. Subsequently, one or more nucleons, or clusters of nucleons are ejected from the compound nucleus leaving behind a residual nucleus.

2.2.1 Cross Sections

Nuclear cross sections can be thought of as the 'effective area' presented by a target nucleus to an incoming projectile, where the larger the cross section, the more likely that the reaction will occur. For a given reaction the cross section depends on a variety of properties, notably the energy of the incoming particle and the structure of nuclei involved in the reaction. Cross sections are usually given in units of barns (b), where $1\,\mathrm{b} = 10^{-28}\,\mathrm{m}^2$, as values for common nuclear reactions are often around this order of magnitude.

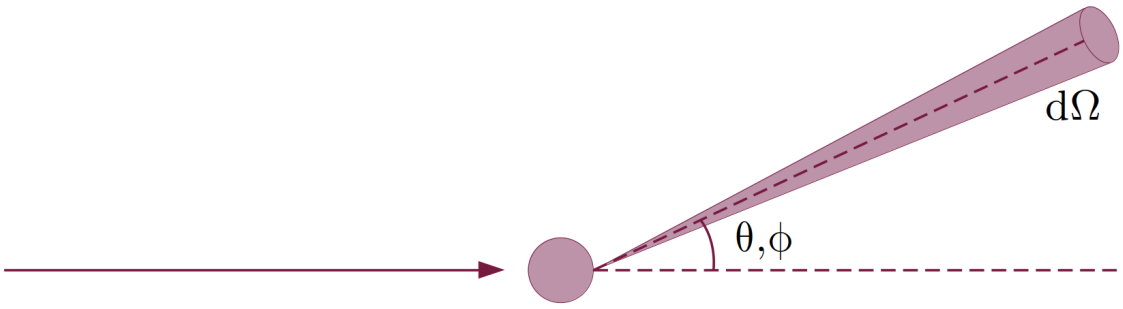


Figure 2.10: Diagram showing an incident beam impinging on a target and an outgoing beam incident on a space that subtends a solid angle of $d\Omega$ at θ,ϕ. Figure adapted from reference [5] (figure 11.6).

In nuclear physics experiments it is common that detectors do not cover all of the 3D-space around a reaction centre, only subtending a small solid angle $d\Omega$ as shown in figure 2.10. For situations like this it can be more useful to use the differential cross section, $d\sigma/d\Omega$, which gives the probability of an interaction occurring where the outgoing particle is emitted within the solid angle $d\Omega$. This value varies as θ and ϕ (the polar and azimuthal angles respectively) are varied. Experiments are often

performed in the plane of the beam axis so that $\phi = 0$, resulting in measurements probing how the differential cross section varies with θ. From this, it is possible to deduce information about the structure of nuclei involved in the reaction [28].

The differential cross section can also refer to the cross section where the reaction produces ejectiles of a certain energy rather than ejectiles emitted at a certain angle. If nuclei are detected at a particular angle and their energy is also resolved, then the cross section is doubly differential [29] and written as $d\sigma/(d\Omega dE)$.

2.2.2 Analysing Powers

Use of polarised beams in nuclear physics experiments can be used to learn more about the structure of the nuclei involved in the reaction, as some properties of the observables from the reactions are closely related to the spin and parity of these nuclei. One such property is the analysing power, also known as the spin asymmetry, which quantifies changes in the differential cross section when using spin-up and spin-down beams. The vector analysing power is given by

$$A_y(\theta) = \left(\frac{2}{3P_y}\right)\left(\frac{\sigma_+(\theta) - \sigma_-(\theta)}{\sigma_+(\theta) + \sigma_-(\theta)}\right), \tag{2.7}$$

where $\sigma_+(\theta)$ and $\sigma_-(\theta)$ are the measured angular cross sections for the spin-up and spin down beams respectively and P_y is the vector polarisation of the beam [28]. In the coordinate system used here the y-direction is parallel to $\vec{k_i} \times \vec{k_o}$ and the z-direction is $\vec{k_i}$, where $\vec{k_i}$ gives the incident wave vector and $\vec{k_o}$ gives the outgoing wave vector. The analysing power can take a value from 1 to -1, with a positive

value suggesting a greater cross section when the beam is spin-up and the opposite for a spin-down beam. As the values the analysing power takes are largely dependent on the spin and parity of the nuclei involved, measured values for analysing power can be compared to calculated values in order to deduce the spin/parity configurations of nuclei.

2.2.3 Optical Models

The exact mechanisms by which nuclei interact with each other are theoretically complex and challenging. The nuclear optical model simplifies this by representing the interaction using a phenomenological potential with parameters that can be fitted to experimental data. The potential takes the form

$$V(r) = V_R(r) + iV_I(r), \tag{2.8}$$

where $V_R(r)$ and $V_I(r)$ are real functions which can be chosen to give the potential an appropriate radial dependence [30]. It is called the optical model as it is analogous to the treatment of the scattering and absorption of light in a medium with a complex refractive index where the imaginary part of the potential, $iV_I(r)$, accounts for absorption. The real part, $V_R(r)$, accounts for elastic scattering.

The optical model is not just an effective way of modelling the elastic scattering of nuclei, it can also be used to aid the calculation of differential cross sections, discussed in section 2.2.1, for many direct nuclear reactions [31] which can then be compared to experimental results. For this, the parameters of the optical model

potential need to be specified numerically. It is common to start off with initial parameter values that describe a simple, theoretically motivated potential and then compare these with the experimental data in order to optimise them. This analysis has already been performed for a wide range of nuclei and beam energies and therefore suitable starting parameters can readily be found in the literature [32].

2.2.4 The Distorted-Wave Born Approximation

The distorted-wave Born approximation (DWBA) [33] is often used to simplify differential cross section calculations. It works by treating the incoming and outgoing wave functions as plane waves distorted by an optical model potential

Consider a transfer reaction $A(a,b)B$ in which a projectile composed of two clusters, b and v, transfers the cluster v onto target A. This produces the residual nucleus B and ejectile b. The coordinates for this system are shown in figure 2.11. The exact transfer matrix element (used to relate the initial and final states of a physical system) for this system is

$$\mathbf{T}^{\text{exact}}_{\text{prior}} = \langle \Psi^{(-)\text{exact}} | V_{vA} + V_{bA} - U_i | \Phi_{I_b:I_a}(\mathbf{r}_{vb}) \chi_{\mathbf{k}_i}(\mathbf{R}_i) \rangle \,, \tag{2.9}$$

$$\mathbf{T}^{\text{exact}}_{\text{post}} = \langle \Phi_{I_A:I_B}(\mathbf{r}_{vA}) \chi^{(-)}_{\mathbf{k}_f}(\mathbf{R}_f) | V_{vb} + V_{bA} - U_f | \Psi^{(+)\text{exact}} \rangle \,, \tag{2.10}$$

where the post and prior denote whether the Hamiltonian has been expanded using either the final or initial kinetic energy respectively, giving results that are different in appearance but the same in application. Here, $\Psi^{(\pm)\text{exact}}$ are the exact solutions to

the three-body interactions described above, V_{bA} denotes the core-core interaction between b and A and V_{vb} and V_{vA} are the binding potentials corresponding to the entrance and exit channels respectively. The U_i and U_f terms are optical potentials for the entrance and exit channels respectively, $\Phi_{I_b:I_a}$ denotes the overlap function of the spin states I_a and I_b and $\chi_{\mathbf{k}_i}(\mathbf{R}_i)$ and $\chi^{(-)}_{\mathbf{k}_f}(\mathbf{R}_f)$ are the initial and final wave functions [34].

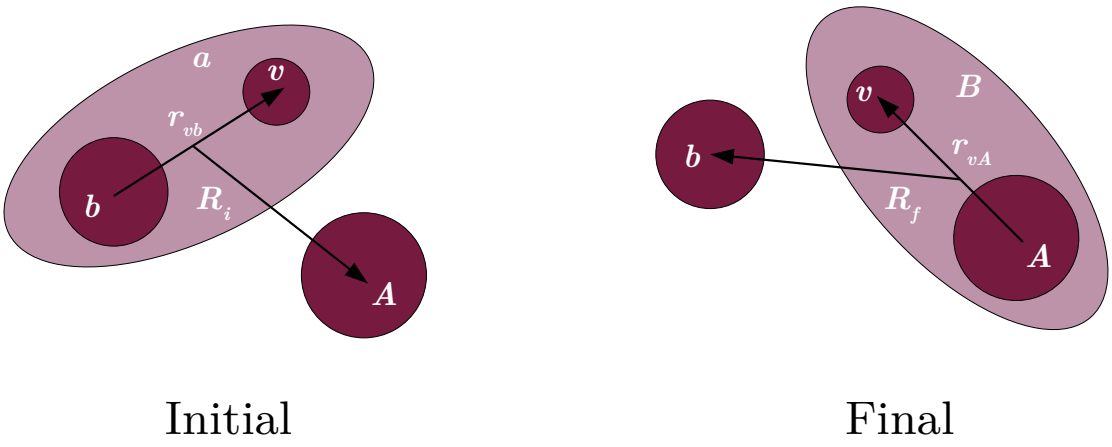


Figure 2.11: Coordinate system for the initial and final states of the $A(a,b)B$ transfer reaction. In this notation, A denotes the target, a the beam, b the ejectile and B the residual nucleus. Figure adapted from reference [34] (figure 14.1).

These equations are very complex, hence the DWBA is employed to simplify the problem. This leads to replacing one of the exact solutions, $\Psi^{(\pm)\text{exact}}$, with a distorted wave multiplied by a corresponding bound state, $\Phi(\mathbf{r})\chi(\mathbf{R})$. This reduces the T matrix for this transfer process to

$$\mathbf{T}^{\text{DWBA}}_{fi} = \langle \chi^{(-)}_f(\mathbf{R}_f)\Phi_{I_A:I_B}(\mathbf{r}_f)|\mathcal{V}|\Phi_{I_b:I_a}(\mathbf{r}_i)\chi_i(\mathbf{R}_i)\rangle\,, \tag{2.11}$$

where $\mathcal{V} = V_{vA} + V_{bA} - U_i$ in the prior form and $\mathcal{V} = V_{vb} + V_{bA} - U_f$ in the post

form is the transfer operator and χ_i and χ_f are the distorted waves corresponding to optical potentials U_i and U_f. Although this form still appears fairly complex, the problem has been reduced to three physical inputs:

1. Optical potentials corresponding to the incoming and outgoing distorted waves.

2. The overlap functions, typically produced by placing single particle states in a Woods-Saxon potential with the depth chosen so as to reproduce the correct binding energy and quantum numbers.

3. The transfer operator. When using the same binding and optical potentials, this only needs consideration of the core-core interaction.

The problem has now been reduced to a point where, using software specifically used to perform DWBA calculations such as FRESCO [34] and DWUCK4 [35], the differential cross sections for a range of nuclear transfer reactions can be calculated. Optical potential parameters can be retrieved from parameter libraries such as RIPL-3 [36] and all other parameters can be calculated based on properties of the particular reaction in question, such as mass of the nuclei involved and the spin/parity of any excited states.

2.3 Nuclear Astrophysics

All across the universe in a variety of cosmic environments countless nuclear reactions are occurring every second. The exact mechanisms for these reactions and the products and energy they produce have profound consequences for how the stars, galaxies and nebulae around us form and evolve. It is therefore no surprise that

astrophysics draws heavily from nuclear physics in some areas, creating the interdisciplinary field of nuclear astrophysics. The main goals of nuclear astrophysics are to explain the energy output of stars and other cosmic environments and to explain the abundance and distribution of isotopes throughout the universe.

When considering what leads to the abundances of different isotopes and elements in the universe, processes that lead to their production need to be considered first. These processes can be specific, relating to the abundance of single isotopes or elements, or can be more general and explain the abundances of a wide range of nuclei. An example of a more specific phenomenon is the Hoyle state [37], which helps explain the rate of carbon production in stellar environments. The production of ^{12}C proceeds through the triple-α process, a process where initially two α particles fuse together to form ^{8}Be. The third α particle then subsequently fuses with the ^{8}Be to form ^{12}C at an excitation energy of around 7.7 MeV. In theory, this process should be rare and does not explain the abundance of carbon observed in the universe. However, the existence of the 7.65 MeV Hoyle state in ^{12}C increases the rate at which this process occurs by a factor of eight orders of magnitude, accurately explaining the stellar abundance of carbon [38].

An area of particular interest is explaining the abundances of nuclei heavier than ^{56}Fe, the isotope with the lowest atomic mass per nucleon. The main processes responsible for this are the rapid and slow neutron capture processes, commonly known as the r-process and the s-process, respectively.

2.3.1 The Rapid Neutron-Capture Process

As their names suggest, the rapid and slow neutron capture processes are sets of nuclear reactions involving the rapid and slow capture of neutrons in order to produce almost all nuclei heavier than ^{56}Fe. Here, 'rapid' suggests that successive captures occur before nuclei have chance to decay, usually via β^- decay due to their neutron-rich nature, whereas 'slow' suggests that radioactive decay to a stable isobar occurs between captures. Therefore, the *s*-process remains closer to the valley of stability (the parabolic shape of the atomic masses along each isobaric (constant A) chain, with the most stable nuclei lying at the bottom) whereas more neutron rich isotopes are produced in the *r*-process. The *r*-process requires a neutron flux ~ 10 orders of magnitude larger than those required for the *s*-process which is why the *s*-process can occur in most stars, particularly stars in the asymptotic giant branch (AGB) region of the Hertzsprung-Russell diagram, whereas the *r*-process can only occur in environments with extreme neutron fluxes such as supernovae and neutron stars [39]. Some nuclei are also produced by the *p*-process, originally the name given to the proton capture process. More recently the *p*-process has sometimes been used to refer to any nucleosynthesis process that produces neutron deficient nuclei, known as *p*-nuclei [40], although it has been suggested that the term *p*-process should only be used to refer to the proton capture process itself [41]. This work will focus on detailing the *r*-process as it is most relevant to the discussion of ^{190}Re, only touching on the *s*-process and *p*-process briefly.

The r-process alone is responsible for producing roughly 50% of all nuclei heavier than iron, with the other 50% produced in the s-process, p-process and another process called the rp-process (rapid proton capture process)[42]. The path the r-process has been calculated to take can clearly be seen in figure 2.12 where is it shown by the magenta line. Stable nuclei produced via the r-process are shown by the magenta blocks. Sharp rises in the proton number of nuclei involved in the r-process can be seen to occur at magic numbers of neutrons (shown by the black bars in figure 2.12). This is because the neutron binding energy drops significantly immediately after closed shells, so the neutrons are more readily knocked out of the nucleus by gamma rays. This results in neutrons being continually added and knocked out until a beta decay occurs, increasing the proton number.

The abundance of nuclei produced by the r-process is shown in figure 2.13. The peaks in the abundances that can be seen are due to an accumulation of material observed at closed neutron shells. This accumulation is due to the aforementioned drop in neutron binding energies beyond neutron closed shells, leading to the formation of astrophysical waiting points in these regions of the chart of nuclides. This, combined with the fact the r-process comes closest to the valley of stability at magic neutron numbers (as seen in figure 2.12) produces the observed abundance peaks as nuclei decay away from the path of the r-process. Specifically, the selenium/strontium peak is due to the $N = 50$ magic number, the xenon/tellurium peak due to the $N = 82$ magic number and the osmium/platinum/gold peak due to the $N = 126$ magic number. Fission recycling, where the r-process duration becomes

sufficiently long and the nuclei sufficiently heavy that fission occurs and the process continues from an earlier stage, also needs to be considered when discussing r-process abundances [43].

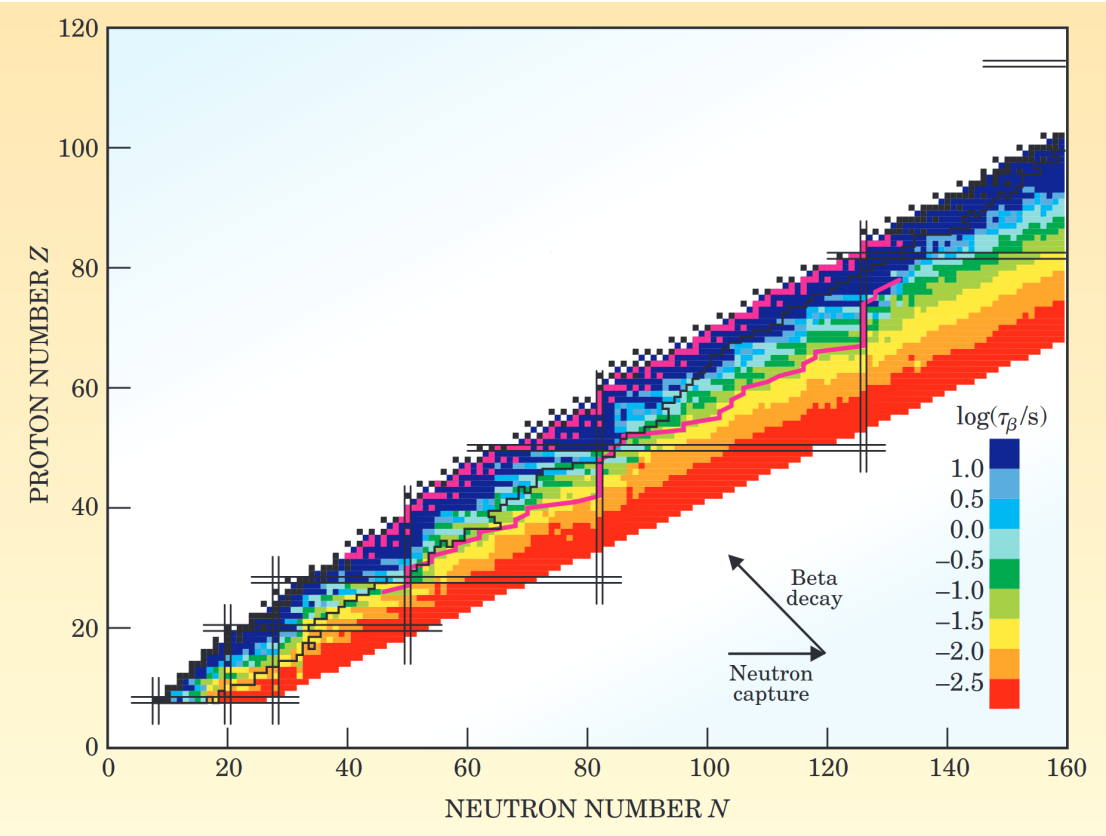


Figure 2.12: Chart showing the stable and neutron-rich nuclides. Stable nuclides are coloured in black and magenta (nuclides coloured magenta are produced as a result of a series of beta decays from a nuclide on the r-process path), with unstable nuclides coloured according to their lifetime. Nuclides further from the line of stable isotopes (known as the valley of stability) have shorter lifetimes. The black bars indicate the locations of closed shells due to magic numbers of nucleons. The magenta line in the centre of the chart shows a typical r-process path predicted by calculations. Figure taken from reference [44] (figure 1).

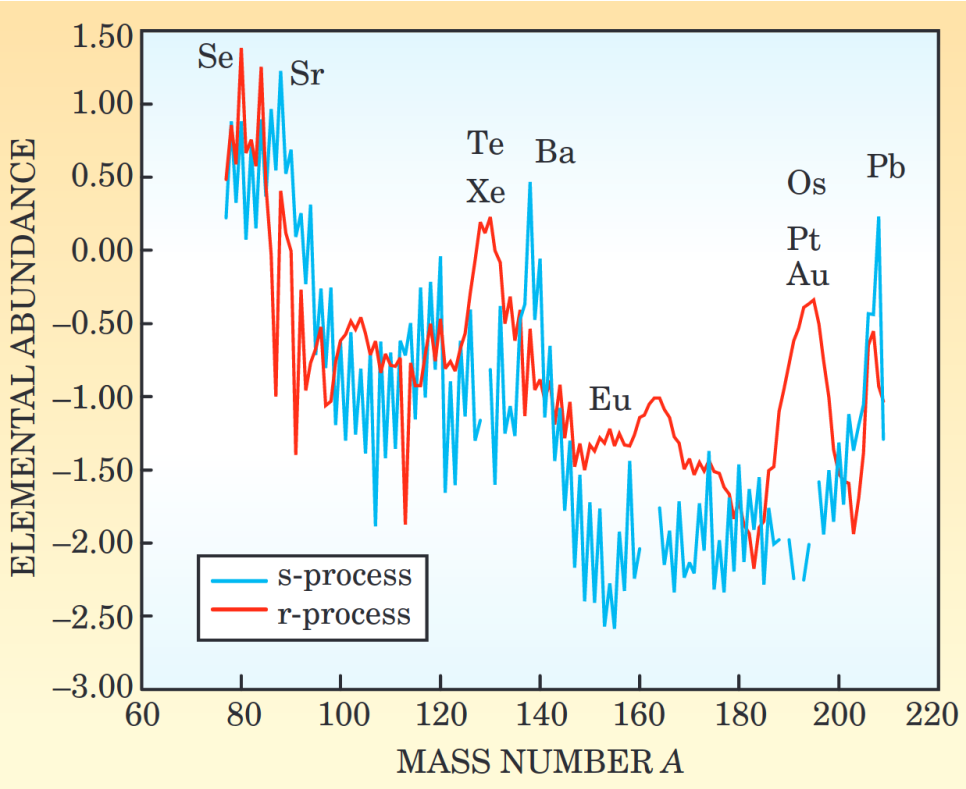


Figure 2.13: Abundances of heavy elements produced via the r-process and s-process in the solar system, as a function of mass number. Elements of particular interest have been labelled. The values on the y-axis are $12 + log_{10}$ of abundance relative to that of hydrogen. Figure taken from reference [44] (figure 2).

Figure 2.13 also shows abundances for the s-process. These are not normalised, but the abundances due to the r-process and s-process are very similar. The abundance peaks due to the s-process lie at a slightly higher mass number as the s-process path is closer to the valley of stability than the r-process path, subsequently encountering neutron closed shells and forming waiting points at a higher mass number.

When studying and modelling processes such as the r-process it is important to have information about a variety of nuclei, such as their atomic mass and energy levels. This allows the production method paths taken by the processes to be more

accurately modelled which, in turn, better explains the experimentally observed abundance peaks [45]. In particular, it is important to determine masses to a precision of 10 keV or lower for understanding astrophysical processes. This is to ensure that the uncertainties in the masses of nuclei do not dominate over reaction rate uncertainties [46, 47].

2.3.2 Isomers in an Astrophysical Context

As has previously been mentioned accurate knowledge of nuclear reaction rates is of great importance to astrophysical nucleosynthesis calculations. Nuclear isomers, mentioned in section 2.1.2, are subsequently of great importance to nuclear astrophysicists. If an isotope exhibits an isomeric state, this may be populated in astrophysical nuclear reactions either preferentially over, or simultaneously with, the ground state. This could subsequently result in either a delayed or an altered decay path. For example, the ground state in ^{108}Ag most commonly undergoes β^- decay into ^{108}Cd with a half-life of 2.4 minutes. However, it has an isomeric state ($^{108\mathrm{m}}$Ag) that most commonly decays via either electron capture or β^+ decay into ^{108}Pd [48]. Although this isotope is not important in an astrophysical context, it is apparent that the presence of such an isomer would have a significant impact on the role a particular isotope might play in an astrophysical process and how it is modelled. Therefore, learning more about the isomeric states in nuclei is currently an important field within nuclear astrophysics, even though most do not have any significant impact. Nuclear isomers that do impact astrophysical processes are known as "astromers" [49].

Chapter 3

Review of Current Literature on Rhenium-190

The focus of this project is measuring improved nuclear data for ^{190}Re ($Z = 75$), such as its atomic mass and level scheme. This isotope is of particular interest as, while not produced directly by the r-process, it lies on the decay path of nuclei populated via this process and therefore improving knowledge of its properties will help to improve astrophysical models. Another property that is also of interest is that ^{190}Re lies in the $A \approx 170$ - 190 region which, as discussed in section 2.1.2, contains large numbers of nuclear isomers which are of interest both from a nuclear structure point of view and also as potential astrophysical waiting points.

In this chapter, both historical studies and current knowledge of ^{190}Re will be detailed in order to give a comprehensive overview of this isotope and to explain more of the motivations behind this project.

3.1 Historical Overview

3.1.1 Level-Structure

Evidence for a rhenium isotope with a mass number of 190 was first presented by Aten Junior and De Feyfer in 1955 [50]. It was produced by irradiating a target of

natural osmium with either a beam of neutrons or deuterons in the $^{190}\mathrm{Os}(n,p)^{190}\mathrm{Re}$ and $^{192}\mathrm{Os}(d,\alpha)^{190}\mathrm{Re}$ reactions. This isotope was found to be a β^- emitter, expected due to its neutron rich nature, and to have a 2.8 ± 0.5 minute half-life. In 1961, the half-life of ^{190}Re was measured to be roughly 3 minutes by Baró and Flegenheimer [51], in agreement with the previous results, but in this study an isomeric state with a half-life of 2.8 hours was also observed. At the time it was thought that there was no transition between the two states, suggesting that the isomeric state decays solely via β^- emission.

In 1969 Haustein and Voigt [52] conducted an extensive study into the properties of the short lived state in ^{190}Re, stated in this work to be the ground state. Improved experimental methods, such as using an osmium source isotopically enriched to $\geq$99 % ^{192}Os, allowed the value of the half-life of the state to be constrained to 3.1 ± 0.3 minutes. The study also looked at assigning spin and parity values for this state using the comparative half-life, or ft-value, for the β^- decay of ^{190}Re. This value allows β decay in different nuclei to be compared and is dependent on the differences between the initial and final nuclear wave functions [5]. Therefore, by looking at the decay of ^{190}Re into states of known spin and parity and calculating the corresponding comparative half-life, spin and parity assignments can subsequently be made for ^{190}Re itself. For example the 1387 MeV state in ^{190}Os, to which the ground state of ^{190}Re most commonly β decays, was known to have a spin-parity configuration of $I^\pi = 3^-$. Calculations involving the ft-value suggested that this transition involves no change in parity and a change in spin of either zero or one.

Therefore, the ground state of ^{190}Re was assigned a spin-parity configuration of either $I^{\pi} = 2^{-}$, 3^{-} or 4^{-}.

This work was improved upon in 1973 through the work of Yates *et al.* [53]. In this experiment a beam of 14 MeV neutrons with a flux of $\sim 10^{9}\,\mathrm{cm}^{-2}\,\mathrm{s}^{-1}$ was incident on a sample of un-enriched osmium tetroxide wrapped in cadmium foil in order to produce ^{190}Re in the $^{190}\mathrm{Os}(n,p)^{190}\mathrm{Re}$ reaction. After studying the ground state and allowing it to decay away, chemical separation was used to separate the remaining rhenium (assumed to be in the isomeric state) from both the radioactive osmium in the sample, which had been produced via the decay of the ^{190}Re ground state, and the unreacted target osmium atoms. Studies of the ground state were found to show "excellent agreement" with the results of Haustein and Voigt [52]. However, the activity of the sample containing the isomeric ^{190}Re was, while sufficient to confirm the presence of the isomeric state, too weak for further study. Therefore, an 18 MeV deuteron beam incident on a source of natural osmium was used to induce the $^{192}\mathrm{Os}(d,\alpha)^{190}\mathrm{Re}$ reaction. From this, the half-life of the isomeric state was found to be 3.3 ± 0.2 h, in fair agreement with previous results. The study also found that the isomeric state does indeed decay into the ground state. However, it first populates an excited state at 119 keV via an isomeric transition before this state subsequently decays into the ground state. This process was found to occur roughly 49% of the time, with the isomeric state undergoing β^{-} decay the other 51% of the time. This work also improved on the spin/parity assignment of the ground state from Haustein and Voigt, arguing that the configuration is specifically

$I^\pi = 2^-$. From this it was deduced that the 119 keV excited state has a spin/parity of $I^\pi = 3^-$ and the transition from this state to the ground state is a rotational M1 transition. As excited states in ^{190}Os populated in the β^- decay of the isomeric state were observed to have a spin ≥ 5, it was deduced that the isomeric state must have a spin of 6, with the spin/parity configuration most likely to be $I^\pi = 6^-$.

Further work by Haustein *et al.* in 1976 [54] led to the discovery of two previously unreported states in ^{190}Re. The study focused on the production of a new neutron-rich isotope, ^{190}W, via the ^{192}Os$(n, 2pn)^{190}$W and ^{192}Os$(p, 3p)^{190}$W knockout reactions. The ^{190}W produced subsequently underwent β^- decay into ^{190}Re. The resulting gamma-ray spectrum measured showed two peaks at 157.6 keV and 162.1 keV which showed similar behaviour to other peaks known to correspond to transitions in ^{190}Re. By comparing their energies with theoretical calculations performed as part of the study, it was proposed that gamma rays of these energies were produced in a two-stage decay from a 319.70 keV state in ^{190}Re, via an 162.1 keV intermediary state. Theoretical predictions and ft-value calculations suggest that these states have spin/parity configurations of $I^\pi = 1^+$ and $I^\pi = 0^+$ respectively. Decays from the $I^\pi = 0^+$ ground state in ^{190}W to both of these states are allowed according to the Fermi and Gamow-Teller selection rules respectively. However, Haustein *et al.* propose that decays to the $I^\pi = 0^+$ state in ^{190}Re are greatly hindered as the Fermi strength is concentrated in an energy-forbidden transition to an isobaric analogue state. As decays to other known states in ^{190}Re would also be forbidden to some degree due to the β^- decay selection rules, it is therefore proposed that the β^- decay

of ^{190}W will feed the 319.70 keV, $I^{\pi} = 1^{+}$ state in ^{190}Re almost all of the time. The decay scheme for ^{190}W, showing this part of the ^{190}Re structure, is shown below in figure 3.1.

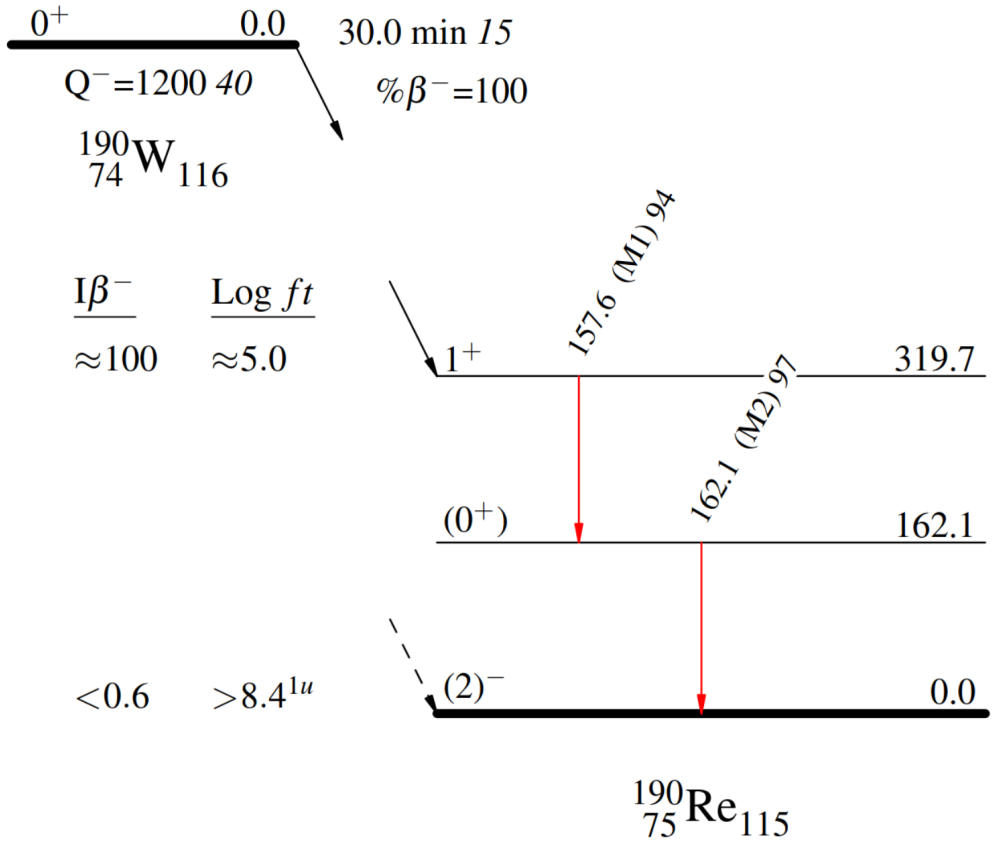


Figure 3.1: Chart showing the β^{-} decay scheme of ^{190}W into ^{190}Re. Energies of states and transitions are given in units of keV. Figure taken from reference [55] (page 31).

This study was also the first to assign Nilsson configurations, discussed in section 2.1.5, to states in ^{190}Re. This is suitable as it is expected that ^{190}Re will exhibit significant deformation as it lies in the $150 \leq A \leq 190$ range of the nuclear chart. For the ground state, the proton and neutron configurations were given as $\frac{5}{2}^{+}[402]_p$ and $\frac{9}{2}^{-}[505]_n$ respectively. The study also gave theoretical predictions for excited states

in ^{190}Re based on the proton and neutron configurations. These are summarised in table 3.1. The observed 119 keV state has the same configuration as the ground state, as it is the first rotational member of the ground-state band.

Table 3.1: Theoretical estimates for spin, parity and energies of excited levels below 1 MeV in ^{190}Re, based on the proton and neutron Nilsson configurations. The energies, given in brackets, are in units of keV. Data taken from reference [54] (table 2).

Neutron	**Proton**	
	$5/2^+[402]$	$9/2^-[514]$
$9/2^-[505]$	2^- (0)	0^+ (216)
	7^- (245)	9^+ (491)
$7/2^-[503]$	6^- (173)	8^+ (498)
	1^- (335)	1^+ (568)
$3/2^-[512]$	1^- (280)	3^+ (553)
	4^- (389)	6^+ (713)
$1/2^-[510]$	3^- (375)	5^+ (663)
	2^- (494)	4^+ (805)
$11/2^+[615]$	8^+ (473)	10^- (672)
	3^+ (610)	1^- (791)

3.1.2 Atomic Mass and Binding Energy

The binding energy of ^{190}Re was first explicitly reported in the 1961 nuclidic mass table [56], which compiled and used all the experimental data available to calculate an extensive list of binding energies for all isotopes known about at the time using theory discussed in section 2.1.3. Here, the binding energy for ^{190}Re is given as 510120 ± 410 keV with the mass excess listed as -35260 ± 410 keV. Such mass tables are published every few years, with the binding energy and mass excess for ^{190}Re being updated each time. A summary of the most accurate calculations of the mass excess and binding energy, as well as atomic mass once this information was added

to the tables, along with publication year for ^{190}Re, is shown below in table 3.2.

Table 3.2: The mass excess, binding energy and atomic mass of ^{190}Re given by all atomic mass evaluations. Here, the unit u refers to an atomic mass unit.

Year	Mass Excess (keV)	Binding Energy (keV)	Atomic Mass (μu)
1961 [56]	-35260 ± 410	1510120 ± 410	(Not Listed)
1964 [57]	-35440 ± 410	1510330 ± 410	(Not Listed)
1971 [58]	-35490 ± 200	1510430 ± 200	189961900 ± 220
1977 [59]	-35520 ± 200	1510410 ± 200	189961870 ± 210
1983 [60]	-35540 ± 200	1510420 ± 200	189961850 ± 210
1993 [61]	-35560 ± 150	1510430 ± 150	189961830 ± 160
2003 [62]	-35570 ± 150	1510443 ± 150	189961820 ± 160
2012 [63]	-35630 ± 70	1510500 ± 70	189961740 ± 80
2016 [64]	-35640 ± 70	1510519 ± 70	189961740 ± 80

In table 3.2 the gradually improved values for the mass and binding energy values can be seen as more extensive studies of ^{190}Re and the processes it takes part in were conducted. All values are in agreement with each other, within errors, suggesting that there are no erroneous measurements.

3.2 Recent Studies and Future Outlook

This section details knowledge of ^{190}Re prior to the work that will be discussed in chapters 5 and 6.

Since the studies detailed in section 3.1, investigations into the properties of ^{190}Re have been infrequent. A study by Luo *et al.* [65] looked into the cross sections of various reactions involving both the ground state and the isomeric state in ^{190}Re. Another study by Walker and Xu [66] looked into the shape of ^{190}Re from a theoretical point of view, which found that in the ground state ^{190}Re is prolate

but an oblate shape can be induced at higher rotational frequencies. Values for the deformation parameters of ^{190}Re have been given by the FRDM(2012) database [45], which uses the finite-range droplet macroscopic model and the folded-Yukawa single-particle microscopic model along with known atomic masses to model nuclear deformations.

In terms of the energy-level structure, no states have been reported other than those discussed in section 3.1.1. An experiment performed by Reed *et al.* [67] in 2012 using the Experimental Storage Ring (ESR) facility at GSI studied neutron-rich, long-lived isomers in the Z = 72-76 region, including the isomeric state in ^{190}Re. The ESR [68] is a heavy-ion storage ring, capable of storing and measuring ions produced in reactions induced by ions of stable beams, accelerated by the heavy-ion synchrotron (SIS). The study measured the energy of the isomeric state, finding it to be 204 ± 10 keV by measuring the mass difference between it and the ground state of ^{190}Re. This was in agreement with the most accurate measurement published at the time (210 ± 50 keV [62]) and also with results from a previous experiment performed at the ESR (227 ± 40 keV). A further study at the ESR, looking to perform Schottky mass measurements of neutron-rich isotopes in the $70 \leq Z \leq 79$ region produced ^{190}Re but did not make any direct observations improving on previous measurements.

Knowledge of the energy-level structure in ^{190}Re prior to this study is shown in figure 3.2. Previously only four excited states had been observed, fewer than might be expected for ^{190}Re as it has been investigated over many years. Therefore, it

would be expected that future studies would potentially elucidate information on further excited states in the energy level structure of ^{190}Re, with the potential for further isomeric states to be discovered. Also, several of the spin/parity assignments are only tentative, as denoted by the brackets surrounding the assignments such as the $I^{\pi} = (6^{-})$ assignment for the isomeric state. Further studies could potentially provide more definitive assignments for these known states, as well as providing values for the spin and parity of any previously unobserved states.

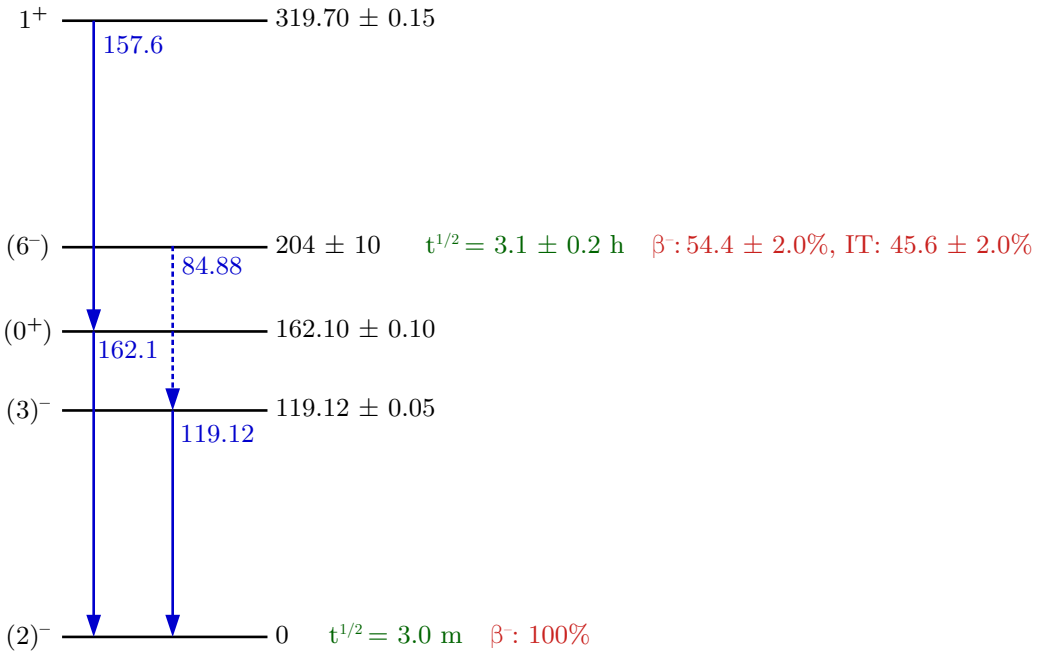


Figure 3.2: Diagram showing the energy-level structure of ^{190}Re, including half-lives and decay schemes where known. Energies of states and transitions are given in units of keV. Data taken from reference [55] (page 29).

The values for the atomic mass and mass excess of ^{190}Re given in the 2016 Atomic Mass Evaluation, given in table 3.2, are both uncertain by around 70 keV. This is significantly greater than the 10 keV limit important for understanding astrophysical processes, such as the r-process, described in section 2.3.1. Through improvement

of current literature values of the atomic mass/mass excess for ^{190}Re and finding out more information about the isomeric states it forms, the improvements can feed into both nuclear structure models and also astrophysical process models such as the Brussels Nuclear Library (BRUSLIB) [69]. Improving the accuracy of values found in nuclear databases, such as NUBASE, is important as it aids other nuclear physics studies. Many values are interrelated, so improving one value may lead to a reduction in the uncertainty of several others. For example, a reduction in the uncertainty of the mass of a particular isotope may lead to a reduction in the Q-value uncertainty of several reactions involving that isotope. Subsequently, studies involving these reactions can be performed more accurately. Therefore, it can be seen that further studies of ^{190}Re and its properties would be of significant interest to a variety of different fields within nuclear physics.

Chapter 4

Experimental Details

The aim of this experiment is to elucidate more information about the properties of ^{190}Re, including its atomic mass and energy-level structure. To achieve this, a set-up where ^{190}Re is produced in a range of excited states is required. The chosen set-up also needs to be able to measure products of the reaction that produces ^{190}Re in a manner that allows for measured properties of these products to be used to deduce information about ^{190}Re. For this reason, the $^{192}\mathrm{Os}(\vec{d},\alpha)^{190}\mathrm{Re}$ reaction was chosen, where $\vec{d}$ denotes that a polarised beam of deuterons was used. This chapter will explain the reasoning behind this specific choice of reaction and what information can be measured and extracted as a result. The experimental set-up used to perform this reaction and measure the subsequent observables will also be detailed.

4.1 Experimental Requirements and Observables

In order to accurately measure properties of ^{190}Re via the $^{192}\mathrm{Os}(\vec{d},\alpha)^{190}\mathrm{Re}$ reaction the experimental set-up used needs to satisfy certain criteria. Firstly, the set-up needs to allow for the α-particle ejectiles to be detected and their energy measured. The energy of the ejectiles will vary depending on the excitation energy of the corresponding residual ^{190}Re nucleus, so by measuring this energy for a large number of α-particles and producing an α-particle energy spectrum, an inverted ^{190}Re energy spectrum would be expected. This spectrum will be inverted as a higher-energy α-particle corresponds to a residual ^{190}Re nucleus produced in a lower-energy state.

Most experimental set-ups will initially give energies in terms of 'channel number', not energy, where each channel corresponds to a discrete range in some input (typically voltage or position) to the data acquisition system. This is because the relationship between channel number and energy varies significantly dependent on the exact configuration of the experimental set-up (such as magnetic field settings) and the ambient conditions. Therefore, it is common to perform an energy calibration by producing a nucleus with many well established excited states in a similar reaction and using the data measured from this reaction to deduce the relationship between channel number and energy for the particular set-up. A suitable reaction to calibrate a detector for the ^{192}Os$(d,\alpha)^{190}$Re reaction (Q-value = 10412 $\pm$ 5 keV) is the ^{194}Pt(d,α)^{192}Ir reaction (Q-value = 10786.3 $\pm$ 1.4 keV). This reaction was chosen as it uses the same projectile and ejectile as the reaction used to produce ^{190}Re and also has similar kinematics (due to the comparable Q-values and masses of the reactants involved in both reactions) meaning that the experimental set-up does not need to be altered when switching between targets. There are also precise literature values for the energy levels of ^{192}Ir [70] that can be used in the calibration. One disadvantage of using ^{192}Ir to calibrate is that it has a high density of states at low excitation energies which can potentially result in some difficulties when fitting energy-levels in regions where the peaks overlap. The high density of states in ^{192}Ir stems from the fact it is a deformed nucleus with an odd number of both neutrons and protons. Therefore, it can couple two valence particles in many ways at low excitation energies.

Due to the nature of the calibration procedure, it is also possible to calculate the atomic mass of ^{190}Re from the Q-value of the ^{192}Os$(d,\alpha)^{190}$Re reaction which is measured relative to the Q-value of the ^{194}Pt$(d,\alpha)^{192}$Ir reaction. There are precise literature values (precise in this context meaning with an uncertainty below 10 keV, important for astrophysical calculations as explained in section 2.3) for the atomic masses of ^{192}Os and ^{194}Pt as well as ^{192}Ir [64]. Therefore, comparison between the Q-value of the ^{192}Os$(d,\alpha)^{190}$Re and ^{194}Pt$(d,\alpha)^{192}$Ir reactions and knowledge of equation 2.4 in section 2.1.3 can be used to deduce the atomic mass of ^{190}Re to a similar level of uncertainty. This is another reason why also performing the ^{194}Pt$(d,\alpha)^{192}$Ir reaction is important in order to meet the aims of this experiment.

To deduce the spin and parity of the measured states in ^{190}Re, it is also important to have an experimental set-up that can produce a polarised beam of deuterons and measure the α-particle ejectiles at a range of angles with respect to the beam axis. This is so that the differential cross section and the analysing power, described in sections 2.2.1 and 2.2.2, can be calculated from the measured data. These measurements can be subsequently compared to distorted-wave Born-approximation calculations for a variety of spin and parity configurations in order to assign the best matching configuration to each state.

4.2 Instrumentation and Set-up

An experiment was performed at the Maier-Leibnitz Laboratory (MLL) in Munich using the 14 MV tandem Van de Graaff accelerator and the Q3D magnetic spectrograph [71, 72] at the facility. The accelerator produced both polarised and unpolarised deuteron beams at an energy of 18 MeV. These were focused on targets of ^{192}Os and ^{194}Pt of thicknesses $45\,\mu g\,cm^{-2}$ and $66\,\mu g\,cm^{-2}$ respectively. Both targets were backed with $7\,\mu g\,cm^{-2}$ of carbon. This set-up was used to induce the ^{192}Os(d,α)^{190}Re and ^{194}Pt(d,α)^{192}Ir reactions. The former reaction was used to produce the ^{190}Re that was the primary focus of this experiment, while the latter reaction was used in order to calibrate the focal-plane detector of the Q3D magnetic spectrograph.

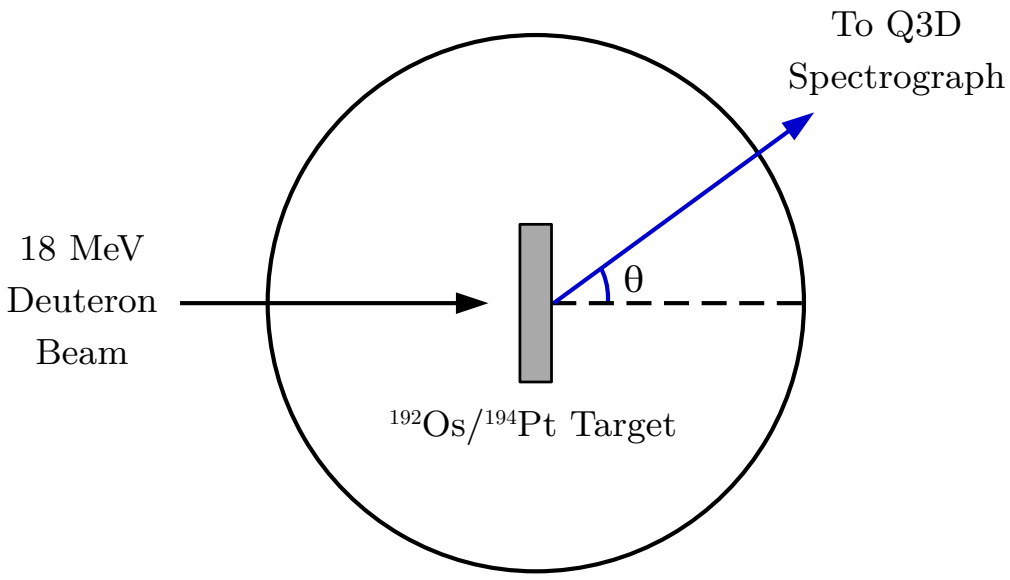


Figure 4.1: Schematic diagram showing a basic overview of the experimental set-up. The value of θ was was set to several angles between 10° and 45° in order to measure data on the differential cross section of the chosen reactions.

The Q3D spectrograph was positioned at various angles within the angular range 10°- 45° with respect to the beam axis. This was done so that sufficient data were obtained in order to allow the measurement of differential cross sections, as detailed in section 2.2.1. For the calibration reaction, the detector was only placed at 20° - 21° as the differential cross sections are known for ^{192}Ir and are not a focus of this work. A schematic view of the set-up is shown in figure 4.1.

4.2.1 Ion Production and Acceleration

As has been previously discussed, the 14 MV tandem Van de Graaff accelerator at MLL is capable of producing polarised and unpolarised beams of both protons and deuterons. These ions are initially produced by a Stern-Gerlach ion source. Gaseous hydrogen or deuterium is injected in the atomic beam source (ABS) which splits the molecular gas into individual atoms through interactions with electrons in a cold plasma. At this stage, adiabatic expansion of the atomic gas in a vacuum chamber produces an atomic jet which is directed towards four sextupole Stern-Gerlach magnets positioned one after another, which are used to separate the atoms based on their spin. The electron polarisation is then transferred to nuclear polarisation using adiabatic radiofrequency transitions. The jet is directed to an electron cyclotron resonance (ECR) chamber to be ionised. The ionisation is a two-stage procedure; first the atoms are positively ionised within the ECR chamber before this positive beam is directed towards a caesium target by two deceleration electrodes. Here, the ions pick up two electrons resulting in them becoming negatively ionised with an efficiency $\geq 30\%$. These negatively charged ions are then directed towards the tandem Van de Graaff accelerator [73].

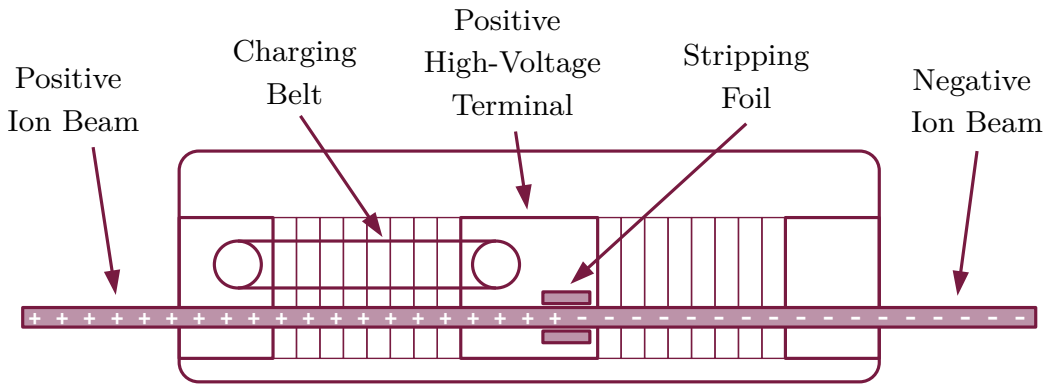


Figure 4.2: Schematic view of a generic tandem Van de Graaff accelerator, where the acceleration is from right to left. Figure adapted from reference [74] (figure 1).

Tandem Van de Graaff accelerators, a generic example of which is shown in figure 4.2, are so-called as they use the general principle of a Van de Graaff generator to accelerate ions in a two stage process. Negative ions are fed into the device and are accelerated towards a positive, high-voltage terminal in the centre. The large potential at this point is generated by a charging belt which carries negative charge away from the centre of the device to ground. At the terminal the negative ions are stripped of electrons resulting in them becoming positively charged. At the MLL tandem Van de Graaff accelerator this stripping process is performed by a carbon foil. The ions, now positive, are then subsequently accelerated away from the positive high-voltage terminal. As this configuration accelerates ions twice using a single machine it has the advantage of being able to reach higher beam energies for a given operating voltage and, as the high-voltage terminal is in the middle of the machine, both ends of the device are at ground which results in easier maintenance of other devices situated near the ends of the machine, such as the ion source [75].

The positive ions from the tandem Van de Graaff accelerator are then sent through to the Q3D magnetic spectrograph via a 90° analysing magnet. This final magnetic element results in a very high beam-energy accuracy.

4.2.2 Q3D Magnetic Spectrograph

The Q3D magnetic spectrograph, named after its single **Q**uadrupole and three **D**ipole magnets, is used to perform high-resolution energy measurements of particles produced in reactions at MLL. Magnetic spectrogaphs operate by separating reaction products based on differences in their trajectories due to differences in their momenta and, therefore, energy. Specifically, in the Q3D spectrograph the quadrupole magnet initially focuses the reaction products entering the device, maximising the solid angle acceptance, before the three dipole magnets are used to separate reaction products based on their momentum to charge ratio. A higher order multipole element, placed between the first and second dipole magnets, produces a magnetic field perpendicular to the motion of the particles, correcting for kinematic broadening and other effects [71, 72].

Due to the separation based on the charge-to-momentum ratio, for particles of the same charge their position on the focal-plane detector is a function of their kinetic energy. This energy can then be used to infer the excitation energy of the residual nucleus produced in the same reaction as the ejectile particle. The length of the focal-plane detector (0.89 m, with the focal plane itself having a length of 1.8 m) limits the range of excitation energies measurable for certain magnetic

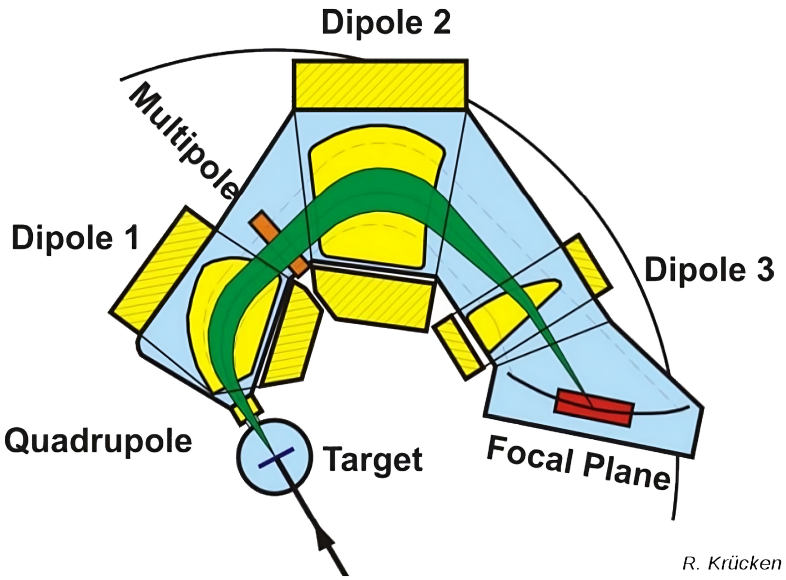


Figure 4.3: Schematic view of the Q3D magnetic spectrograph with the magnetic components labelled. The path charged particles take through the detector is highlighted in green. Figure taken from reference [76] (figure 1).

settings, so these settings need to be carefully chosen for a given experiment. For this experiment, the Q3D fields were set corresponding to focus on an energy of $E_x^{\mathrm{Q3D}} = 400\,\mathrm{keV}$ in ^{190}Re, yielding an acceptance range of roughly -200 - $2200\,\mathrm{keV}$. The Q3D is highly dispersive, resulting in this small energy-range acceptance. Although it seems illogical to have a negative acceptance range as this is unphysical, this was done to ensure that low-lying states in ^{192}Ir, produced with a more positive Q-value, could be observed using the same magnetic field settings as any change in field between the ^{192}Ir and ^{190}Re reactions would have required a new calibration. The energy that the detector has been set to focus on is not in the centre of the acceptance range due to the non-linear relationship between the energy and channel number. This relationship is non-linear due to the curved nature of the focal plane. The spectrometer sits on a curved track which it can be moved along in order to

measure the angular distribution of ejectiles. In this experiment, an angular range of 10° to 45° was used. The in-plane angular acceptance of the Q3D is ±3°. In figure 4.3 a schematic overview of the Q3D spectrograph is shown.

4.2.3 Focal-Plane Detector

The focal-plane detector, shown in figure 4.4, is filled with isobutane gas at a pressure of 500 mbar. It consists of two sets of cathode foils surrounding anode wires which act as proportional counters [77]. The foil furthest from the 25 μm Kapton® entrance window of the focal-plane detector is a cathode strip foil, segmented into 255 individual strips with a repetition length of 3.5 mm. As the positive-ion ejectiles travel through the two proportional counters they ionise the gas, liberating electrons which are subsequently accelerated towards the anode wire. This process produces a charge avalanche as the accelerating electrons induce further ionisation.

The positive ions produced in the avalanche travel towards the cathode foils. The ions interact with several strips on the cathode strip foil, as can be seen in figure 4.4. The charge induced on each of the strips can be fitted with a Gaussian distribution, with the condition a signal has to be produced on 3-7 consecutive strips to be considered valid (the voltage across the detector is tweaked for a particular reaction to give an average of 5 channels). The centroid value of this fit gives the horizontal position of the incident particle. The energy loss of the particles as they travel through the detector can also be measured by both sets (planes) of anode wires, while the plastic scintillator is able to measure the residual energy of the particle after

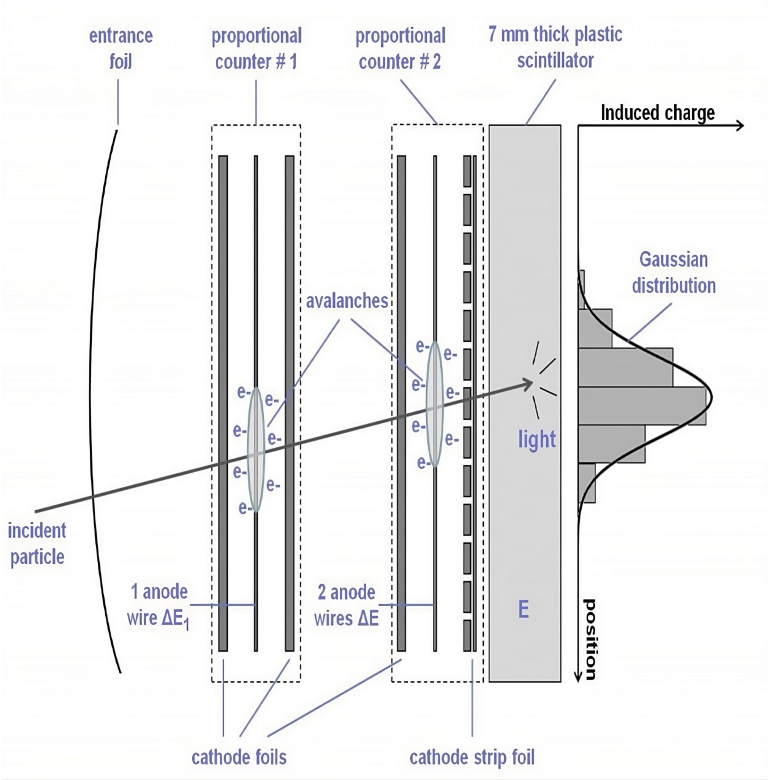


Figure 4.4: Diagram showing how the different components of the Q3D's focal-plane detector are used to detect incoming particles. This diagram shows the detector from above, resulting in the two anode wires in the second proportional counter appearing as a single wire. Figure taken from [78] (figure 2).

it has passed through the proportional counter stages of the detector. Knowledge of these properties allows for particle identification to be performed [79], as will be detailed in section 4.4.1.

4.3 Run Information

Using the aforementioned experimental set-up, twenty-nine experimental runs were performed. The data were collected using the MARABOU software (MBS And ROOT Based Online/Offline Utility) at Munich [80]. Four of these runs produced ^{192}Ir with the remaining twenty-five producing ^{190}Re. Experimental details for each

of these runs are shown in table 4.1. Here, details for each of the runs relevant for further analysis is given, such as the recoil isotope produced, the angle of the Q3D magnetic spectrograph with respect to the beam axis and the polarity of the beam (given as 'N/A' if the beam was unpolarised). The table also gives the values of 'SCA1' and 'SCA3' for each run, shorthand for scaler 1 and scaler 3 respectively (the information contained by these values is detailed in section 6.2.1), and the beam current. All these values relate to the current measured by the Faraday cup integrator and can be used to calculate the number of beam particles and detector dead-time per run.

The number of hits on the 4096 channels of the Q3D's focal-plane detector was recorded for each run. For similar runs, these values can be summed together to increase the statistics. For example, runs $4, 5, 6, 7, 26$ and 27 could be combined to give the spectrum of α-particle ejectile energies for the ^{194}Pt(d,α)^{192}Ir reaction, corresponding to a reversed ^{192}Ir energy spectrum. Runs can be grouped together based on the induced reaction, Q3D angle and polarity of the beam where required.

Table 4.1: A table showing details for each of the twenty-nine experimental runs performed as part of this study. For each run details of the specific experimental set-up and properties of the beam are given. Red and blue rows have been used to easily distinguish runs corresponding to the production of ^{190}Re and ^{192}Ir respectively, with lighter to darker shades of each colour corresponding to no beam polarisation, a spin-down beam and a spin-up beam.

Run Number	Product	Q3D Angle (°)	Beam Polarity	SCA1	SCA3	Beam Current (μA)
3	^{190}Re	20	N/A	2982270	13213	0.06
4	^{192}Ir	20	N/A	1593292	7616	0.03
5	^{192}Ir	20	N/A	950872	27126	0.2
6	^{192}Ir	20	N/A	958457	2116	1.05
7	^{192}Ir	20	N/A	5814595	25186	0.9
8	^{190}Re	20	N/A	1986476	10716	0.75
9	^{190}Re	20	N/A	8100187	51365	1.35
10	^{190}Re	25	N/A	9756745	22710	1.25
11	^{190}Re	45	N/A	17977479	30932	1.2
12	^{190}Re	10	Up	2951550	16718	0.75
13	^{190}Re	10	Down	2888517	15835	0.8
14	^{190}Re	10	Up	3714520	20151	0.7
15	^{190}Re	10	Down	3099909	17821	0.71
16	^{190}Re	15	Down	764315	1356	0.8
17	^{190}Re	15	Up	3084708	6233	0.8
18	^{190}Re	15	Down	3042704	6144	0.8
19	^{190}Re	15	Up	2981309	6063	0.8
20	^{190}Re	15	Down	3027305	6020	0.79
21	^{190}Re	21	Down	1225739	9028	0.8
22	^{190}Re	21	Up	2662419	9626	0.4
23	^{190}Re	21	Down	2403719	9220	0.63
24	^{190}Re	21	Up	2487844	9784	0.6
25	^{190}Re	21	Down	816217	3688	0.6
26	^{192}Ir	21	Down	1474959	4816	0.6
27	^{192}Ir	21	Up	930382	3350	0.6
28	^{190}Re	27	Down	2302297	3038	0.6
29	^{190}Re	27	Up	2216554	2787	0.6
30	^{190}Re	27	Down	2278075	3028	0.57
31	^{190}Re	27	Up	2240351	2938	0.6

4.4 Data Analysis

For each run, a data file was produced containing the information recorded by the focal plane of the Q3D magnetic spectrograph. Before further analysis, these files were processed by a user written sort file written in Fortran77 and run using the Sunsort software package [81]. The sort file processed the raw input on an event-by-event basis, accounted for some settings of the Q3D and wrote the data in forms suitable for further analysis.

4.4.1 Event Selection

Once the raw files from the focal plane of the Q3D had been sorted, the desired events needed to be selected. Although the experimental set-up had been optimised for the ^{192}Os(d,α)^{190}Re and ^{194}Pt(d,α)^{192}Ir reactions, the conditions were such that other reactions could occur from which some events could reach the focal-plane detector, notably (d,p) and (d,d) reactions. Therefore, using properties of the measured ejectiles and the manner in which they interact with the focal-plane detector, events corresponding to the production of an α-particle ejectile need to be identified and selected for further analysis; removing events in which other types of ejectile have been produced. This was done by plotting events in two-dimensional histograms and only accepting those which fall into a certain region or 'window' of the plot. Examples of these plots are shown in figure 4.5.

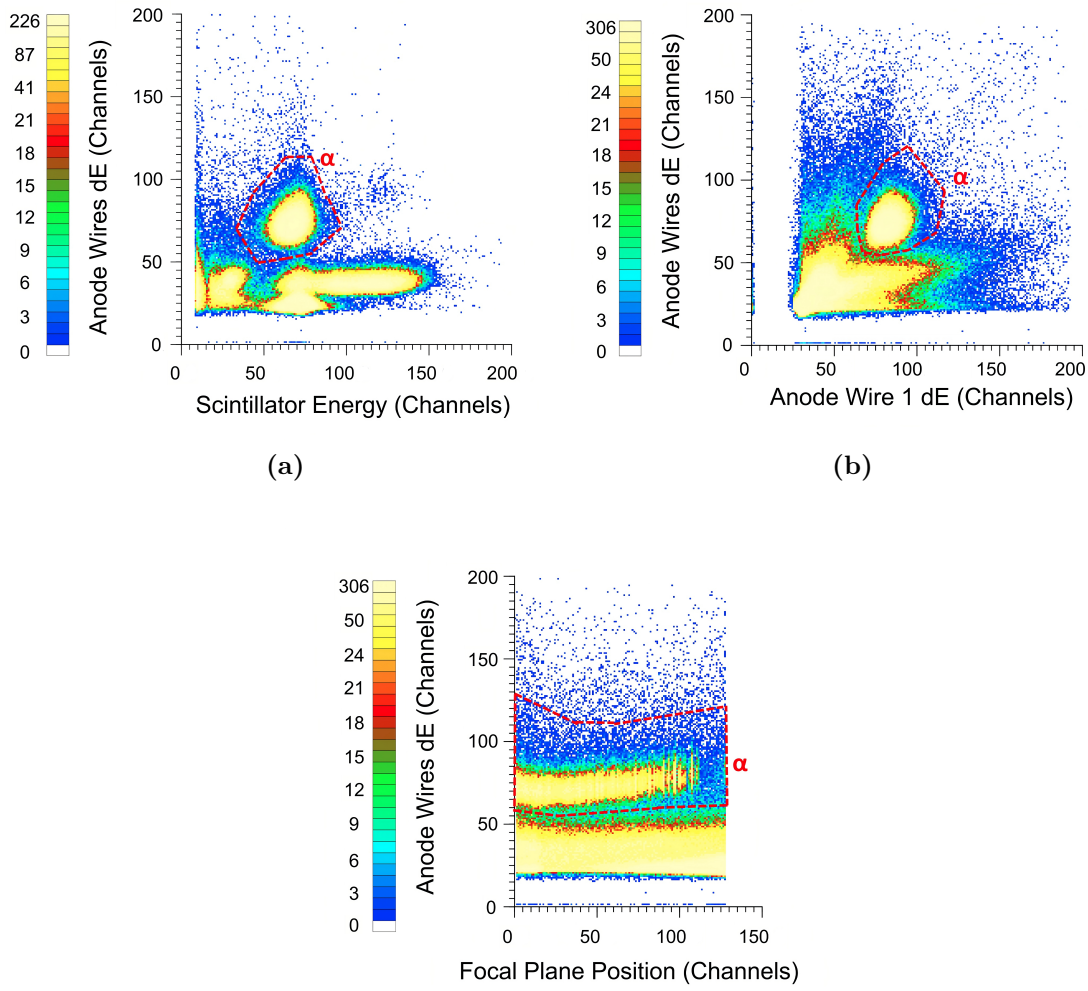


Figure 4.5: Plots showing how charged particles, in this case α-particles, were identified using properties measured by the Q3D magnetic spectrograph. A heat-map colour scheme is used to show intensities, with a colour scale shown beside each plot. Regions (known as "windows") corresponding to α-particles are denoted by red dashed lines. All three plots show the energy loss as measured by the anode wires on the y-axis. On the x-axis is the residual energy measured by the scintillator (a), the energy loss measured by the first anode wire (b) and the position on the focal plane (c). Note that position on the focal plane is proportional to the energy of the detected particle.

For this study three windows, or two-dimensional gates, were used for event selection.

All of the 2-D histograms show the energy loss as measured by the two anode wires

in the second proportional counter, shown in figure 4.4, on the y-axis. The x-axis for the three window plots are the residual energy of the particle as measured by the scintillator, the energy loss as measured by the single anode wire in the first proportional counter and the position of the particle on the focal plane of the detector (which is proportional to the energy of the ejectile). It can be seen in figure 4.5 that plotting events based on these properties results in multiple clear regions of high intensity in each of the plots, corresponding to the observation of different types of ejectile.

These windows can be chosen either by matching the regions to simulated Monte-Carlo events or by manually identifying regions based on energy loss characteristics of different particles. As previously mentioned, it was known that almost all particles will correspond to protons, scattered deuterons or α-particles. As α-particles exhibit the highest energy loss per distance travelled of these three particles [82], regions corresponding to the highest energy loss were selected in each case. By requiring that events have to lie within the windows shown on all three panels of figure 4.5, the vast majority of selected events will correspond to the detection of α-particles.

The effect of the windows can be seen in figure 4.6, where spectra corresponding to the production of ^{190}Re are shown with no windows, one window, two windows and all three windows applied. All ^{190}Re runs shown in table 4.1 were used to generate this data set. It is clear to see that there is a large reduction in the number of counts going from no gates being applied to implementing a single window. Individual peaks

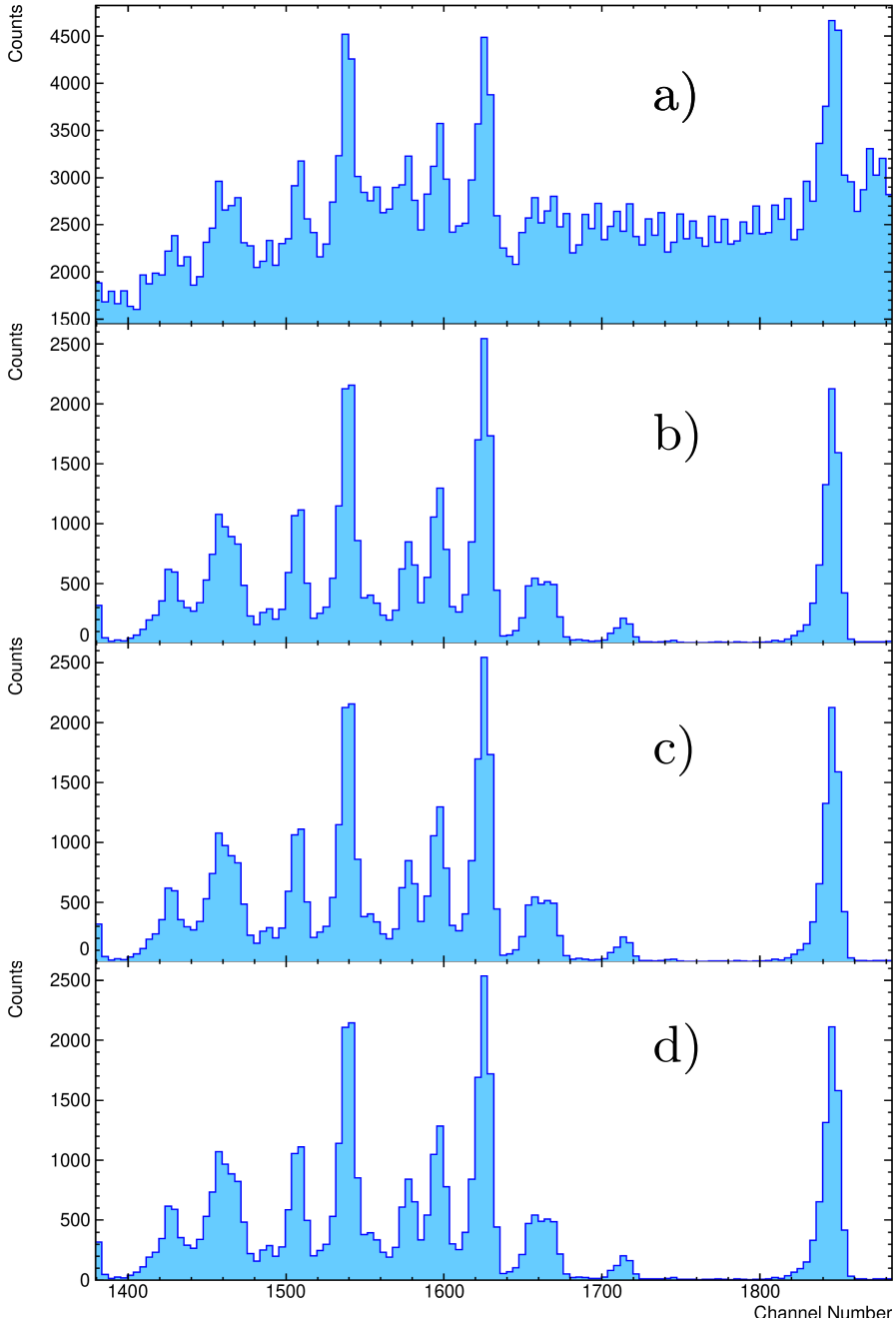


Figure 4.6: Spectra corresponding to the measurement of the energies of α-particle ejectiles from the ^{192}Os(d,α)^{190}Re with different gating applied. No gating was used in spectrum a). In spectrum b), the window corresponding to the residual energy measured by the scintillator of the Q3D was used. For spectrum c), the window corresponding to the energy loss as measured by the first anode wire was added. Spectrum d) was produced using all three windows described in the text.

corresponding to excited states in ^{190}Re can also been seen much more clearly. Going from a single gate to two or three gates, a much more subtle change is seen. There is some reduction in the number of counts, too small to see clearly in 4.6, but is of the order of tens of counts for most channels. This is expected, as in theory each of the gates should be cutting the same set of events. Using multiple windows is a good test of this logic.

4.4.2 Energy Calibration

Before further analysis could be performed, the focal plane of the Q3D magnetic spectrograph needed to be calibrated. This involved finding a relationship between the channel number given by the Q3D and the corresponding energy of the α-particle ejectiles. As discussed in section 4.1, the ^{194}Pt(d,α)^{192}Ir reaction was used to perform this energy calibration, owing to the large number of known states in the level structure of ^{192}Ir. To achieve this, an energy spectrum for ^{192}Ir needs to be produced. In order to produce such a spectrum, data from runs $4, 5, 6, 7, 26$ and 27 in table 4.1 were combined. As only the energy of the peaks are needed for a calibration, the data do not need to be split according to beam polarity.

Suitable data were selected via gating as described in section 4.4.1 in order to produce a spectrum with peaks corresponding to resonances in the energy-level structure of ^{192}Ir. The resonances themselves have a Breit-Wigner form. However, as they are all bound and therefore long-lived ($\sim$ fs or longer), the levels are narrow in energy (much less than an eV) and subsequently the Gaussian resolution of

the detector dominates. Observed peaks were then fitted as a series of Gaussian distributions with a linear background. This was done for a variety of energy levels across the region of interest to ensure the calibration was accurate for the relevant region of the focal plane.

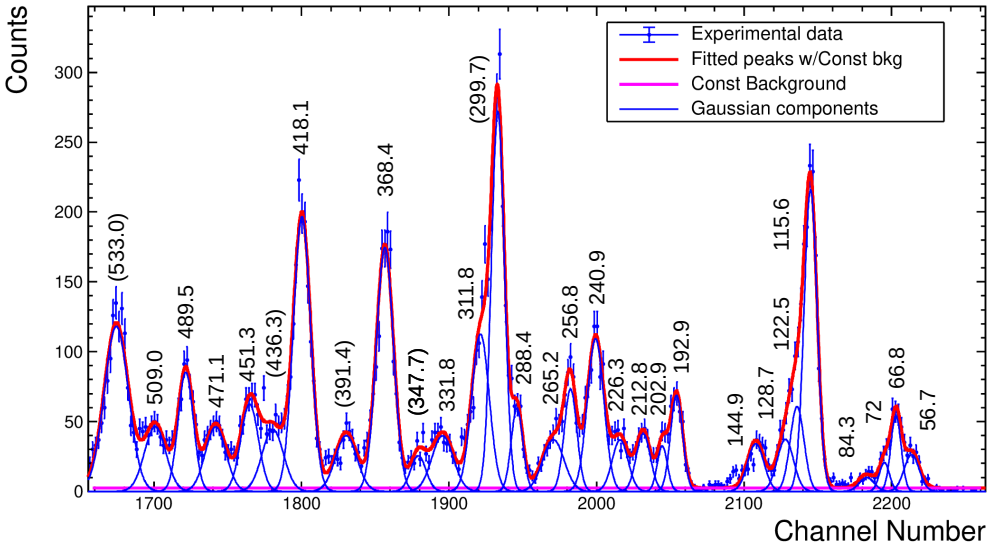


Figure 4.7: Plot showing the fitted low-energy region of the ^{192}Ir spectrum. As the detector was used to measure the energy of α-particle ejectiles produced in the ^{194}Pt(d,α)^{192}Ir reaction, a high channel number (and therefore high α-particle energy) corresponds to a low excitation energy for the residual ^{192}Ir nucleus. Each peak is labelled with its corresponding assigned energy in units of keV [70]. The typical uncertainty in the centroid energy of the peaks from the fit is roughly 1 keV. Peaks omitted from the calibration due to comprising several close-lying energy levels are labelled in brackets with energies obtained after calibrating.

The fitted ^{192}Ir spectrum is shown in figure 4.7. Here, each of the observed peaks is labelled with a corresponding assigned literature energy in units of keV. Not all known energy levels in ^{192}Ir were populated in this experiment, and some peaks could

not confidently be assigned a known energy value due to high level degeneracy in certain regions of the spectrum. The low lying $I^{\pi} = 1^{-}$, 56.72 keV energy level in ^{192}Ir is the ^{192m1}Ir isomeric state ($t_{1/2} = 1.45 \pm 0.05$ mins) [64]. Note that the ground state of ^{192}Ir was not observed in this experiment. Using the assigned energy values a quadratic fit, appropriate for the focal plane of the Q3D magnetic spectrograph, was performed to give a relation between channel number and excitation energy for the residual nucleus. This calibration is shown in figure 4.8

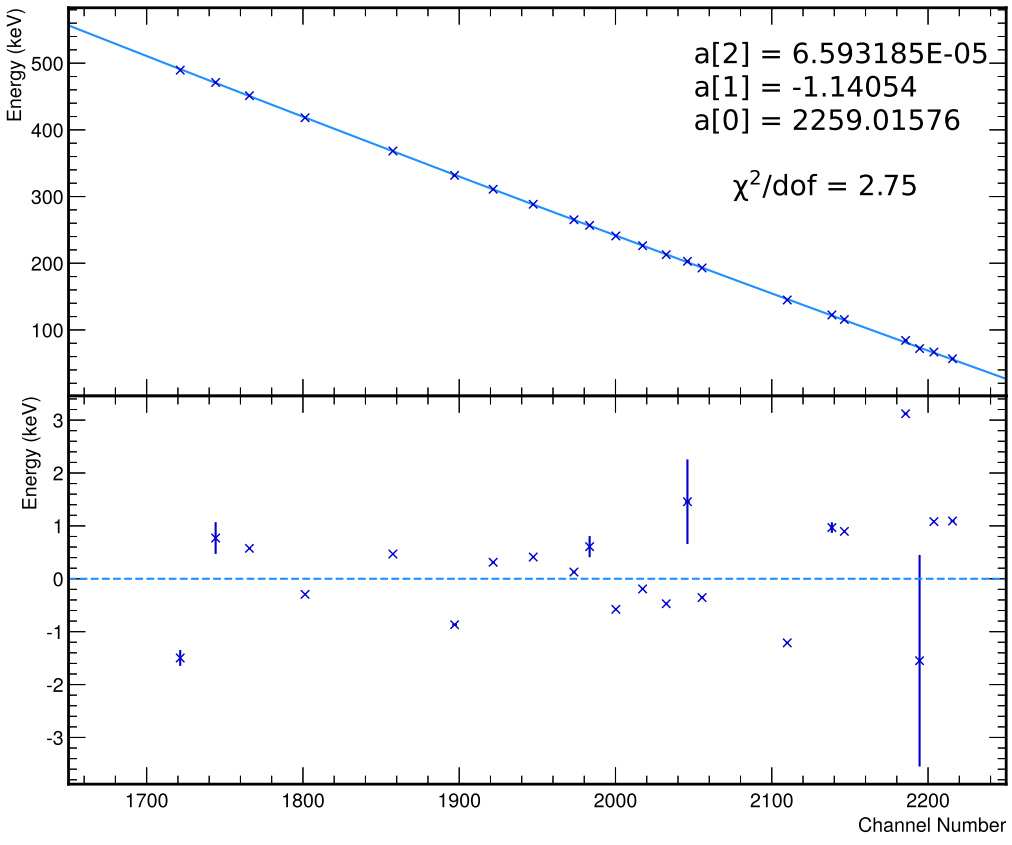


Figure 4.8: Plot showing the energy calibration for the focal-plane detector of the Q3D magnetic spectrograph, with measured data points shown and the calibration parameters given. The second plot gives the residuals of the calibration.

This calibration could then be used to calculate the energy of any unknown peaks in ^{190}Re, once a correction has been made to the intercept. This was required as the spectrum in figure 4.7 gives the energy of the α-particle ejectile. This is dependent on the Q-value of the reaction in which the α particle was created and the recoil energy of the heavy product which will be different for the ^{192}Os(d,α)^{190}Re and ^{194}Pt(d,α)^{192}Ir reactions and this difference needs to be accounted for. The calibration can also be used to relate the channel number to the energy of the α-particle ejectiles directly using kinematic calculations.

4.4.3 Energy Spectra of Rhenium-190

In a process similar to that detailed for ^{192}Ir, α-particle ejectile spectra corresponding to the production of ^{190}Re in the ^{192}Os(d,α)^{190}Re reaction needed to be produced in order to deduce information about the atomic mass and structure of the isotope. As a polarised beam is not required for the atomic mass/binding energy calculation, a spectrum was produced combining data from runs 3, 8 and 9 for the purposes of this investigation. The Q3D was placed only at 20° for these runs as it is important to keep the emission angle consistent for kinematic calculations. For investigations into the details of the energy-level structure in ^{190}Re knowledge of the ejectile emission angle and beam polarity is important, so runs were combined accordingly. A summary of which runs were combined for this part of the analysis is given in table 4.2

Table 4.2: Details of the experimental runs combined in order to study the energy-level structure of ^{190}Re.

Q3D Angle (°)	Beam Polarity	Runs	Total SCA1	Total SCA3
10	Up	12, 14	6666070	36869
10	Down	13, 15	5988426	33656
15	Up	17, 19	6066017	12296
15	Down	16, 18, 20	6834324	13520
21	Up	22, 24	5150263	19410
21	Down	21, 23, 25	4445675	21936
27	Up	29, 31	4456905	5725
27	Down	28, 30	4580372	6066

An example of a raw ^{190}Re spectrum, using data from the ^{190}Re runs with an unpolarised beam, is shown in figure 4.9. As expected, several distinct peaks corresponding to excited states in the energy-level structure of ^{190}Re can be seen. Similar spectra were produced for the different emission angles and beam polarities. Peaks were observed at similar channel numbers but the relative intensity of these peaks varied as the angle of the Q3D magnetic spectrograph and the beam polarity were altered. This can be seen in figure 4.10 and figure 4.11 for different Q3D angles and polarities respectively. Although these spectra are not normalised with respect to the number of interactions induced by the beam, which varies due to factors such as beam exposure time and beam current, the relative variation in the intensity of the peaks can be seen clearly in both examples.

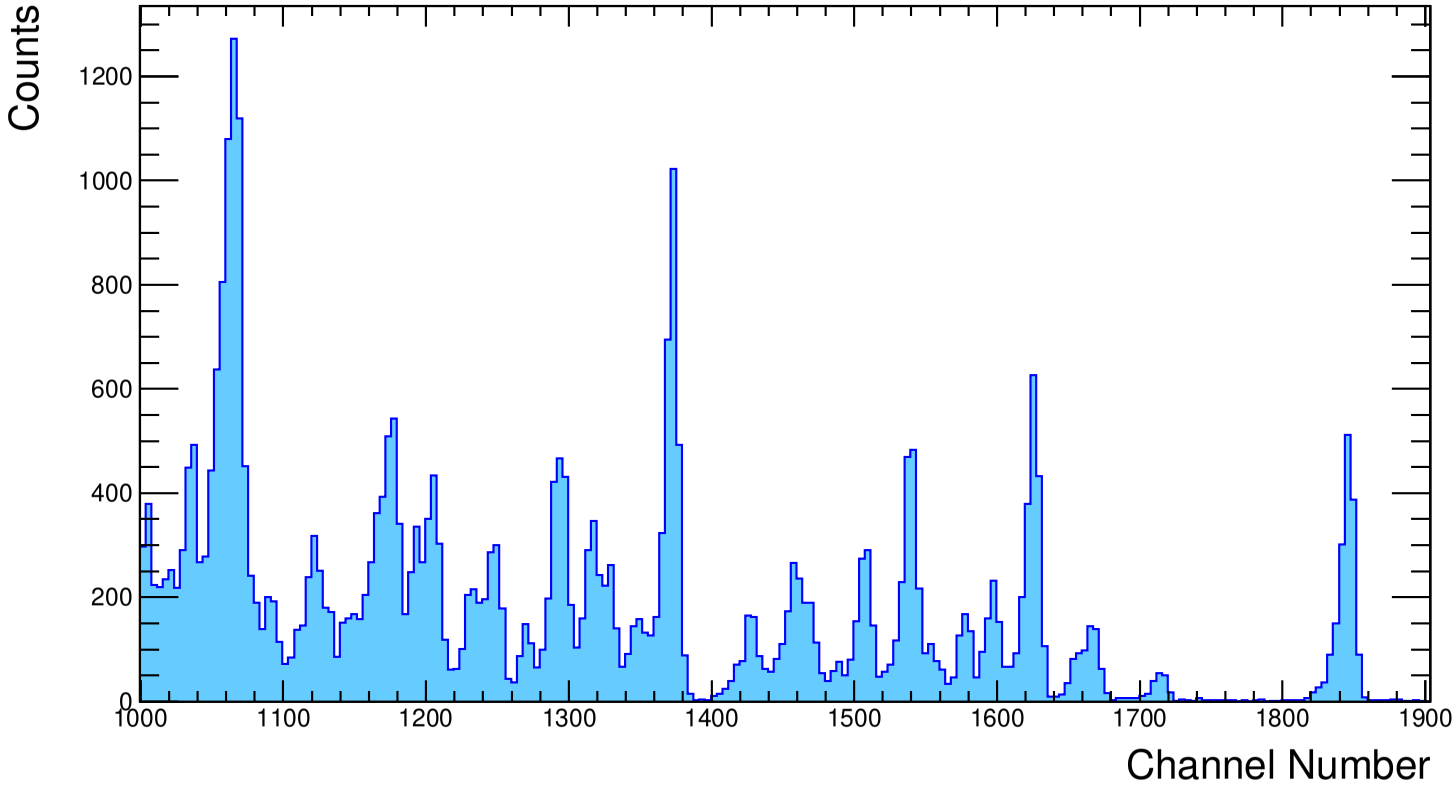


Figure 4.9: Plot showing the raw low-energy region of the ^{190}Re spectrum. As this is an α-particle ejectile spectrum a high channel number (and therefore high α-particle energy) corresponds to a low excitation energy for the residual ^{190}Re nucleus.

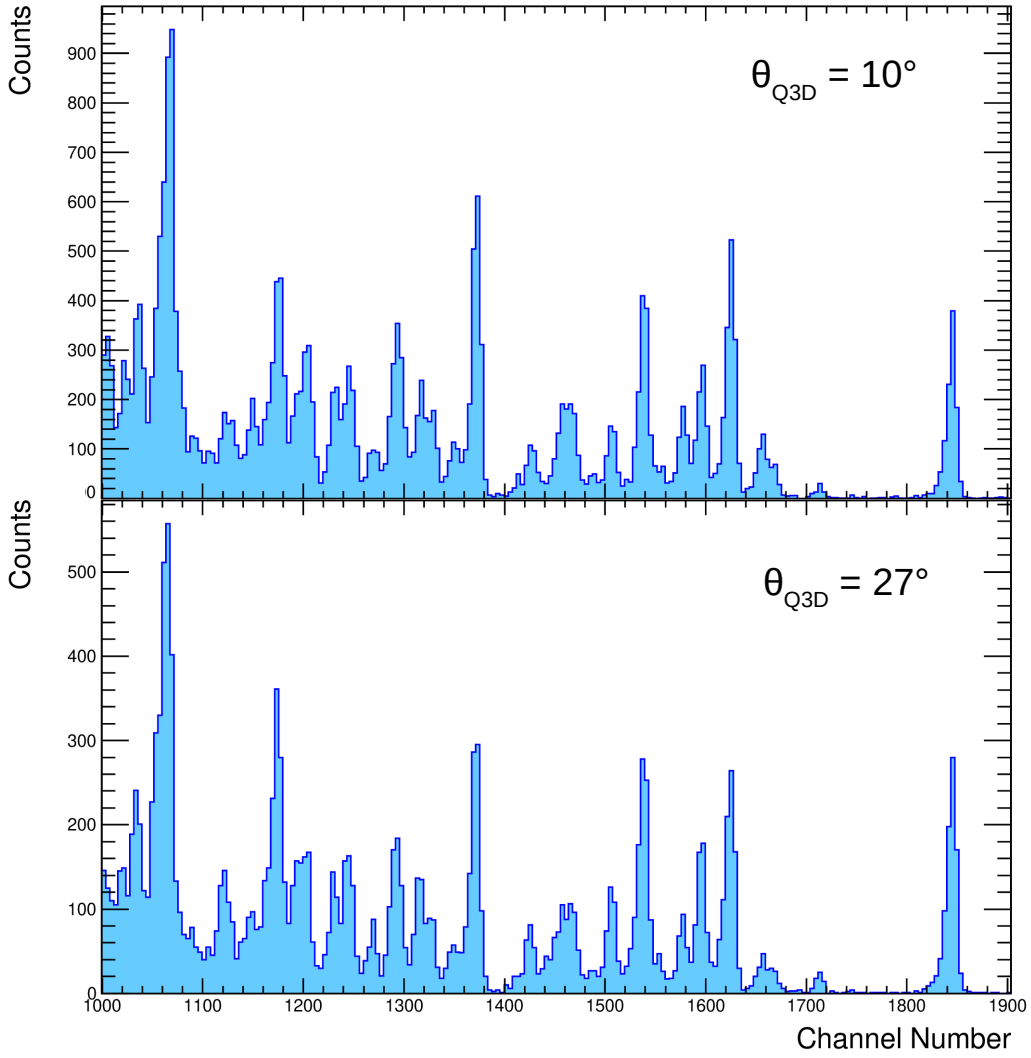


Figure 4.10: Plot showing the raw low-energy region of the ^{190}Re spectrum, measured with the Q3D magnetic spectrograph placed at 10° and 27° with respect to the beam axis. The spectra have *not* been normalised for the different beam exposures.

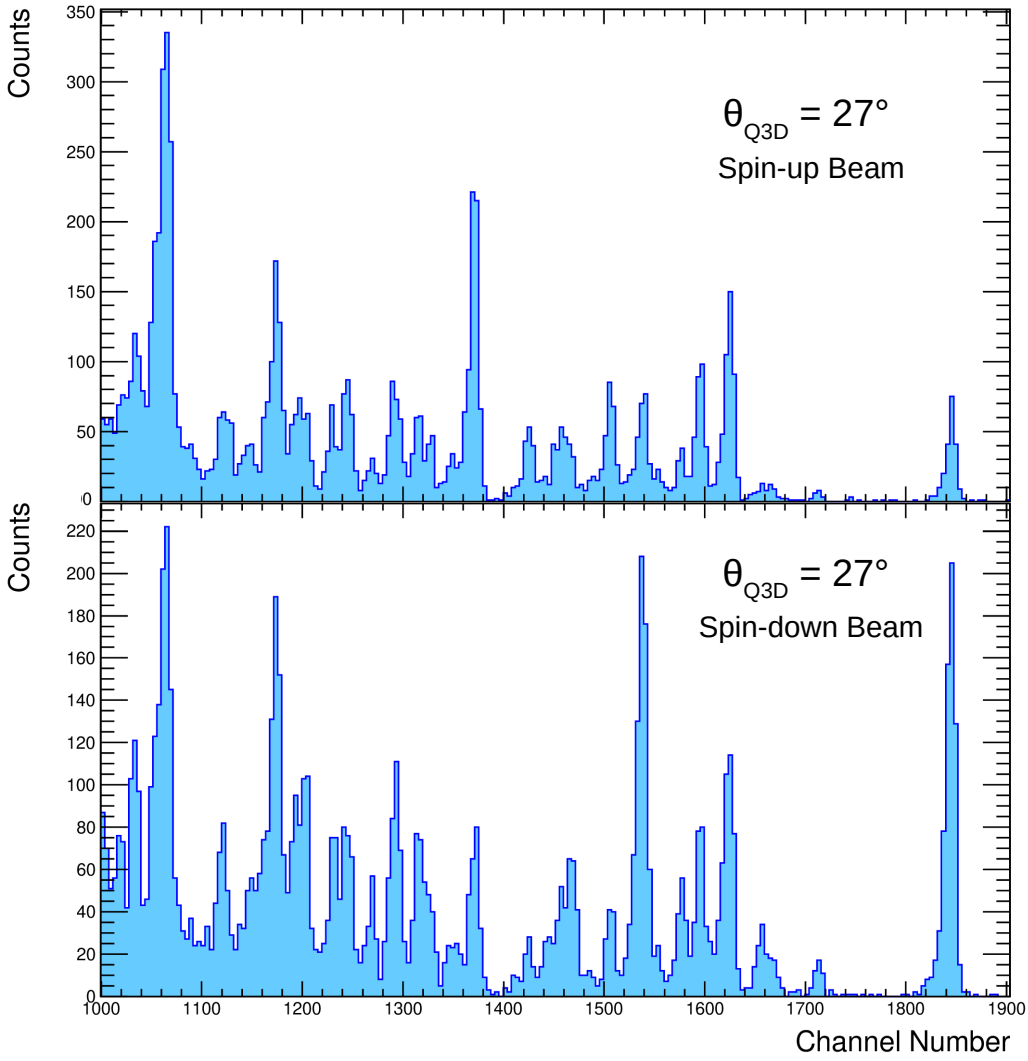


Figure 4.11: Plot showing the raw low-energy region of the ^{190}Re spectrum, measured with the Q3D magnetic spectrograph placed at 27° with respect to the beam axis with spin-up and spin-down deuteron beams used. The spectra have *not* been normalised for the different beam exposures.

Chapter 5

Atomic Mass Measurement

The first aim of this project was to measure the atomic mass of ^{190}Re to a higher precision than the previous literature value of 70 keV. Specifically, the aim is to reduce the uncertainty to below a value of 10 keV in order for use in astrophysical calculations (as explained in section 2.3). This chapter will detail the calculations and analysis performed in order to achieve this, present the subsequent results and discuss the implications and uses of this result.

5.1 Data Analysis

5.1.1 Mass Excess Calculations

As discussed in section 2.1.3, the Q-value of a reaction is the amount of energy taken in or given out during said reaction. This can easily be calculated from the difference in the mass excesses of the reactants and the products, given in units of energy, as shown in equation 2.4. As an example, two reactions with the same deuteron projectile and α-particle ejectile, $A(d,\alpha)C$ and $B(d,\alpha)D$ (referred to as reaction a) and reaction b) respectively), have Q-values given by the following:

$$Q_a = \Delta m_A + \Delta m_d - \Delta m_C - \Delta m_\alpha, \tag{5.1}$$

$$Q_b = \Delta m_B + \Delta m_d - \Delta m_D - \Delta m_\alpha. \tag{5.2}$$

Here, Δm_i represents the mass excess of isotope i. By combining these two equations the difference in the Q-value between reactions a) and b) can be found, symbolically represented by ΔQ_{ba}. This can be rearranged to give the mass excess of any of the reactants or products, if this is desired. As an example, the mass excess of product C in reaction a) can be found as follows:

$$\Delta Q_{ba} = \Delta m_B - \Delta m_A + \Delta m_C - \Delta m_D, \tag{5.3}$$

$$\implies \Delta m_C = \Delta Q_{ba} + \Delta m_A - \Delta m_B + \Delta m_D. \tag{5.4}$$

This equation can be applied to the two reactions used in this experiment, with reaction a) becoming ^{192}Os(d,α)^{190}Re and reaction b) becoming ^{194}Pt(d,α)^{192}Ir so that $A = {}^{190}$Os, $B = {}^{194}$Pt, $C = {}^{190}$Re and $D = {}^{192}$Ir. Therefore, the mass excess of ^{190}Re can be expressed as follows:

$$\Delta m_{Re} = \Delta Q_{ba} + \Delta m_{Os} - \Delta m_{Pt} + \Delta m_{Ir}. \tag{5.5}$$

All the mass excesses used in this calculation (apart from Δm_{Re}, which is to be determined) have known literature values with an uncertainty below 10 keV [64] which will be tabulated and discussed in detail later in this chapter. The mass excesses in equation 5.5 can be replaced with the atomic mass for each of the nuclei, if this is desired.

In order to find the mass excess/atomic mass of ^{190}Re the difference in Q-value between the ^{194}Pt(d,α)^{192}Ir and ^{192}Os(d,α)^{190}Re reactions needs to be calculated,

as this is the final unknown in equation 5.5. This can be found by calculating the total energy of the reactants and products of each reaction and comparing them. Returning to the generic case with reactions a) and b) being $A(d,\alpha)C$ and $B(d,\alpha)D$ respectively, the equation for the difference in Q-value between the reactions is given by

$$\begin{aligned}\Delta Q_{ba} &= E_{\alpha(b)} + E_D - E_D^* - E_{\alpha(a)} - E_C + E_C^* \\ &= \Delta_{E_{\alpha(ba)}} + \Delta_{E_{DC}} - E_D^* + E_C^*, \end{aligned} \tag{5.6}$$

where E_α is the measured energy of the α-particle ejectile for either reaction a) or b), E_C and E_D are the recoil energies of the residual nuclei and E_C^* and E_D^* are the energies of the excited states the residual nuclei have been produced in. This can be simplified by introducing terms for the difference in the energy of the α-particle ejectiles ($\Delta_{E_\alpha} = E_{\alpha(b)} - E_{\alpha(a)}$) and the difference in energy between the two residual nuclei ($\Delta_{E_{DC}} = E_D - E_C$). This problem is further simplified if it is assumed that C and D are produced in their ground states, as the excitation energies of the residual nuclei do not need to be taken into account. Returning to the specific reactions used in this experiment, and assuming ^{190}Re and ^{192}Ir are produced in their ground states, the equation becomes

$$\Delta Q_{ba} = \Delta_{E_\alpha} + \Delta_{E_{IrRe}}. \tag{5.7}$$

The difference in α-particle ejectile energy can be found by comparing the measured ^{192}Ir and ^{190}Re spectra along with the previously obtained energy calibration. The

difference in recoil energies between the two residual nuclei can be calculated using non-relativistic two-body kinematic calculations.

5.1.2 Kinematics and Recoil Energy

For a reaction, $P_1(P_0, P_2)P_3$, where a projectile (particle 0) is incident on a target (particle 1), producing a light ejectile (particle 2) and a heavy residual nucleus (particle 3) at angles of θ and ϕ with respect to the direction of the projectile respectively, the conservation of energy and momentum can be used to form the following equations:

$$E_0 + Q = E_2 + E_3 + E^* = E_{tot} + E^*, \tag{5.8}$$

$$p_0 = p_2 \cos\theta + p_3 \cos\phi, \tag{5.9}$$

$$0 = p_2 \sin\theta - p_3 \sin\phi. \tag{5.10}$$

Here, E_i and p_i are the energy and momentum of particle i respectively, Q is the Q-value of the reaction, and E^* is the total excitation energy of the products of the reaction. Rearranging and combining these equations can be used to give the momentum of the ejectile particle [83]:

$$p_2 = \frac{2p_0 \cos\theta \pm \sqrt{4p_0^2 \cos\theta - 4(1 + \frac{m_3}{m_2})(p_0^2 - 2m_3 E_{tot})}}{2(1 + \frac{m_3}{m_2})}. \tag{5.11}$$

From here, the energy and momentum for the residual nucleus can easily be found:

$$E_{tot} = Q + E_0 - E^*, \tag{5.12}$$

$$E_2 = \frac{p_2^2}{2m_2}, \tag{5.13}$$

$$E_3 = E_{tot} - E_2, \tag{5.14}$$

$$p_3 = \sqrt{2m_3E_3}. \tag{5.15}$$

If the products are both produced in their ground states, $E^* = 0$, this simplifies equation 5.8 so that only the beam energy and momentum (E_0, p_0), the Q-value of the reaction (Q) and the masses of the two outgoing particles (m_2, m_3) need to be known in order to calculate the energies and momenta of the two outgoing particles.

This method was used to calculate the recoil energies for the ^{192}Ir and ^{190}Re nuclei. It was found that $E_{Re} = 152.743\,\text{keV}$ (the calculation is shown in appendix A) and $E_{Ir} = 154.793\,\text{keV}$. In both cases the errors are negligible (<eV) compared to other components of the ^{190}Re atomic mass calculation. This results in a difference in recoil energy of $\Delta_{E_{Ir-Re}} = 2.050\,\text{keV}$.

Although this calculation relies on knowledge of the mass of ^{190}Re, which may seem illogical as this experiment is aiming to measure this value, the uncertainty in the current literature value for the mass does not contribute significantly to the overall uncertainty on the recoil energy so this is not an issue (as is demonstrated in appendix A). This is because the percentage uncertainty on the atomic mass of

^{190}Re is negligible and the recoil energy is small compared to the mass. This value for the recoil-energy difference can now be used in equation 5.7 in order to calculate the difference in Q-value between the two reactions performed in this experiment.

5.1.3 Low-Energy Rhenium-190 Structure

The next step in calculating the difference in Q-value between the two reactions performed as part of this experiment is to find the difference in the energy of the α-particle ejectiles produced. In order to do this, first the low-energy region of the ^{190}Re spectrum needed to be fitted, as the ^{192}Ir spectrum was in section 4.4.2 for the calibration.

It was observed that the two lowest-energy peaks in the ^{190}Re spectrum were slightly skewed and therefore could not be accurately fitted using a Gaussian distribution. This effect is sometimes observed in peaks at the extremes of spectra and beyond the main body of peaks when measuring using the Q3D. To fit a skewed Gaussian, a different equation was used. This equation is formed by introducing a cumulative distribution function with a shape parameter, α, given by

$$\Phi(\alpha x) = \int_{-\infty}^{\alpha x} \phi(t)dt = \frac{1}{2}\left[1 + \mathrm{erf}\left(\frac{\alpha x}{\sqrt{2}}\right)\right], \tag{5.16}$$

where $\phi(x)$ is the typical Gaussian distribution function, given by

$$\phi(x) = \frac{a}{\sqrt{2\pi}} \exp\left[-\frac{(x-b)^2}{2c^2}\right]. \tag{5.17}$$

Here, a, b and c give the height, mean and standard deviation of the peak respectively. Equation 5.16 makes use of the error function, defined as

$$\text{erf}(x) = \frac{2}{\sqrt{\pi}} \int_0^x e^{-t^2} dt. \tag{5.18}$$

This corresponds to the area under the Gaussian curve between $-x$ and x. The probability density function for the skewed-normal distribution is given by $f(x) = 2\phi(x)\Phi(\alpha x)$ [84]. Therefore, the equation used to fit skewed Gaussian peaks in this study is then given by

$$f(x) = \frac{a}{\sqrt{2\pi}} \exp\left[-\frac{(x-b)^2}{2c^2}\right] \left[1 + \text{erf}\left(\frac{\alpha x}{\sqrt{2}}\right)\right]. \tag{5.19}$$

Using both equation 5.19 and the equation for an unskewed Gaussian, the low-energy region of the ^{190}Re spectrum was fitted. This can be seen below in figure 5.1. This is the same spectrum as shown in figure 4.9, generated using data from the same runs, but with a fit performed. Here, the mode of the distribution used to fit the skewed peaks was taken as their centroid value.

The skew of the two lowest energy (and therefore highest channel number) peaks can be clearly seen in figure 5.1. The remaining two peaks in the figure were fitted

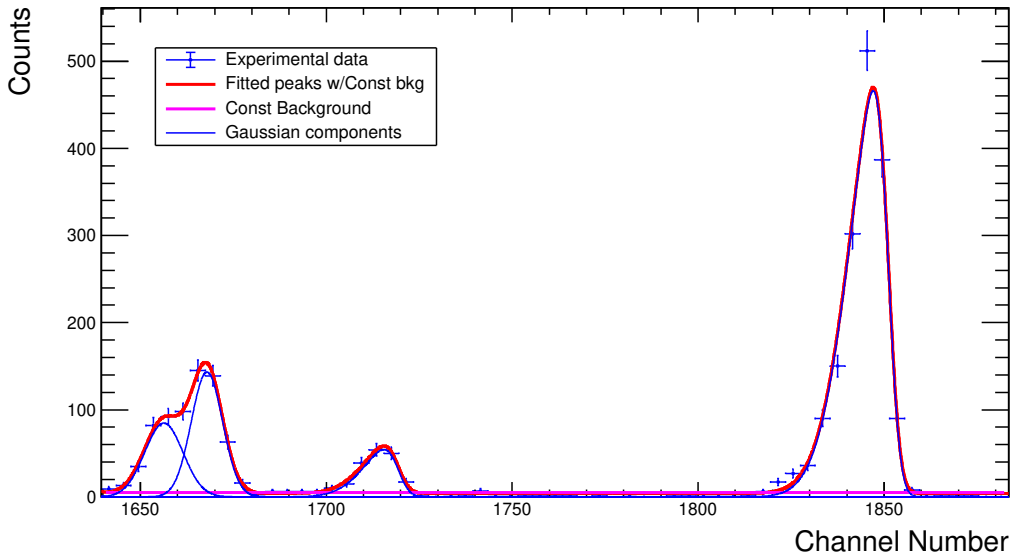


Figure 5.1: The low energy region of the ^{190}Re spectrum, measured using α-particle ejectiles from the ^{192}Os(d,α)^{190}Re reaction. The rightmost two peaks have been fitted as skewed Gaussians, with the other peaks fitted as standard Gaussians.

using regular Gaussian distributions. Based on the current $I^{\pi} = (2)^{-}$ assignment for the ground state of ^{190}Re, it was expected that this state will be populated in the experiment. Therefore, it was decided that the rightmost peak in the spectrum was the ground state. This assumption was checked by extracting the energy of the second peak from the right and comparing to the known levels of ^{190}Re (as shown in figure 5.2 in section 5.1.4). This could now be compared with the ^{192}Ir spectrum in order to find a value for Δ_{E_α} in equation 5.7.

5.1.4 Combined Spectrum

To find the difference in the energy of α-particles emitted in the ^{192}Os(d,α)^{190}Re and ^{194}Pt(d,α)^{192}Ir reactions, excitation energies together with the beam energy can be used with kinematic calculations to convert channel number to energy. Standard

kinematics can then be used to subsequently convert this to the α-particle ejectile energy. This is a simple process using equations given in section 5.1.2. Once this has been done, it is straightforward to calculate the difference in α-particle ejectile energies for states produced in the two reactions as the fits of the peaks in the spectra will give these energies.

A complication with this process was that the ^{192}Ir ground state was not populated in this experiment due to its $I^{\pi} = 4^{+}$ configuration being incompatible with the ground-state configuration of the ^{194}Pt target. However, this could be calculated by extrapolating the calibration to find the ejectile energy corresponding to an excitation energy of 0 keV in ^{192}Ir. The difference in α-ejectile energy between this point and ^{190}Re could then be easily found. Although this extrapolation introduced uncertainty, the fact that the excitation energy of the ground state was known by definition to be 0 keV means that this method introduced the least amount of overall uncertainty into the calculation. A plot of the two spectra overlaid on the same axes, with the x-axis showing both the channel number and the corresponding ejectile energy, is shown in figure 5.2

The two lowest energy peaks in the ^{190}Re spectrum, the ground state and the first excited state, have been included in figure 5.2 and are labelled. The fitted value of the first excited state in ^{190}Re was found to be 119.2 ± 0.7 keV, which is in agreement with the current literature value of 119.12 ± 0.05 keV [55]. In this figure, the difference in energy between an α-particle ejectile corresponding to the

ground states in ^{190}Re and ^{192}Ir (shown by a dashed line) can clearly be seen. This was calculated to be $\Delta_{E_\alpha} = 373 \pm 4$ keV. This is significant as the uncertainty is lower than 10 keV and therefore this value alone will not prevent the uncertainty in the calculated atomic mass of ^{190}Re being below the value of 10 keV important for astrophysical models.

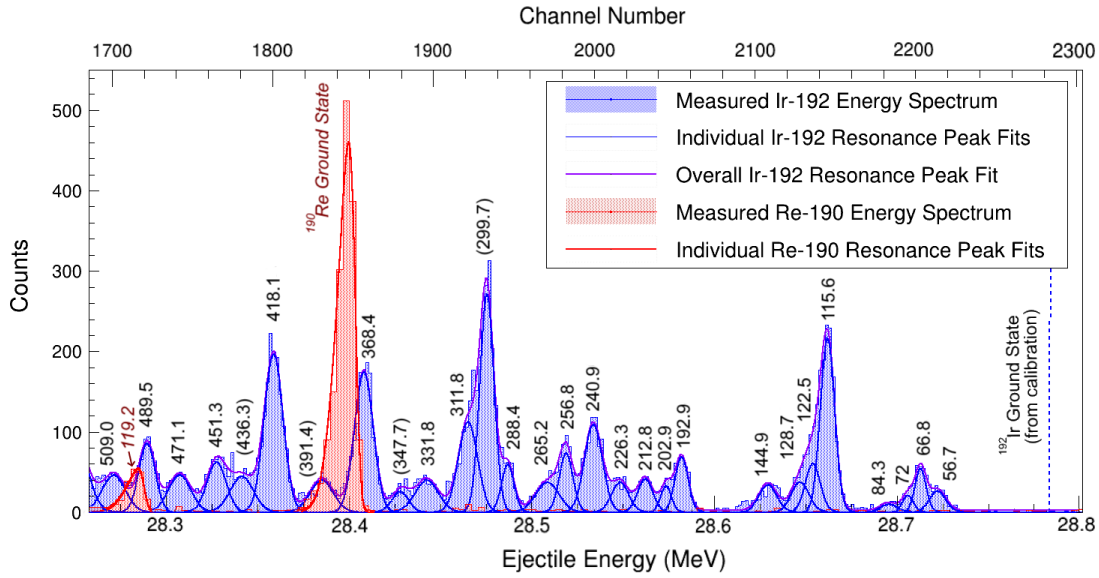


Figure 5.2: Fitted low-energy region of the ^{192}Ir energy spectrum, with the excitation energies of peaks used in the calibration labelled in keV [70, 85] and those omitted due to comprising multiple close-lying resonances labelled in brackets. The plot shows both the ejectile (α-particle) energy and the corresponding channel number for the focal plane detector on the x-axes. Here, a higher value of channel number corresponds to a lower excitation energy since ejectile energy is being measured. The fitted ground-state and first excited-state peaks in ^{190}Re have been overlaid and labelled in red. The position of the ^{192}Ir ground state (found using the calibration) is also indicated, but was not populated due to its $I^\pi = 4^+$ configuration being incompatible with the ^{194}Pt target ground-state configuration [28]. Figure and caption taken from reference [86].

5.2 Results and Discussion

5.2.1 Atomic Mass Results

Using equation 5.7 and the values $\Delta_{E_\alpha} = 373 \pm 4\,\text{keV}$ and $\Delta_{E_{IrRe}} = 2\,\text{keV}$ (rounded, with negligible error compared to that of Δ_{E_α}), yields a value of $\Delta Q_{IrRe} = 375 \pm 4\,\text{keV}$. Using this Q-value difference, values for the mass excess, atomic mass and binding energy per nucleon for ^{190}Re can be calculated using equations detailed in section 5.1.1. Table 5.1 shows the values used in these calculations.

Table 5.1: Values used to calculate the mass excess of ^{190}Re using equation 5.5. The value for ΔQ_{IrRe} was found in this experiment, with the mass excess values taken from reference [64]. These values are unchanged in the most up to date atomic mass evaluation [87].

$\mathbf{\Delta Q_{IrRe}}$ **(keV)**	$\mathbf{\Delta m_{Pt}}$ **(keV)**	$\mathbf{\Delta m_{Os}}$ **(keV)**	$\mathbf{\Delta m_{Ir}}$ **(keV)**
375 ± 4	-34760.1 ± 0.5	-35882.3 ± 2.3	-34835.6 ± 1.3

In table 5.2, the values calculated as part of this experiment (the mass excess, atomic mass and binding energy per nucleon for ^{190}Re) are displayed alongside previous literature values. From this it is clear that the results of this experiment lie within the uncertainty of the previous values which shows the two sets of results are in agreement. The results are also within the uncertainty of all previously reported measurements, given in table 3.2. The uncertainty in all of the values has been reduced significantly, in each case being over an order of magnitude lower than the literature values.

Table 5.2: Properties of ^{190}Re calculated using the results of this experiment [86], shown alongside known literature values from reference [64]. These values are unchanged in the most recent atomic mass evaluation [87].

	Mass Excess (keV)	**Atomic Mass (keV)**	**Atomic Mass (μu)**	**Binding Energy per Nucleon (keV)**
Current Work	-35583 ± 5	1796948297 ± 5	189961800 ± 5	7949.78 ± 0.03
Literature	-35640 ± 70	1796948240 ± 70	189961740 ± 80	7950.1 ± 0.4

5.2.2 Uncertainty Calculations

The uncertainties in the literature values of the mass excesses of ^{192}Ir, ^{192}Os and ^{194}Pt (the other nuclei involved in this experiment) are 1.3 keV, 2.3 keV and 0.5 keV respectively as shown in table 5.1. From equation 5.5, it can be seen these values affect the uncertainty in the mass excess, and therefore the atomic mass and binding energy, of ^{190}Re calculated in this experiment. As it is largest, the uncertainty in the mass excess of ^{192}Os is clearly most significant.

The other source of error in this experiment is the method used to find the difference in Q-value between the two reactions. As previously mentioned, the ground state of ^{192}Ir was not populated in this experiment. In order to find the difference in energy of the ^{192}Ir and ^{190}Re ground states the calibration was extrapolated beyond the peaks used to perform the calibration itself in order to find where the ground state of ^{192}Ir would be expected, had it been populated. This extrapolation introduces uncertainty into the position of the ^{192}Ir ground state that is carried forward to the value of the mass excess of ^{190}Re. An alternative method for finding the difference

in Q-value which does not involve extrapolation is to find the difference between an excited state in ^{192}Ir, such as the ^{192m1}Ir isomeric state at 56.72 keV (or any other well-populated state), and the ground state in ^{190}Re before accounting for this excitation energy. However, the uncertainty introduced by fitting the peak in ^{192}Ir and the uncertainty in the energy of the state itself (although often negligible) results in no overall reduction in uncertainty using this method. The fit of the ground state peak in ^{190}Re also yields an uncertainty of ± 0.5 keV which must be included in the overall uncertainty in the Q-value difference which, as previously stated, was calculated to be ± 4 keV.

In this experiment, ^{192}Ir was used to perform the calibration as it has similar proton and mass numbers to ^{190}Re and both can be produced via (d, α) reactions. However, the level density in some regions of the ^{192}Ir energy spectrum is high and the spectrum is quite complex overall, as can be seen in figures 4.7 and 5.2. It is for this reason that ^{192}Ir is not ideal for performing a calibration. As the statistics for the ^{192}Ir spectrum are also relatively low, the error on centroid values for the fitted peaks is significant, introducing uncertainty to the calibration and any values calculated using it. In order to further reduce the uncertainty in ^{190}Re calculated using this method, a different calibration reaction using a nucleus with a lower level density and with high statistics is required. The mass of ^{192}Os could also independently be measured to a higher precision.

5.3 Discussion and Outcomes

As has been discussed previously, uncertainty in the value of the mass excess of ^{190}Re has been reduced to 5 keV from the previous literature value of 70 keV. Not only is this an impressive result from a nuclear data point of view, it is also significant as the uncertainty has been reduced to below 10 keV. As discussed in section 2.3.1 this is important for models of astrophysical processes, such as the r-process, as it ensures that uncertainties in nuclei produced via such processes do not dominate reaction rate uncertainties.

Since these results have been published, the updated ^{190}Re mass excess measurement has been used, alongside other work, to reduce the uncertainty in the literature value for the Q-value of the β^- decay of ^{190}W into ^{190}Re [55]. It has also been used to reduce the uncertainty in several properties of ^{190}Re itself, such as the Q-value of the β^- decay into ^{190}Os and the α-decay into ^{186}Ta. The values for the single proton and neutron separation energies for ^{190}Re have also seen reductions in their uncertainties as a result of this work. This demonstrates why measuring the mass of nuclei accurately is important, as it can lead to the reduction in the uncertainty of several more nuclear properties as a result.

As can be seen from table 5.1, the most significant source of uncertainty from this experiment is from the measurement of the Q-value difference between the two reactions used and not the masses of the other nuclei involved. Therefore, there is

scope to further constrain the atomic mass of ^{190}Re using this method, potentially by using a different calibration reaction or by measuring for longer to increase the statistics. It may also be possible to reduce the uncertainty in the atomic mass measurement by using an ion trapping method [88], although such a method would not yield information on the energy-level structure in ^{190}Re.

Chapter 6

Energy-Level Structure Investigations

The second stage of this project involved investigating the energy-level structure of ^{190}Re. As detailed in section 3.2, only five states (including the ground state) in ^{190}Re are currently known, with their properties established to varying degrees of accuracy. It can be seen in ^{190}Re spectra produced in this project, such as in figure 4.9, that many more states in ^{190}Re have been observed through this experiment. For these unknown states, the aim is to elucidate the excitation energy, spin and parity. For the five currently known states, the aim is to either measure their properties to a higher degree of precision where possible, or to confirm/update the previously assigned values.

6.1 Excitation Energies

To find the energies of the observed excited states in ^{190}Re the measured spectrum was fitted beyond the low-energy region shown in figure 5.1. Then, the fitted values (given in channel number) were converted to an energy using the ^{192}Ir calibration detailed in section 4.4.2. The difference in α-particle ejectile energies between the ^{194}Pt(d,α)^{192}Ir and ^{192}Os(d,α)^{190}Re reactions, calculated in section 5.1.4, was used to convert these energies from corresponding to excitation energies for the ^{192}Ir residual nucleus to the desired ^{190}Re residual nucleus.

The ^{190}Re spectrum was fitted up to an excitation energy of $\sim 1000\,\text{keV}$. For this fit the background was taken to be linear as the excitation energies are below the neutron-decay threshold of $S(n) = 5675 \pm 10\,\text{keV}$ [55], above which a more complex background function would be required due to three-body contributions from neutron decay of the recoiling nucleus. Although the Q-value for the $(^{190}\text{Re},\alpha)^{186}\text{Ta}$ decay is $0.60 \pm 0.02\,\text{MeV}$, kinematic calculations can be used to calculate penetrabilities through the Coulomb barrier which demonstrate that this channel is not significant below 1000 keV.

In this region a total of 57 distinct peaks were fitted and assigned energies using the calibration. Most notable are the peaks corresponding to previously known states in ^{190}Re. These are the ground state, the state at 119.12 keV (measured to be $119.2 \pm 0.7\,\text{keV}$ in this study), shown and discussed previously in section 5.1.4, and two other states previously reported to have energies of $204 \pm 10\,\text{keV}$ (the ^{190m}Re state) and $319.70 \pm 0.15\,\text{keV}$. The energies of these peaks were found to be 205.8 keV and 317.1 keV respectively, although the $204 \pm 10\,\text{keV}$ could also be another state found to have an energy of 212.5 keV due to the large uncertainty in the literature value. Note that the 162.1 ± 0.1 keV state in ^{190}Re was not populated in this experiment due to its 0^+ spin/parity configuration and was therefore not observed, as shown by its absence in table 6.2 in section 6.2.2.

The current calibration, used for the mass measurement calculations shown in chapter 5, was calculated using peaks in the ^{192}Ir spectrum above channel number

of 1700. Peaks below this point were not included in the calibration due to the high level-degeneracy in the higher-energy regions of the ^{192}Ir spectrum making fitting and assigning energies to peaks difficult, introducing uncertainty. However, as the fitted ^{190}Re spectrum extends to a channel number of around 800, the calibration was extrapolated for most of the ^{190}Re spectrum. As some peaks in the ^{190}Re spectrum have been assigned to known energy levels, these can be included in the calibration to improve its accuracy in higher energy regions. The new calibration with the ground state, $119.12 \pm 0.05\,\text{keV}$ and $319.70 \pm 0.15\,\text{keV}$ states included is shown in figure 6.1.

As expected, the accuracy of the new calibration for the known states in the ^{190}Re spectrum is improved. The fit of the $119.12 \pm 0.05\,\text{keV}$ and $319.70 \pm 0.15\,\text{keV}$ states are now $119.34 \pm 0.50\,\text{keV}$ and $319.05 \pm 0.57\,\text{keV}$ respectively, showing better agreement with the literature values than when using the initial calibration. As the lower channel number (and therefore higher energy) peaks in the ^{190}Re have now been considered, this spectrum introduces less uncertainty due to the extrapolation than the previous calibration. This calibration also gives the same Δ_{E_α} value, discussed in section 5.1.1, as the previous calibration which means that the atomic mass of ^{190}Re calculated in chapter 5 is still valid for this calibration. The fitted ^{190}Re spectrum up to an excitation energy of $\sim 1000\,\text{keV}$, with peaks labelled according to their energy given using the new calibration in units of keV, is shown in figure 6.2. As discussed above, the background in this region was taken to be linear.

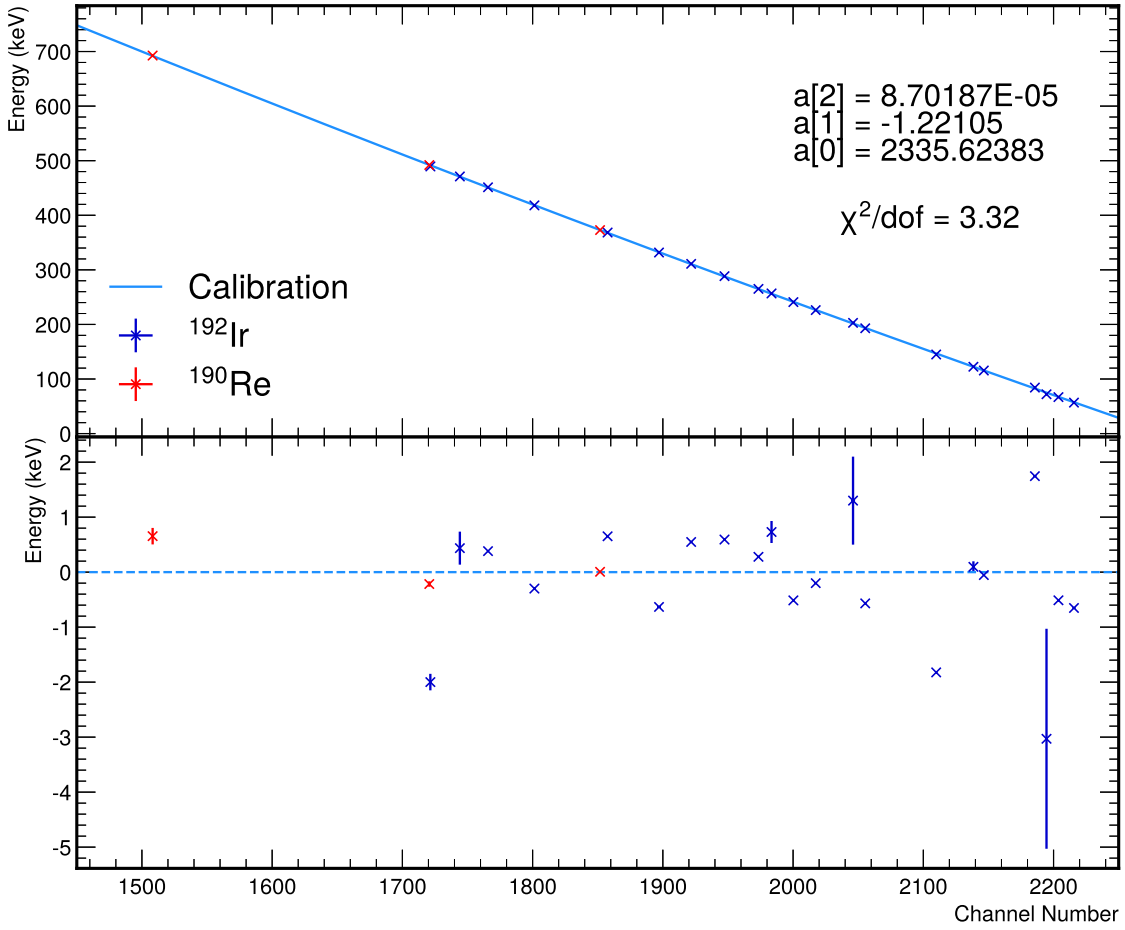


Figure 6.1: Plot showing the updated energy calibration for the focal plane detector of the Q3D magnetic spectrograph, including known energy levels in ^{190}Re. These states have been given energies corresponding to equivalent α-particle ejectile energies for the ^{194}Pt(d,α)^{192}Ir so that they are consistent with the rest of the points in the calibration. The second plot gives the residuals of the calibration.

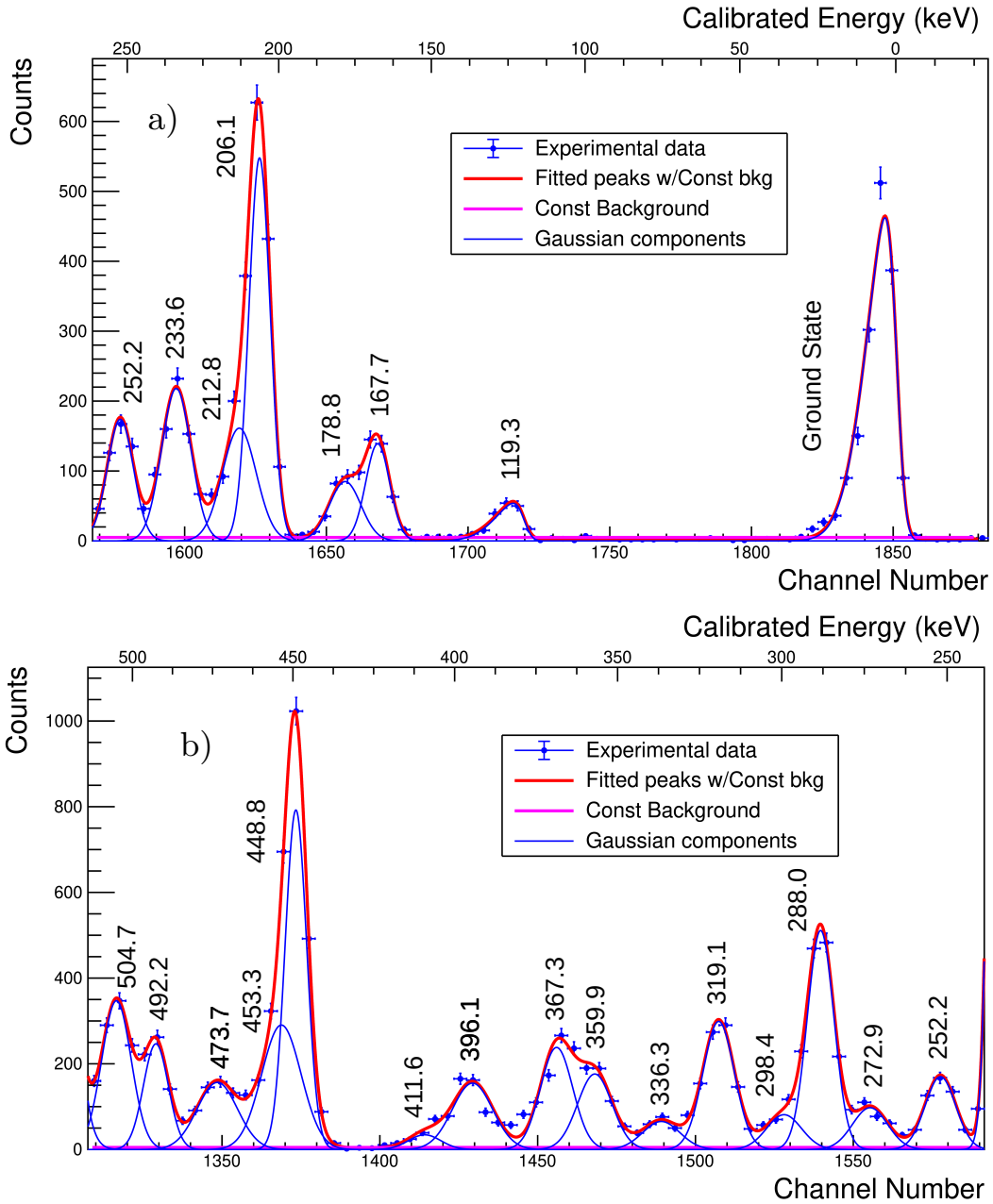


Figure 6.2: Figure continues on next page.

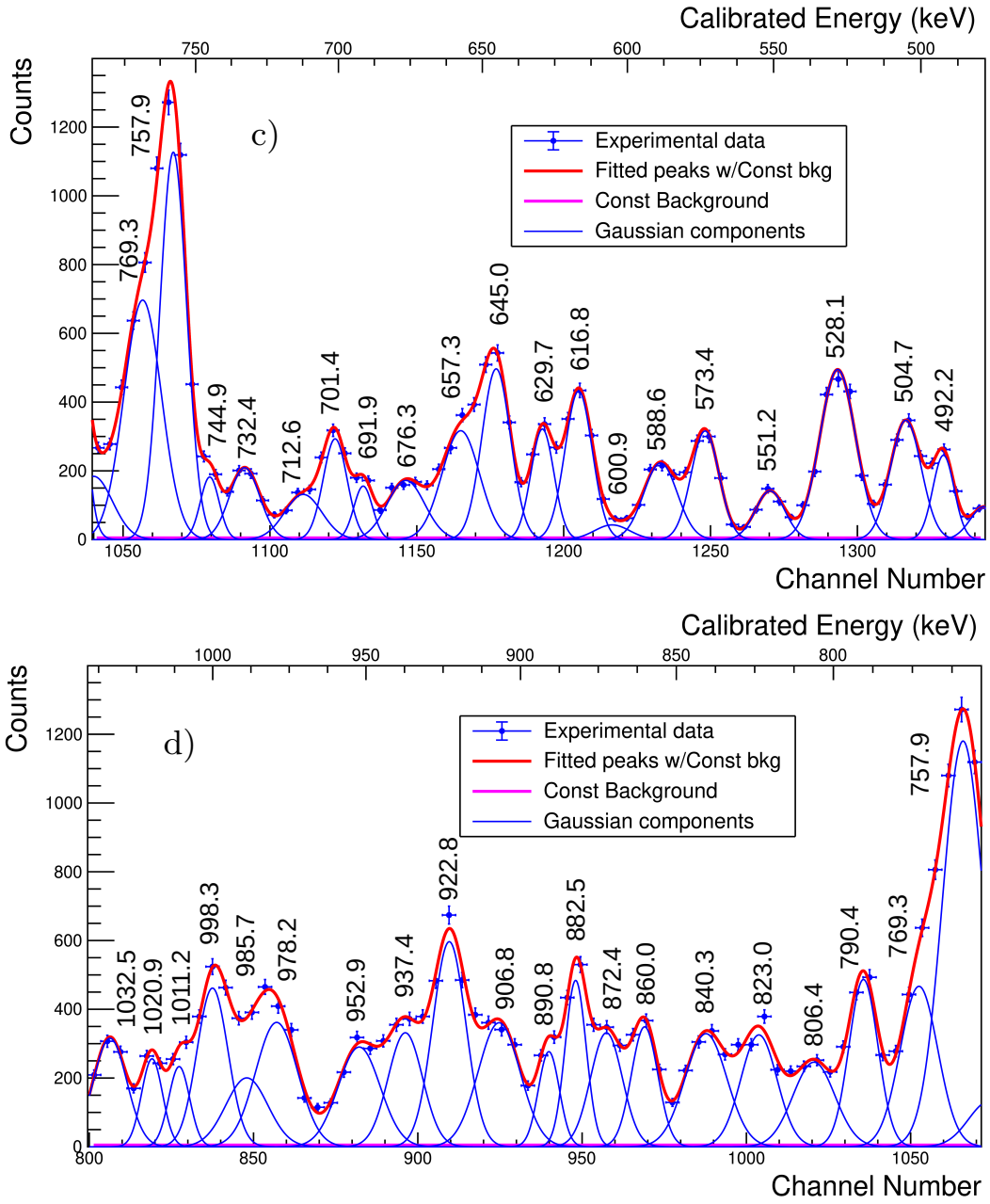


Figure 6.2: Plot showing fitted regions of the ^{190}Re spectrum. As the detector was used to measure the energy of α-particle ejectiles produced in the ^{192}Os(d,α)^{Re}Re reaction, a high channel number (and therefore high α-particle energy) corresponds to a low excitation energy for the residual ^{190}Re nucleus. Each peak is labelled with its calibrated energy. Shown are the a) ∼0 - 250 keV, b) ∼250 - 500 keV, c) ∼500 - 750 keV and d) ∼750 - 1000 keV regions of the spectrum.

Table 6.1: Table showing the measured energy levels in ^{190}Re and the corresponding channel numbers from the fit of figure 6.2. The calibration used to convert between these values is shown in figure 6.1.

Energy (keV)	**Error (keV)**	**Channel Number**	**Error**		**Energy (keV)**	**Error (keV)**	**Channel Number**	**Error**
0.00	0.36	1851.79	0.18		645.04	1.42	1178.05	0.42
119.34	0.50	1720.67	0.40		657.30	1.77	1165.99	1.07
167.71	0.47	1668.45	0.33		676.28	1.60	1147.38	0.64
178.80	0.55	1656.54	0.44		691.87	1.59	1132.14	0.49
206.07	0.41	1627.39	0.14		701.40	1.61	1122.84	0.45
212.82	0.70	1620.19	0.61		712.56	2.27	1111.97	1.58
233.62	0.48	1598.09	0.25		732.35	1.70	1092.74	0.37
252.21	0.49	1578.41	0.25		744.86	1.77	1080.61	0.46
272.91	0.67	1556.58	0.51		757.92	1.77	1067.98	0.23
288.01	0.51	1540.71	0.18		769.31	1.87	1056.99	0.52
298.42	1.01	1529.80	0.92		790.44	1.90	1036.65	0.30
319.05	0.57	1508.23	0.21		806.41	2.04	1021.33	0.61
336.28	0.88	1490.29	0.71		823.04	2.06	1005.41	0.46
359.94	0.77	1465.74	0.49		840.25	2.12	988.98	0.44
367.31	0.77	1458.11	0.48		860.00	2.28	970.18	0.72
396.13	0.77	1428.40	0.38		872.41	2.33	958.40	0.72
411.59	1.29	1412.52	1.11		882.50	2.28	948.83	0.41
448.79	0.81	1374.51	0.15		890.83	2.31	940.95	0.38
453.34	0.92	1369.87	0.46		906.82	2.40	925.84	0.50
473.65	0.98	1349.24	0.49		922.83	2.48	910.76	0.53
492.17	0.95	1330.50	0.31		937.41	2.63	897.05	0.84
504.72	0.97	1317.83	0.26		952.93	2.70	882.49	0.84
528.12	1.01	1294.28	0.17		978.19	2.87	858.88	1.00
551.24	1.11	1271.11	0.31		985.70	2.79	851.87	0.70
573.38	1.19	1249.01	0.38		998.25	2.81	840.18	0.54
588.58	1.26	1233.88	0.46		1011.02	2.95	828.32	0.84
600.93	2.16	1221.62	1.77		1020.85	2.88	819.20	0.41
616.76	1.30	1205.95	0.31		1032.53	2.92	808.37	0.30
629.67	1.35	1193.19	0.33					

The full list of fitted channel numbers and corresponding energies for each of the peaks, with error, is shown in table 6.1. The errors for the energies of these states was given by a combination of the uncertainty in the centroid values of the peaks from the fits and an assigned uncertainty from the extrapolation of the calibration. The extrapolation uncertainty was calculated by reperforming the calibration with the channel number of the $319.70 \pm 0.15\,\mathrm{keV}$ state varied by $\pm 2\sigma$, where σ is the centroid error from fitting the peak. This was done as it was observed that the nature of the extrapolation was weighted heavily by the position of this point. The energies for each point given by these calibrations were then used to calculate the extrapolation error.

6.2 Spin and Parity

In order to elucidate the spin and parity of the observed excited states in ^{190}Re, measured values of the differential cross section and analysing power needed to be compared to calculated values for a variety of spin and parity configurations. The process of calculating the measured values from data collected by the experimental set-up will be detailed in this section, as will the process of calculating corresponding values from nuclear theory. These calculations will be compared to potentially deduce the spin and parity of the observed states in the energy-level structure of ^{190}Re.

6.2.1 Experimental Measurements

To calculate the overall differential cross section for a reaction producing a particular excited state at a certain angle, first the differential cross section for both the spin-up and the spin-down beams need to be calculated. For experiments performed at the Q3D magnetic spectrograph, these are given by the following:

$$\sigma_{\uparrow\downarrow} = \frac{d\sigma}{d\Omega}\left(\uparrow\downarrow\right) = \frac{N_{\uparrow\downarrow}}{N_b}\,\frac{1}{\Delta\Omega}\,\frac{M_{r(\text{target})}}{x\,N_A} \quad \text{cm}^2\,\text{msr}^{-1}\,, \tag{6.1}$$

where $N_{\uparrow\downarrow}$ is the number of counts in the peak (for either the spin up or spin down measurement) corresponding to the state, N_b is the total number of particles in the beam over the course of the runs, $\Delta\Omega$ is the opening angle of the slits on the Q3D detector used to control the solid angle acceptance in units of millisteradians (msr), $M_{r(\text{target})}$ is the atomic mass number of the target, x is the thickness of the target in units of $\text{g}\,\text{cm}^{-2}$ and N_A is Avogadro's constant. For this experiment, the Q3D slits were wide open so that $\Delta\Omega = 15$ msr. For the ^{192}Os target the atomic mass number is $M_{r(\text{target})} = 192$ and the thickness of the target, as stated in section 4.2, is $x = 66\ \mu\text{g}\,\text{cm}^{-2}$.

The number of counts in each peak, $N_{\uparrow\downarrow}$, is given by the fit shown in figure 6.2. Information used to calculate the total number of particles in the beam, N_b, was given by the Brookhaven Instruments Faraday Cup Integrator (FCI). This was connected to a Faraday cup placed behind the target at 0° with respect to the beam axis. A large proportion of the beam did not interact with the target and was

therefore incident on the Faraday cup. The total current integrated on the Faraday cup was proportional to, and can therefore be used to calculate, N_b by converting the current recorded by the Faraday cup into digital pulses. The sum of these pulses is recorded as a quantity called scaler 1, the values of which for each run are shown in table 4.1. When the data acquisition system (DAQ) was busy processing an event, the detector was 'dead' (that is to say, signals received during this time were not be processed). During this dead time the Faraday cup pulses were recorded as a separate quantity called scaler 3, which is also given in table 4.1. The difference between these two values was used to give the dead-time corrected value for the integrated current on the Faraday cup, referred to as $\mathrm{SCA_{DT}} = \text{scaler 1} - \text{scaler 3}$, which can be used to calculate the number of particles in the beam as follows

$$N_b = \mathrm{SCA_{DT}} \frac{\mathrm{FS}}{1000\, e}, \tag{6.2}$$

where FS is the full scale setting, which was 2×10^{-6} for this experiment and e is the elementary charge. This means that, when the beam had a current of 2×10^{-6} A, the FCI sent 1000 pulses per second to the scalers. This scales linearly, so if the beam current was 1×10^{-6} A then 500 pulses per second were sent [89].

Once the spin-up and spin-down differential cross sections had been calculated, they could subsequently be used to calculate both the overall differential cross section and

the analysing power. These are given by

$$\frac{d\sigma}{d\Omega}(\theta) = \frac{\sigma_+(\theta) + \sigma_-(\theta)}{2}, \tag{6.3}$$

$$A_y(\theta) = \frac{2}{3P_y}\frac{\sigma_+(\theta) - \sigma_-(\theta)}{\sigma_+(\theta) + \sigma_-(\theta)} \quad [28]. \tag{6.4}$$

Here P_y is the vector polarisation of the beam, which was known to be 50% for the runs that utilised a polarised beam in this experiment. These values could be calculated for each of the observed states in the ^{190}Re spectrum shown in figure 6.2 for each angle at which data were measured ($10°, 15°, 21°$ and $27°$) and subsequently can be compared to theoretical calculations.

6.2.2 Theoretical Calculations and DWUCK4

To calculate the theoretical differential cross sections and analysing powers for various final state spin/parity configurations, different equations to those shown above in section 6.2.1 are required. These are, for a particular L transfer, as follows

$$\frac{d\sigma}{d\Omega}(\theta)^* = \sum_L G_{LJ}\,\sigma^{LJ}(\theta)\left[1 + \frac{1}{2}\,P_{yy}\,A_{yy}^{LJ}(\theta)\right], \tag{6.5}$$

$$A_y(\theta)^* = \sum_L G_{LJ}\,\sigma^{LJ}(\theta)A_y^{LJ}(\theta)\left[1 + \frac{1}{2}\,P_{yy}\,A_{yy}^{LJ}(\theta)\right]\frac{1}{d\sigma(\theta)/d\Omega^*}. \tag{6.6}$$

Here, J is the total momentum of the final state, G_{LJ} is the spectroscopic factor, σ_{LJ} is the theoretical cross section, P_{yy} is the tensor polarisation of the beam, A_{yy}^{LJ} is the

theoretical tensor analysing power and A_y^{LJ} is the theoretical vector analysing power. The spectroscopic factor gives the spectroscopic strength of a particular L transfer and is found by using a minimisation routine to fit the theoretical calculations to measured data. The theoretical values of σ_{LJ}, A_{yy}^{LJ} and A_y^{LJ} are calculated using the distorted-wave Born approximation (DWBA), as discussed in section 2.2.4.

A sum over multiple L states, as given in equations 6.5 and 6.6, are sometimes required as the population of unnatural parity states, where $\pi = -1^{J+1}$, can proceed via two different L transfers for the ^{192}Os($\vec{d}$,α)^{190}Re reaction (except for the $J^\pi = 0^-$ state which can only be populated by a $L = 1$ transfer). The allowed spin/parity configurations for the ^{190}Re final state for a range of different L transfers are shown below in table 6.2, clearly showing how two different L transfers can populate the same final state. These combinations of selection rules arise from coupling the deuteron ($I^\pi = 1^+$) with orbital angular momentum and the spin-zero positive parity ^{192}Os and ^{4}He ground states to generate the final state properties in ^{190}Re with J^π.

Table 6.2: The relation between spin/parity (J^π) configurations of states in ^{190}Re and allowed L transfers in the ^{192}Os($\vec{d}$,α)^{190}Re reaction. Here, states of natural parity are populated by the $L = J$ transfer and states of unnatural parity are populated by both the $L = J + 1$ and $L = J - 1$ transfers.

L	J^π			L	J^π			L	J^π		
0			1^+	3	2^-	3^-	4^-	6	5^+	6^+	7^+
1	0^-	1^-	2^-	4	3^+	4^+	5^+	7	6^-	7^-	8^-
2	1^+	2^+	3^+	5	4^-	5^-	6^-	8	7^+	8^+	9^+

To perform the DWBA calculations, the program DWUCK4 [35] was used. DWUCK4 performs calculations using zero-range, single step DWBA interactions and also includes the functionality to add finite-range corrections. It can be used to calculate σ_{LJ}, A_{yy}^{LJ} and A_{y}^{LJ} values for the ^{192}Os($\vec{d}$,α)^{190}Re reaction as required. To do so, an input file needs to be produced in order to specify the basic input to the program, the form of the initial and final distorted waves and to describe the form factor for the interaction between these two states. To easily produce these input files, a python program named PyDwuck was written which reads in input parameters, performs checks to ensure that the inputs are suitable, formats the numbers into the form used by DWUCK4 before laying these out in a correctly formatted DWUCK4 input file [90]. To perform the DWBA calculations, DWUCK4 requires optical model parameters to be provided to the program through the input file. For the incoming, outgoing and transfer channels, the optical model potential used was the sum of volume and surface Woods-Saxon potentials, described in sections 2.1.1 and 2.2.3. These have the form

$$V(r) = \underbrace{V_R\, f(x_R) + i\, V_I\, f(x_I)}_{\text{volume}} + \underbrace{W_R\, g(x_R) + i\, W_I\, g(x_I)}_{\text{surface}}, \tag{6.7}$$

where

$$f(x_i) = 1/(1 + e^{x_i}), \tag{6.8}$$

$$g(x_i) = \frac{df(x_i)}{dx_i}, \tag{6.9}$$

$$x_i = (r - r_{0i}A^{1/3})/a_i. \tag{6.10}$$

Here V_R and V_I are the real and imaginary volume potentials and W_R and W_I are the real and imaginary surface potentials. The reduced radius of the target or recoil nucleus is given by $R_i = r_{0i}A^{1/3}$ as in section 2.1.1, and a_i gives the diffuseness of the potential. All these parameters, along with other parameters required for the simulation, are taken from global optical model parameter libraries such as RIPL [36]. The optical model parameters used for the initial waves, final waves and the transfer interaction are shown in table 6.3.

Table 6.3: Optical model parameters provided to DWUCK4 in order to calculate observables for the ^{192}Os($\vec{d}$,α)^{190}Re reaction using DWBA calculations. The parameters for the incoming d + ^{192}Os channel and bound d + ^{190}Re state are taken from reference [91] with the parameters for the outgoing α + ^{190}Re channel taken from reference [92].

		d + ^{192}Os	α + ^{190}Re	d + ^{190}Re
Volume	V_R	103.4	185.0	104.0
	r_{0R}	1.15	1.40	1.15
	a_R	0.81	0.52	0.81
	V_I	0.0	25.0	0.0
	r_{0I}	0.0	1.40	0.0
	a_I	0.0	0.52	0.0
Surface	W_R	0.0	0.0	17.8
	r_{0R}	0.0	0.0	1.34
	a_R	0.0	0.0	0.68
	W_I	18.7	0.0	0.0
	r_{0I}	1.34	0.0	0.0
	a_I	0.68	0.0	0.0

Using these parameters, input files for DWUCK4 were produced in order to calculate theoretical values for σ_{LJ}, A_{yy}^{LJ} and A_y^{LJ} for the ^{192}Os($\vec{d}$,α)^{190}Re reaction, each corresponding to a different spin/parity configuration for the recoil ^{190}Re nucleus.

These files used L transfers given in table 6.2 in order to reproduce these configurations. These calculations were compared to the measured data, once values for the spectroscopic factors had been calculated using a minimisation routine.

6.2.3 Differential Cross Sections and Analysing Powers

For each of the observed peaks in the ^{190}Re spectrum, shown in figure 6.2, the differential cross section and analysing power were calculated for each of the four angles at 10°, 15°, 21° and 27°. These values were then compared to theoretical calculations corresponding to different spin/parity configurations for the excited state of the ^{190}Re recoil nucleus. A minimisation routine was first used to find the spectroscopic factor, seen in equations 6.5 and 6.6, for each of these configurations before performing a goodness of fit test to determine which configuration matched the measured data the best.

Firstly, this method was used to attempt verify the spin and parity of the known states in ^{190}Re, given in figure 3.2. An example of this is shown in figure 6.3 for the $E = 119.12\,\text{keV}$, $I^{\pi} = 3^{-}$ state. From this it can be seen that the theoretical and measured differential cross sections match well, though the analysing power agreement is not convincing. It is believed that this is due to the analysing power being more sensitive to the exact optical model parameters used. Although attempts were made to adjust the optical model parameters in order to better fit the measured analysing power data, this was unsuccessful.

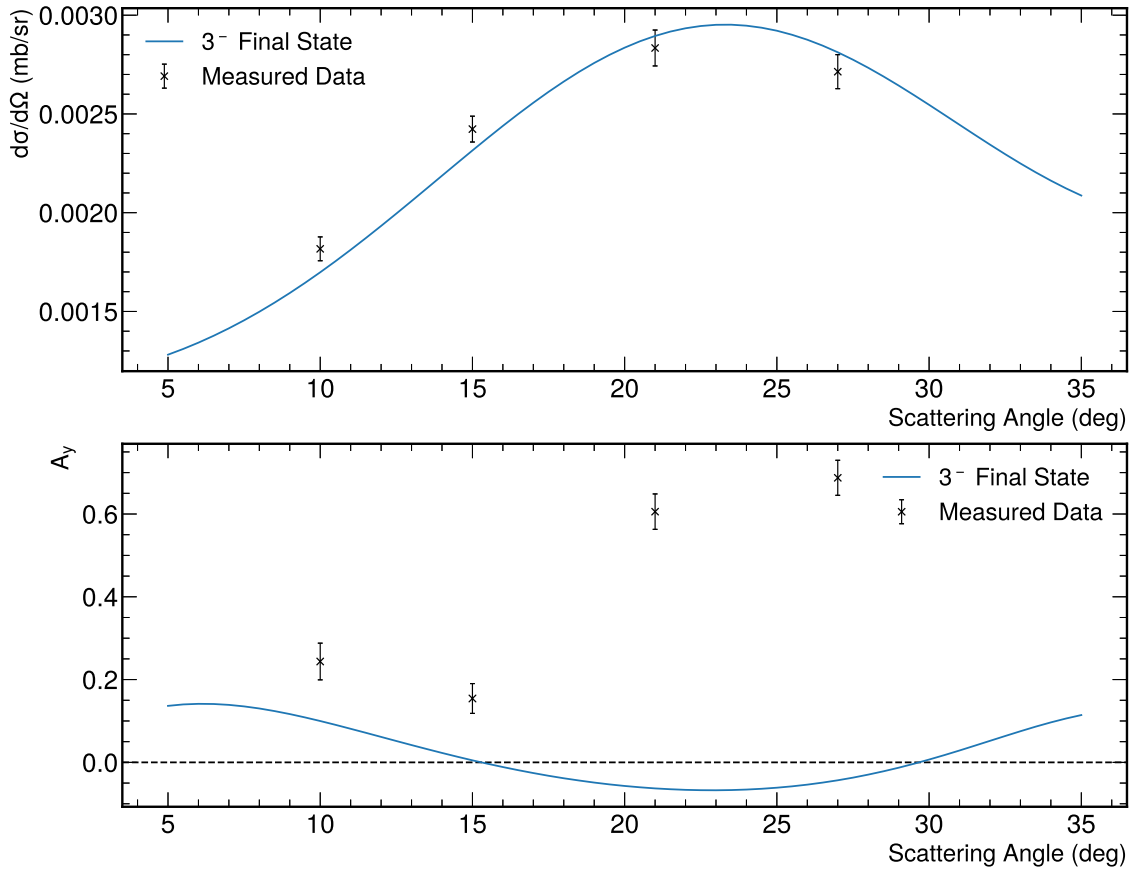


Figure 6.3: Comparisons between measured data for the differential cross section and analysing power for the $E = 119.12\,\text{keV}$ state in ^{190}Re, produced via the $^{192}\text{Os}(\vec{d},\alpha)^{190}\text{Re}$ reaction, and theoretical calculations performed using DWUCK4 corresponding to a $J^{\pi} = 3^{-}$ state in the recoil ^{190}Re nucleus.

The same poor matching between the calculated and measured distributions are observed when attempting to compare calculations for the other known states in ^{190}Re, for both the differential cross sections and the analysing powers. It is thought that this is due to the fact that these all correspond to unnatural parity states, and that there are issues with how the multiple contributing L-transfers are calculated and combined. These issues have not currently been rectified, so the spin/parity configurations of states in ^{190}Re cannot yet be confidently assigned. However, the experimental differential cross sections and analysing powers (calculated using the

method described in section 6.2.1) are shown in figure 6.4 with the intention of aiding any further study on the spin and parity of the excited states in ^{190}Re. Of particular interest are the 206.1 keV and 212.8 keV peaks, both of which could potentially correspond to the ^{190m}Re isomeric state. Another issue is the lack of data. As there is no fitting between the observed and calculated differential cross sections and analysing powers, other than the scaling of the spectroscopic factor, it is common for the two to only match weakly even in the best case scenario. Due to this, having several observed data points over a wide angular range is beneficial. In the case of this study, only having four points over a fairly small angular range makes matching observed data to calculated distributions difficult, even if the distributions are being calculated correctly.

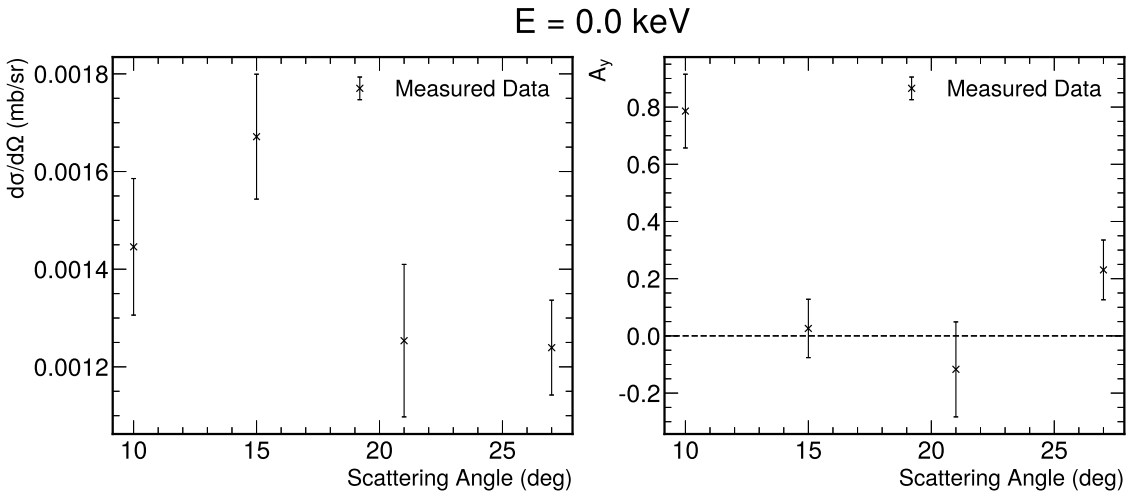


Figure 6.4: Figure continues on next page.

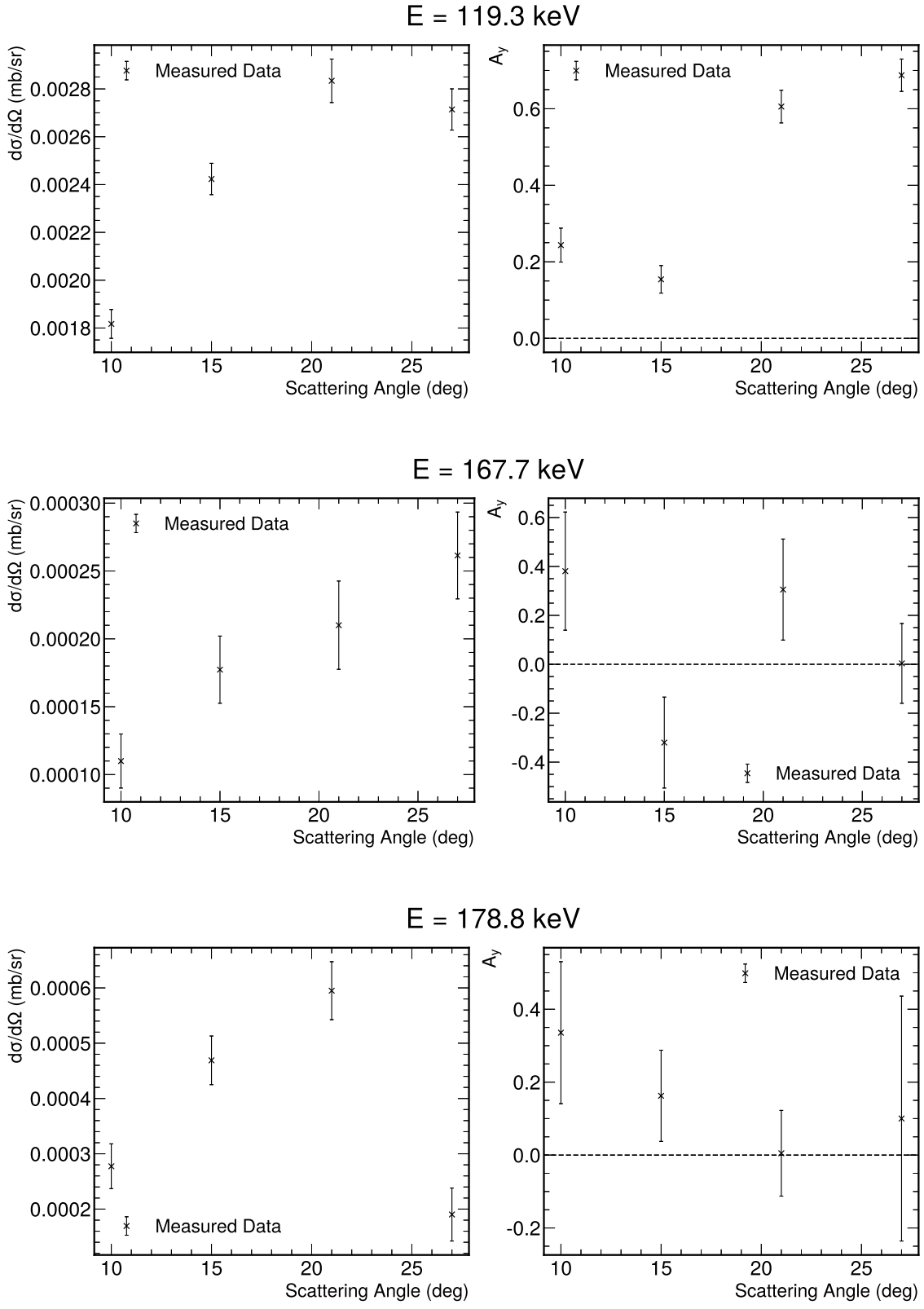


Figure 6.4: Figure continues on next page.

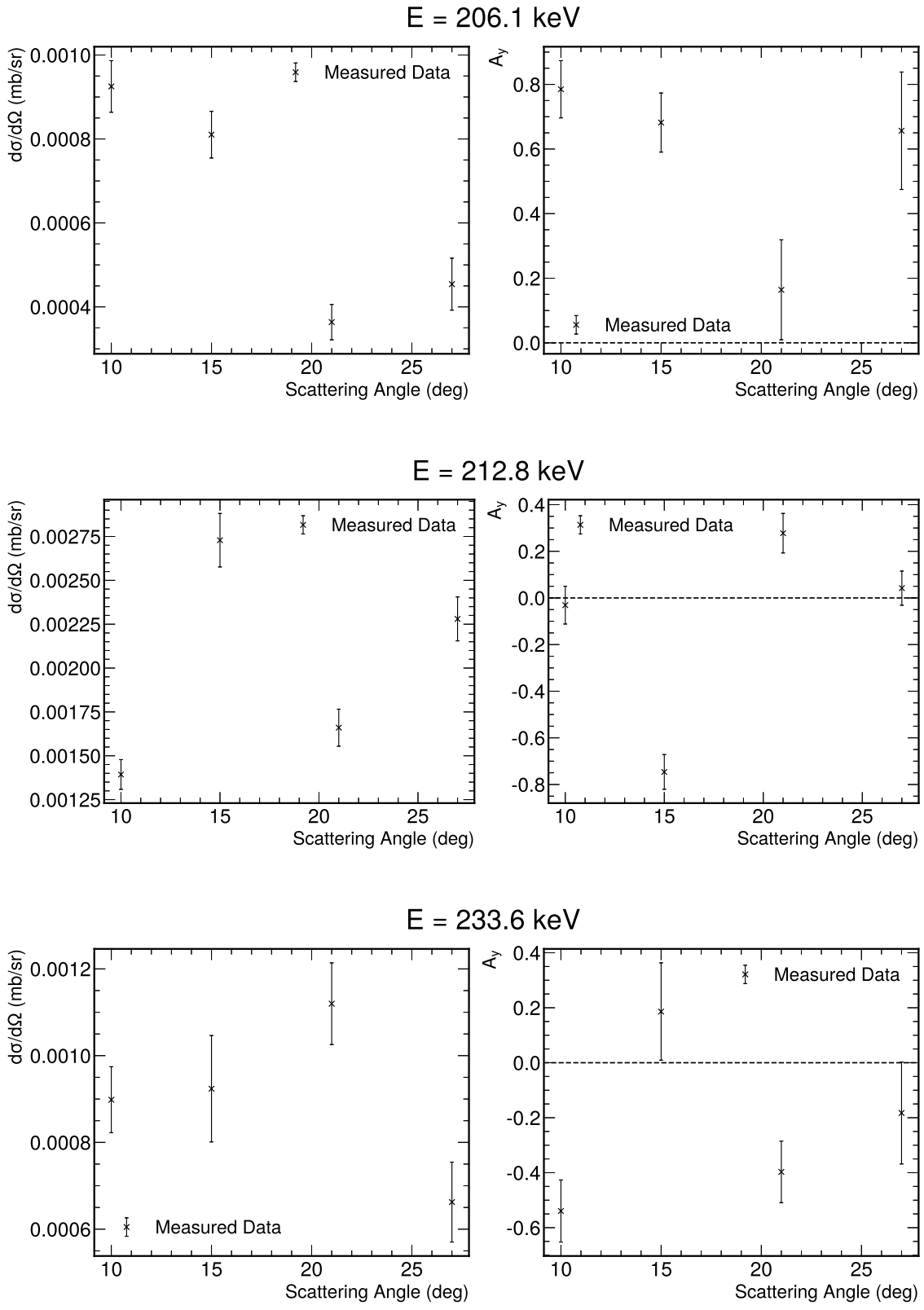


Figure 6.4: Figure continues on next page.

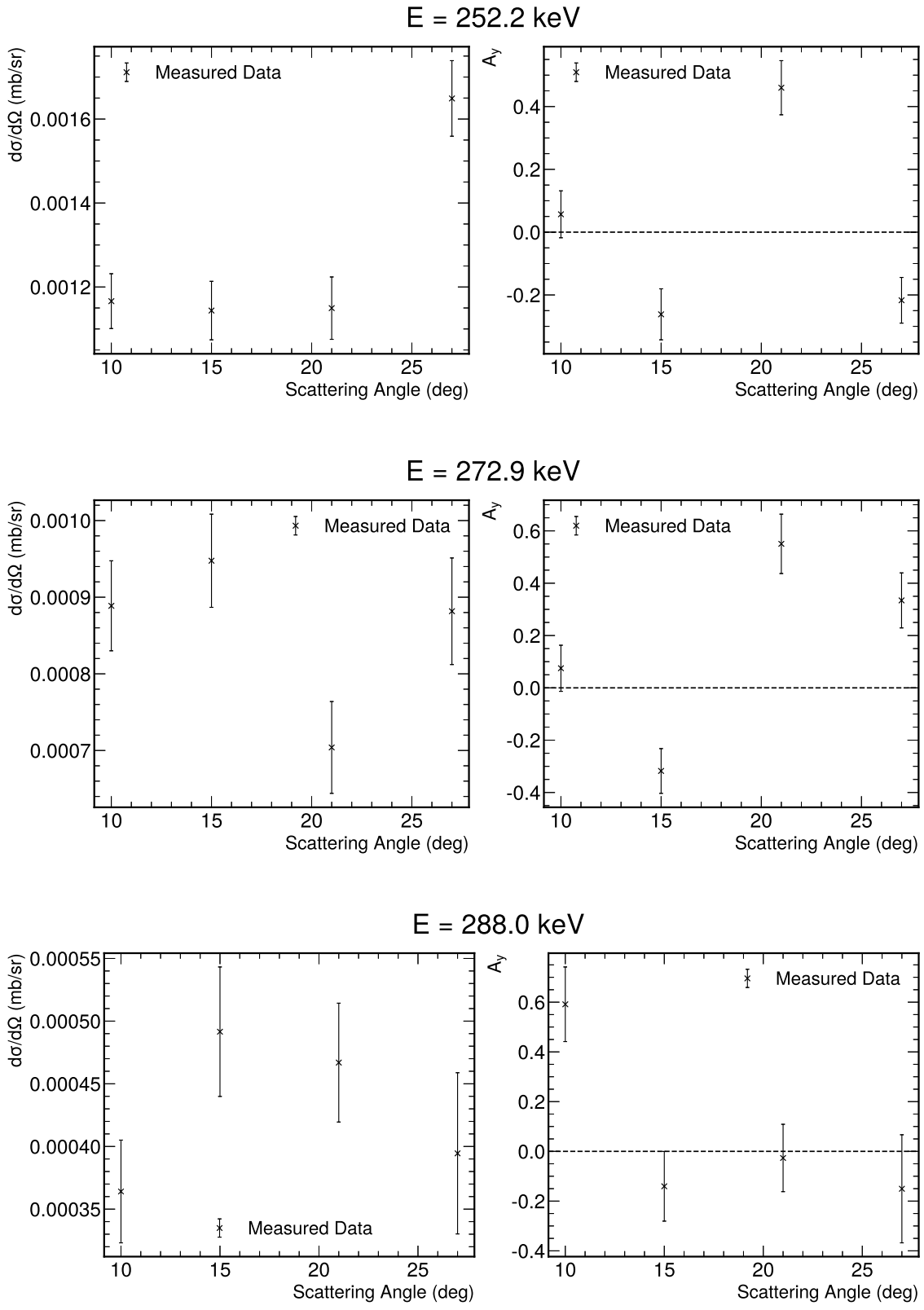


Figure 6.4: Figure continues on next page.

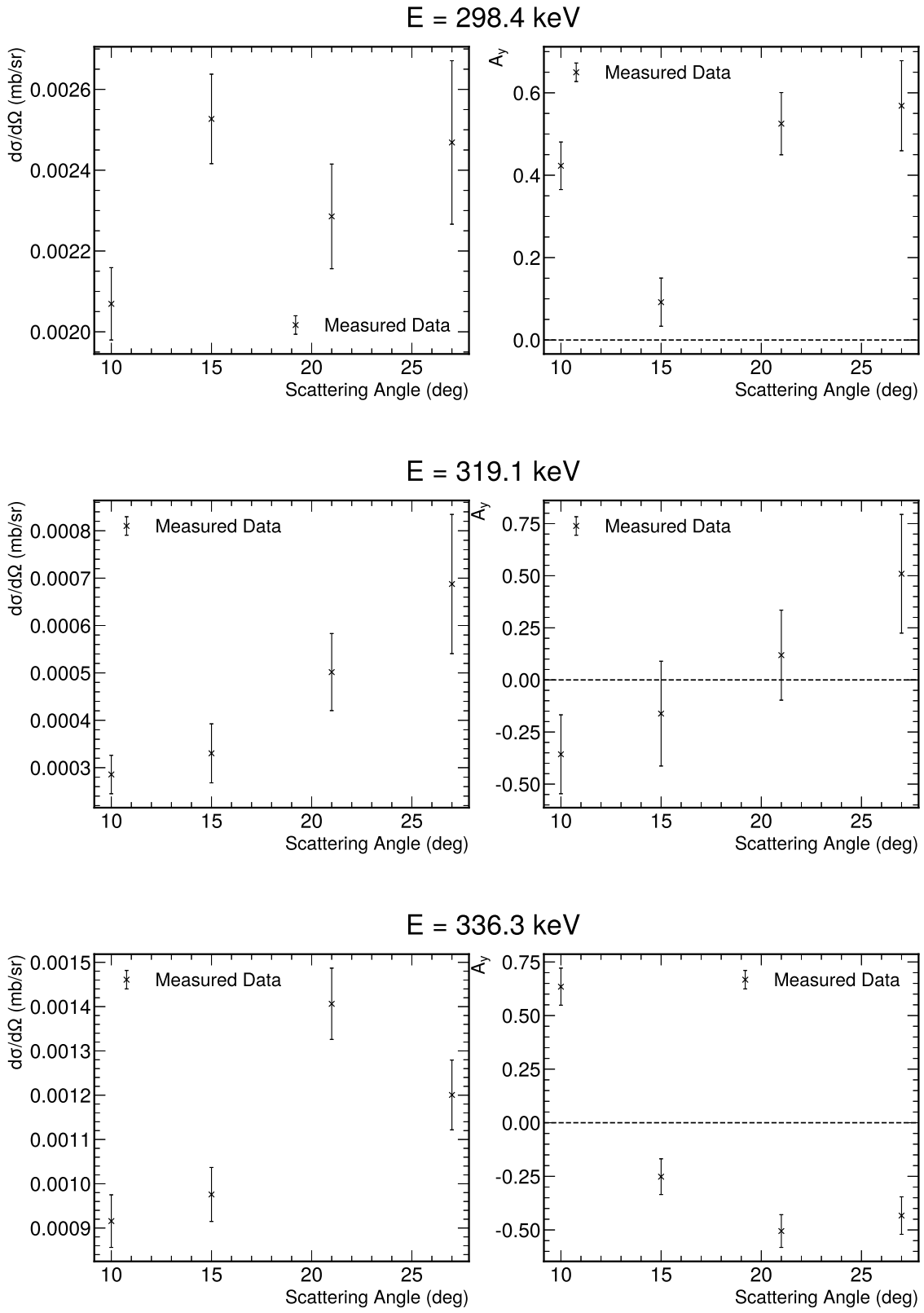


Figure 6.4: Figure continues on next page.

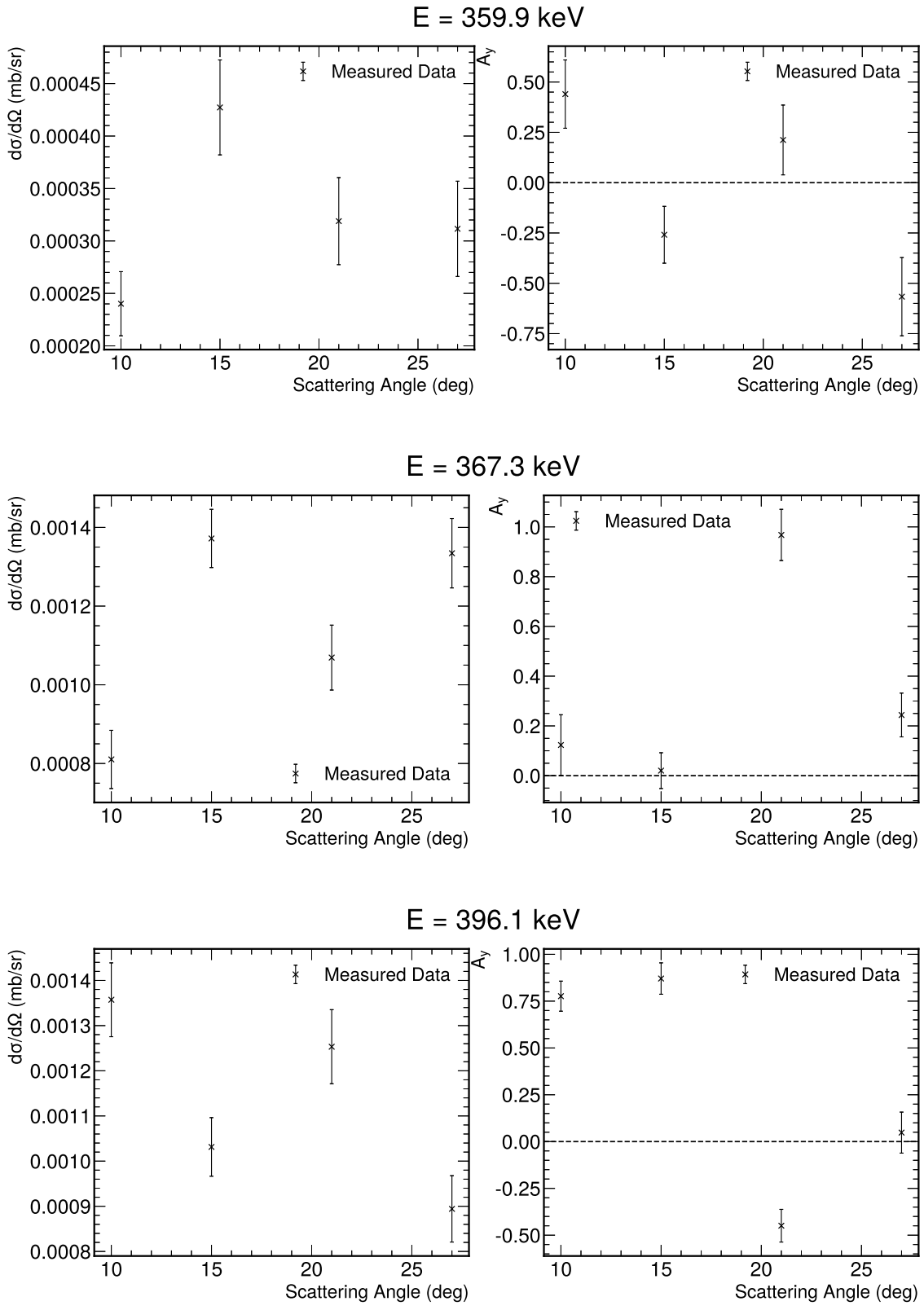


Figure 6.4: Figure continues on next page.

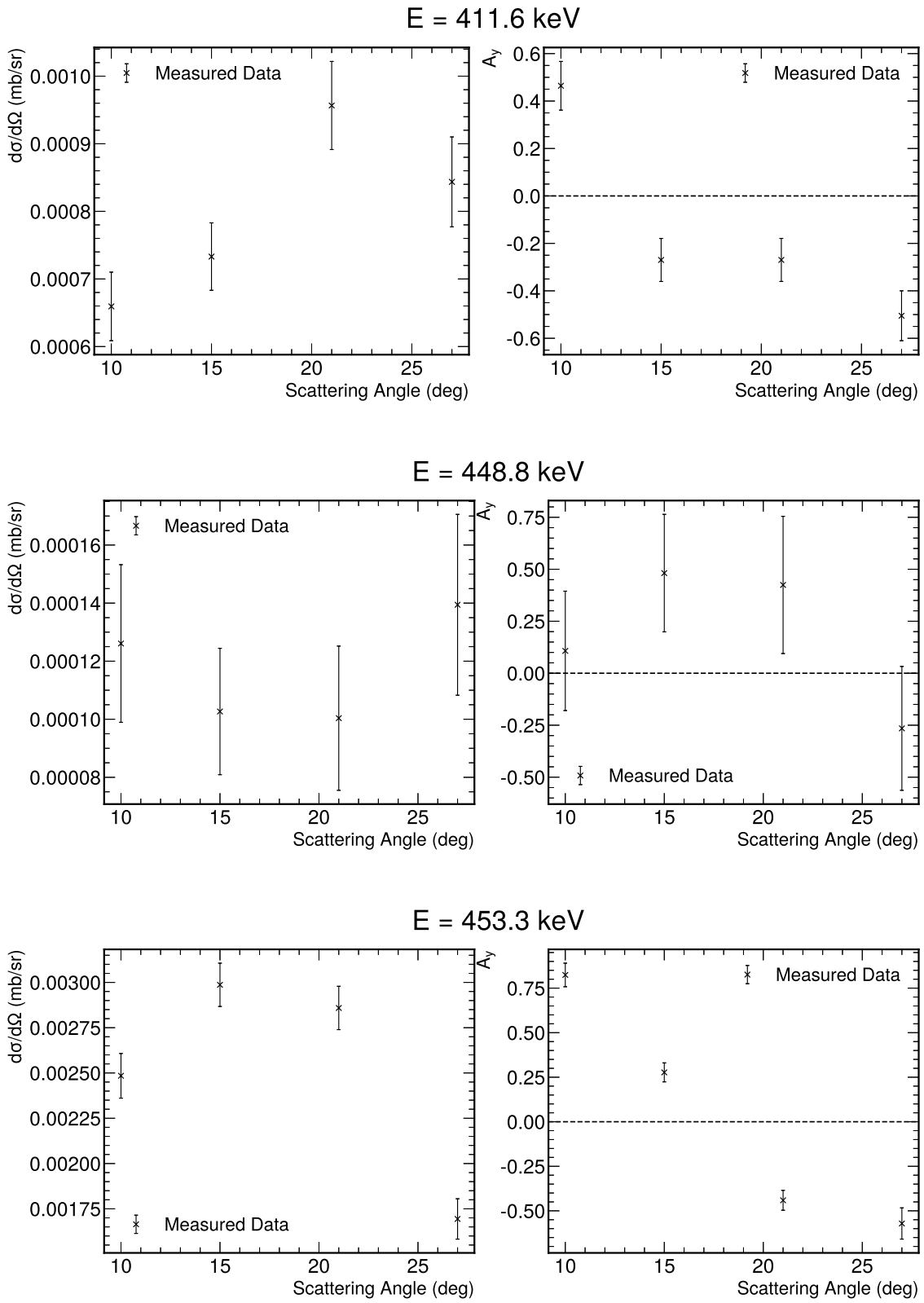


Figure 6.4: Figure continues on next page.

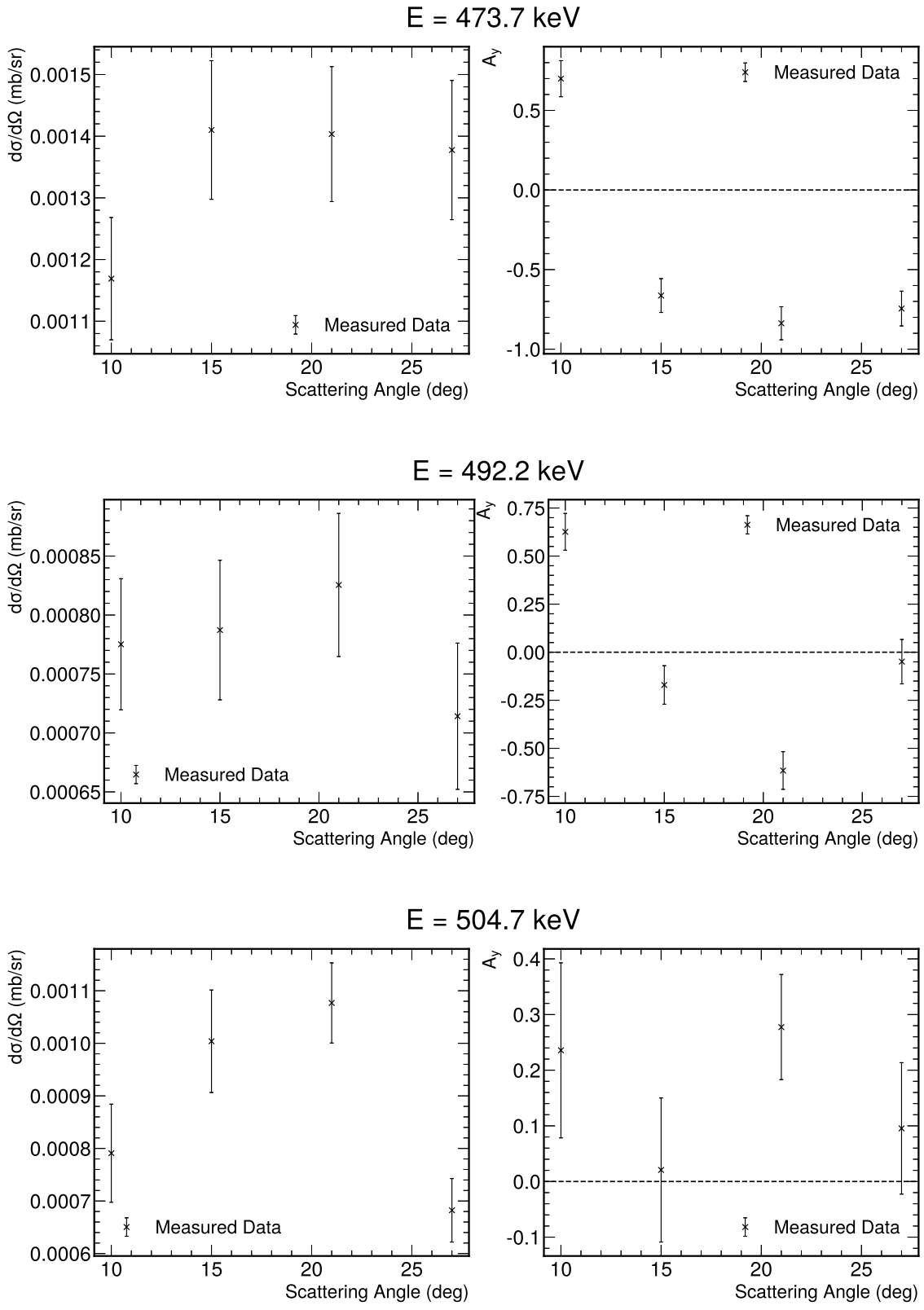


Figure 6.4: Figure continues on next page.

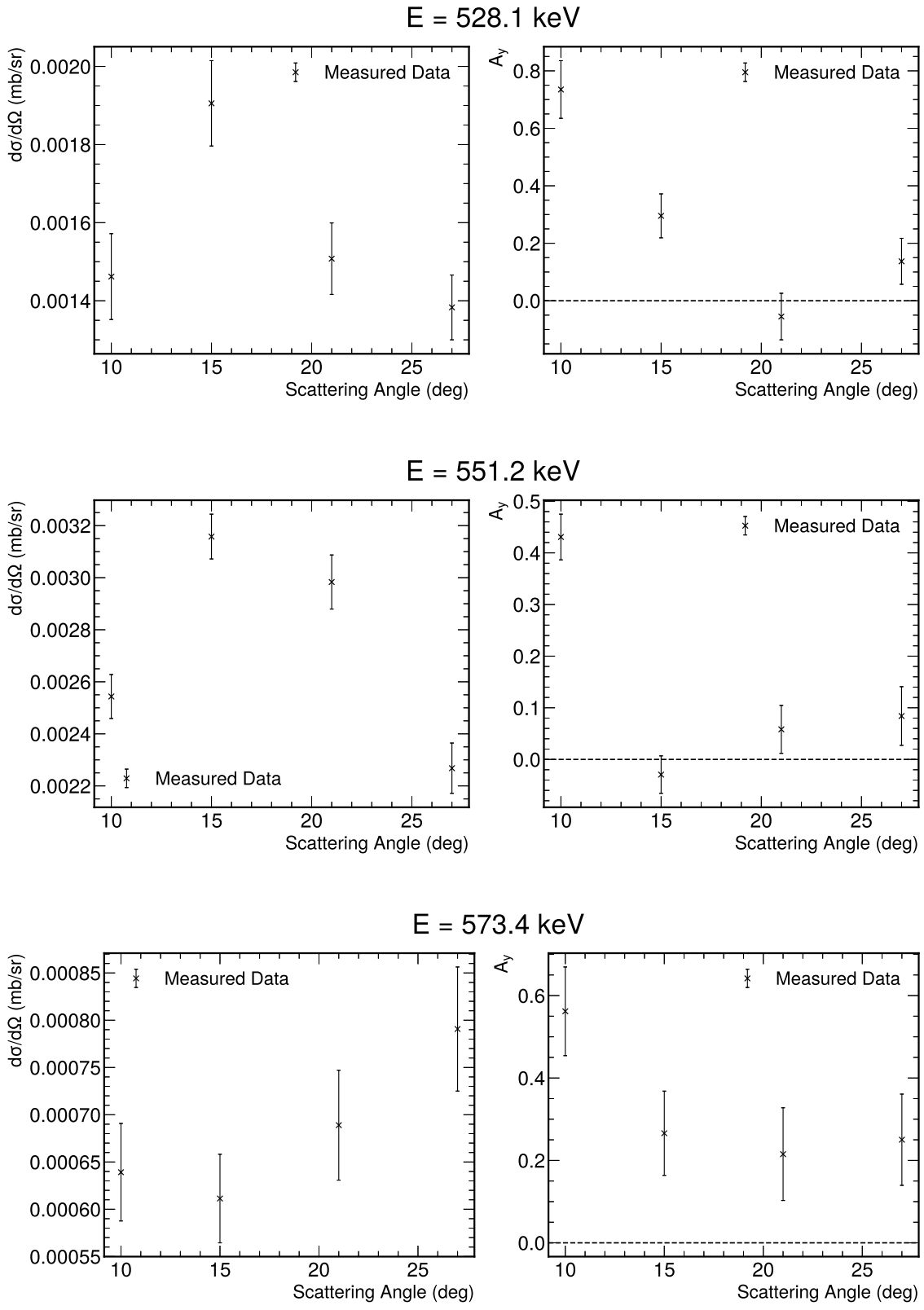


Figure 6.4: Figure continues on next page.

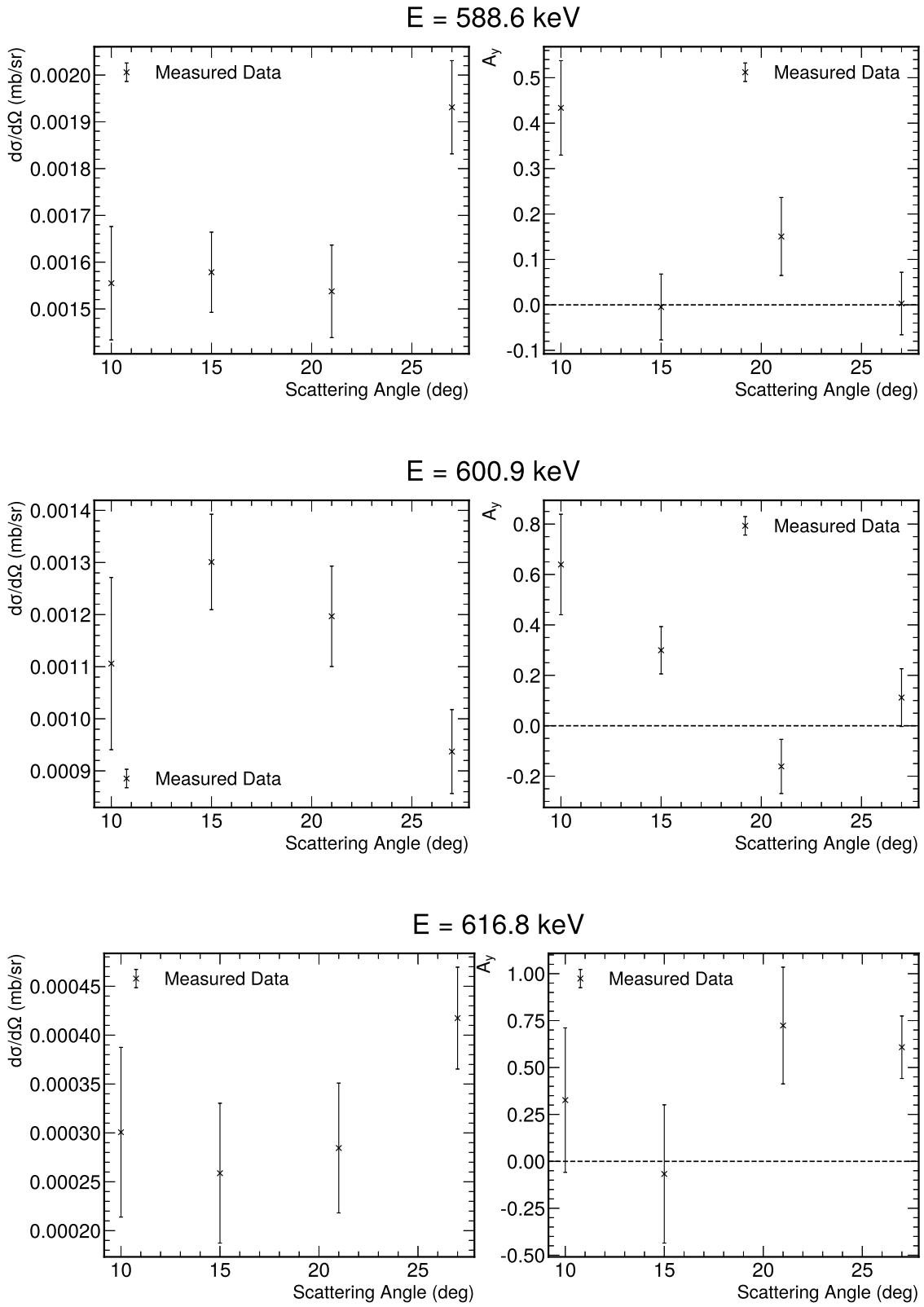


Figure 6.4: Figure continues on next page.

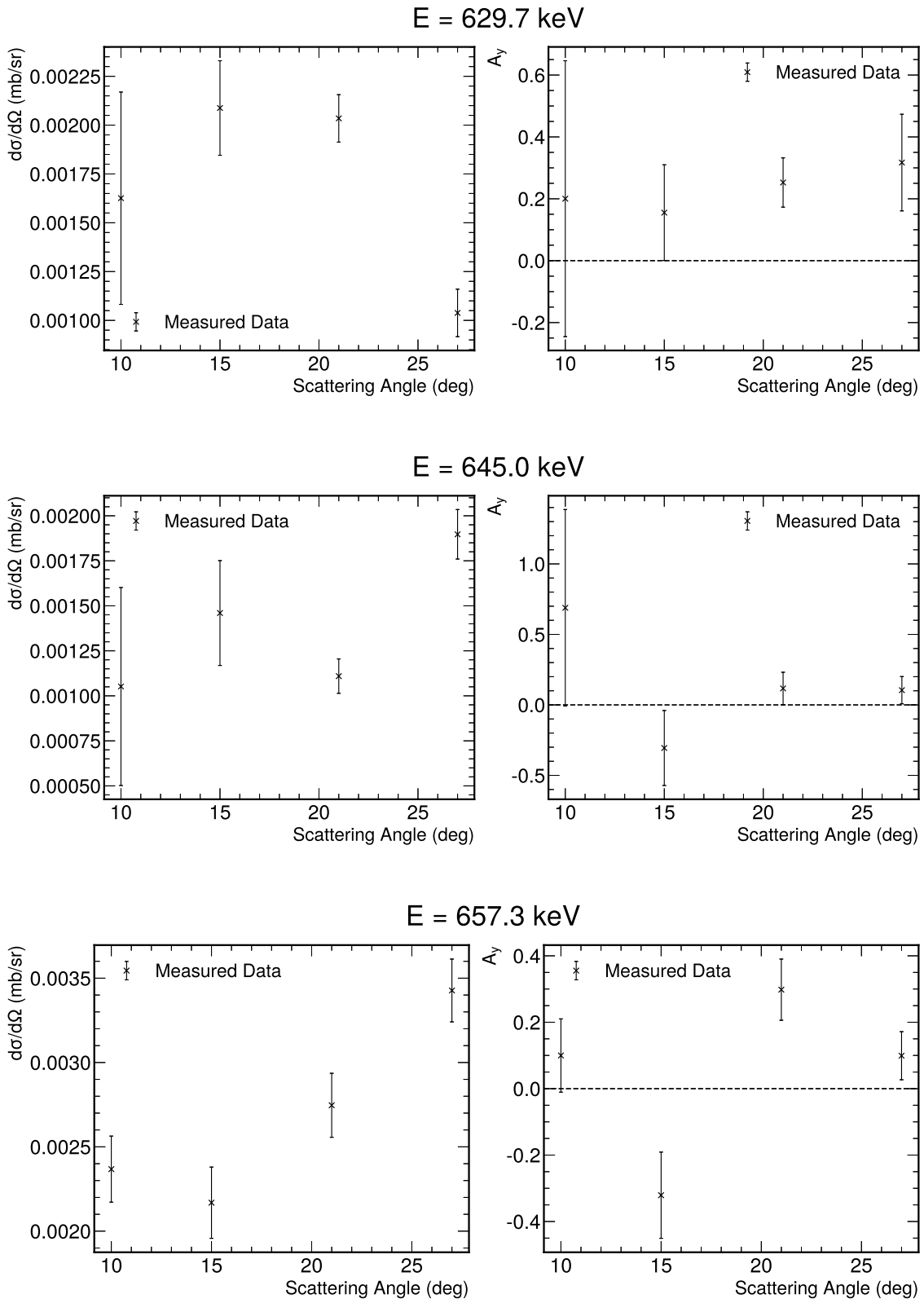


Figure 6.4: Figure continues on next page.

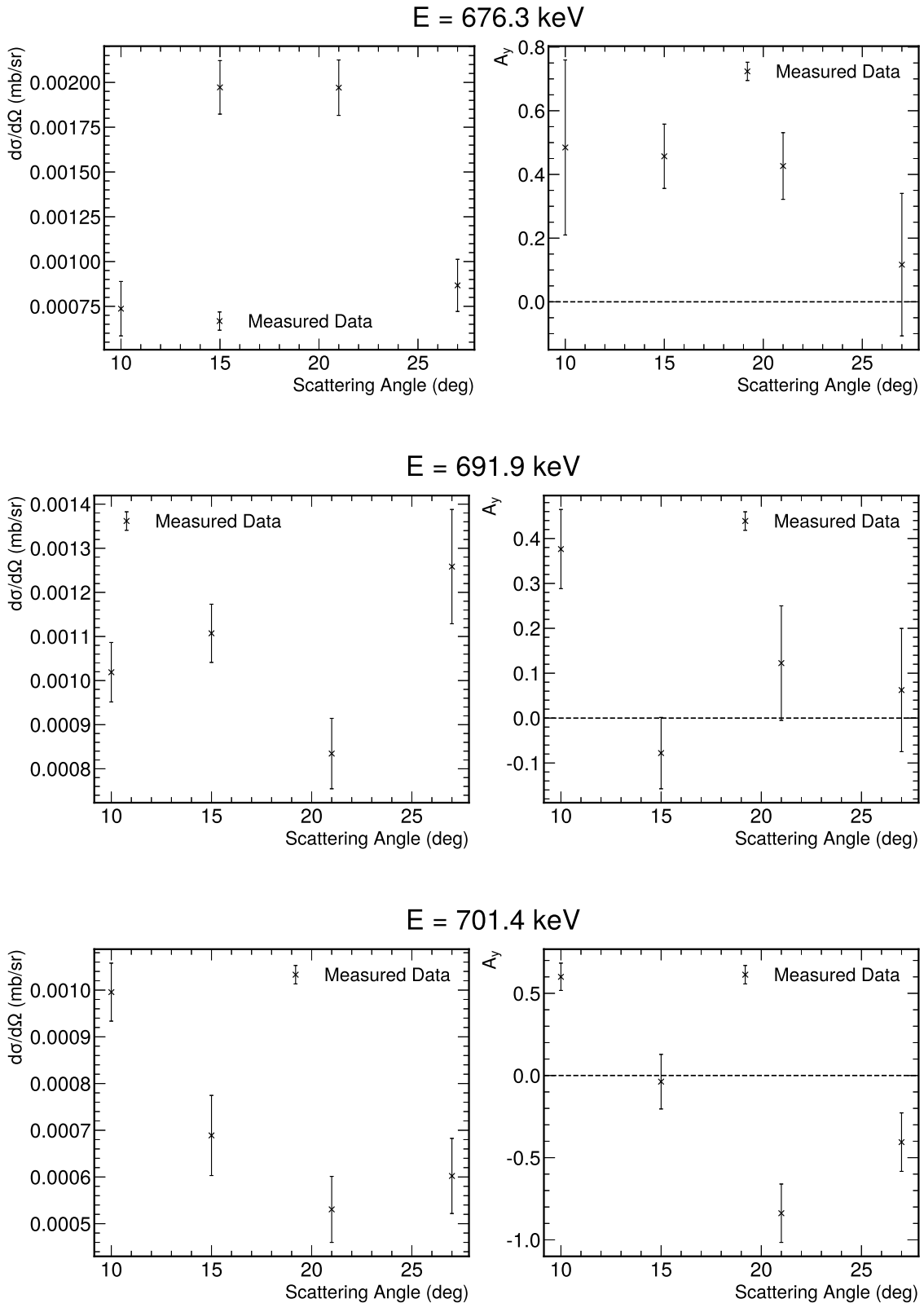


Figure 6.4: Figure continues on next page.

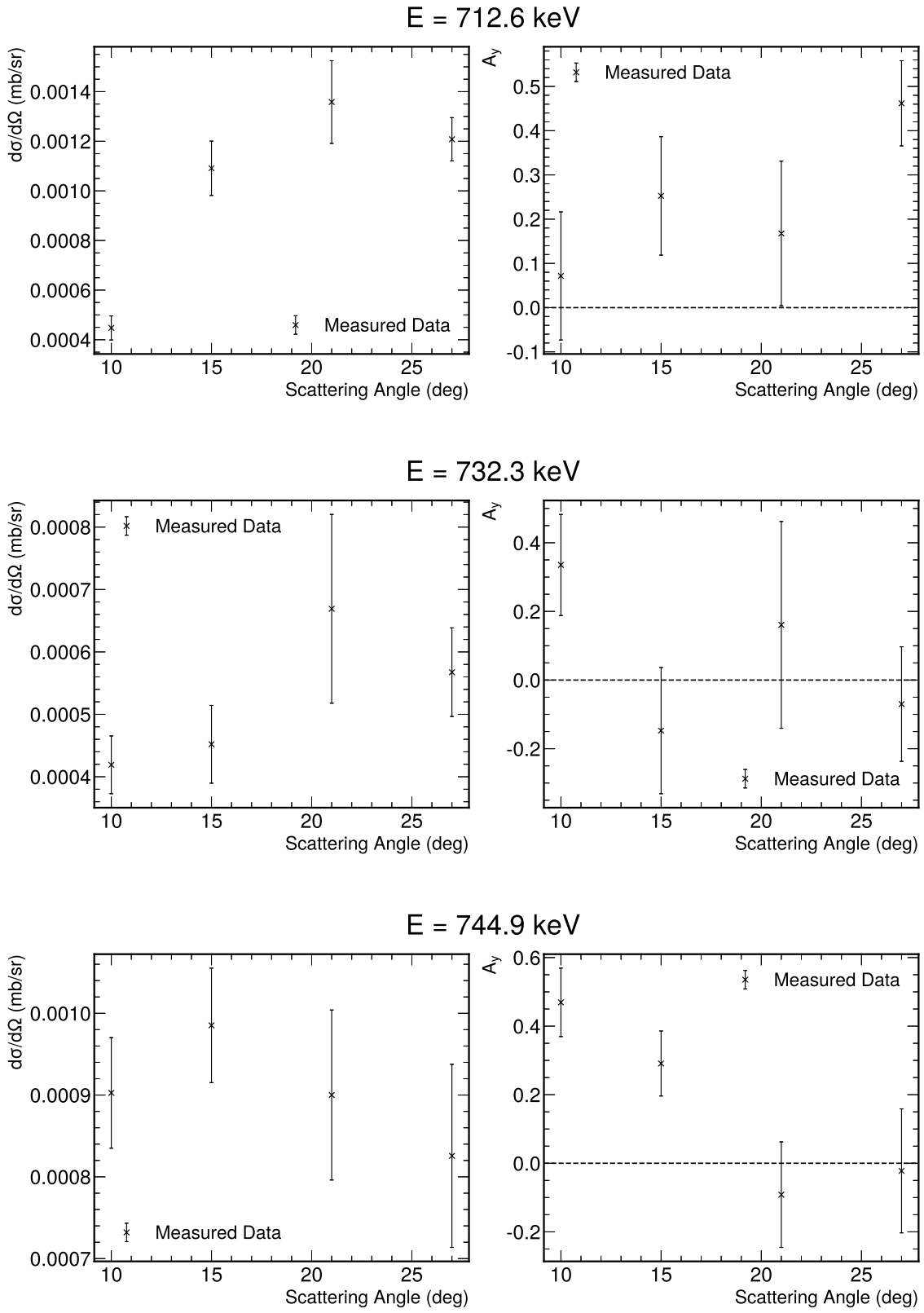


Figure 6.4: Figure continues on next page.

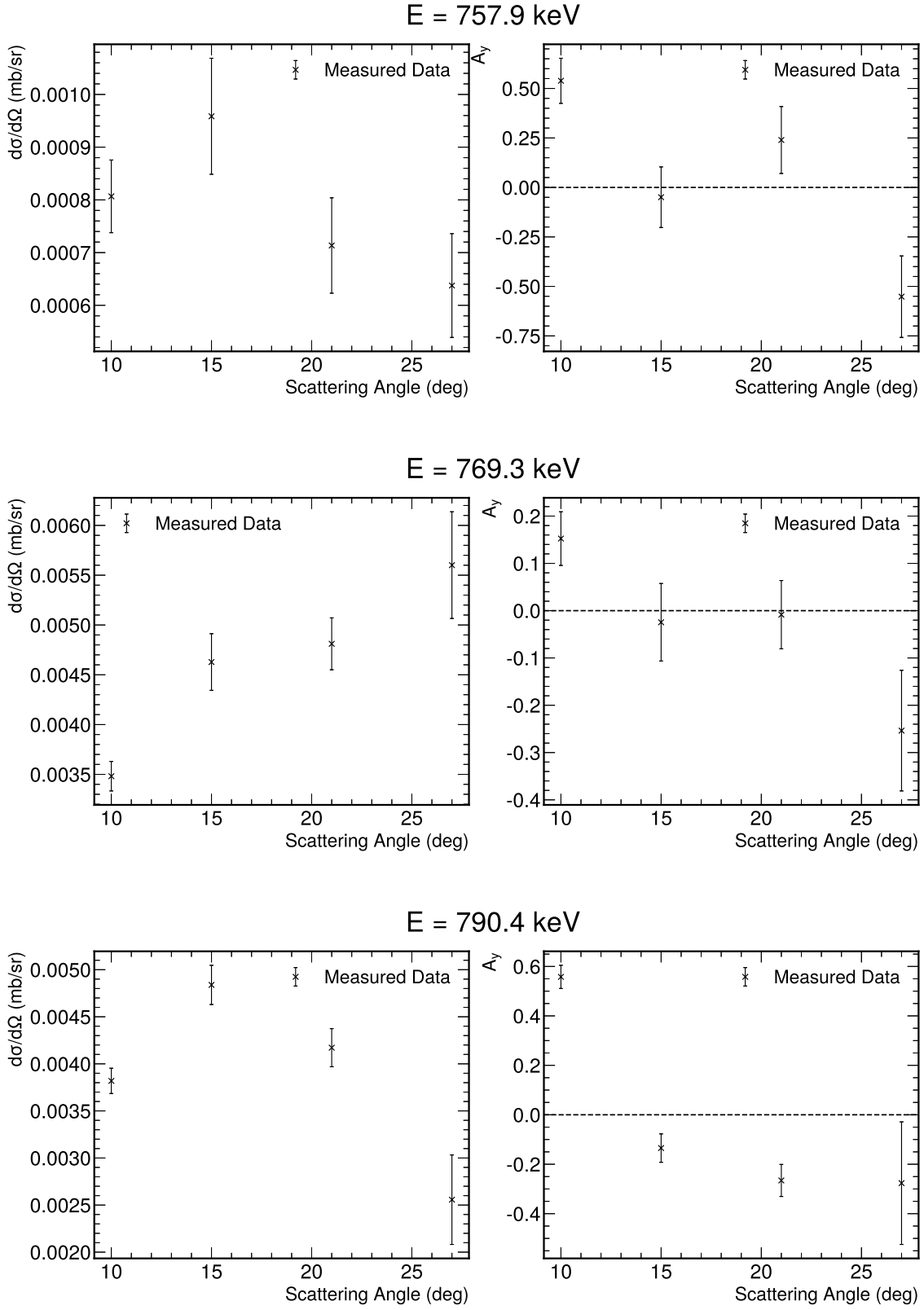


Figure 6.4: Figure continues on next page.

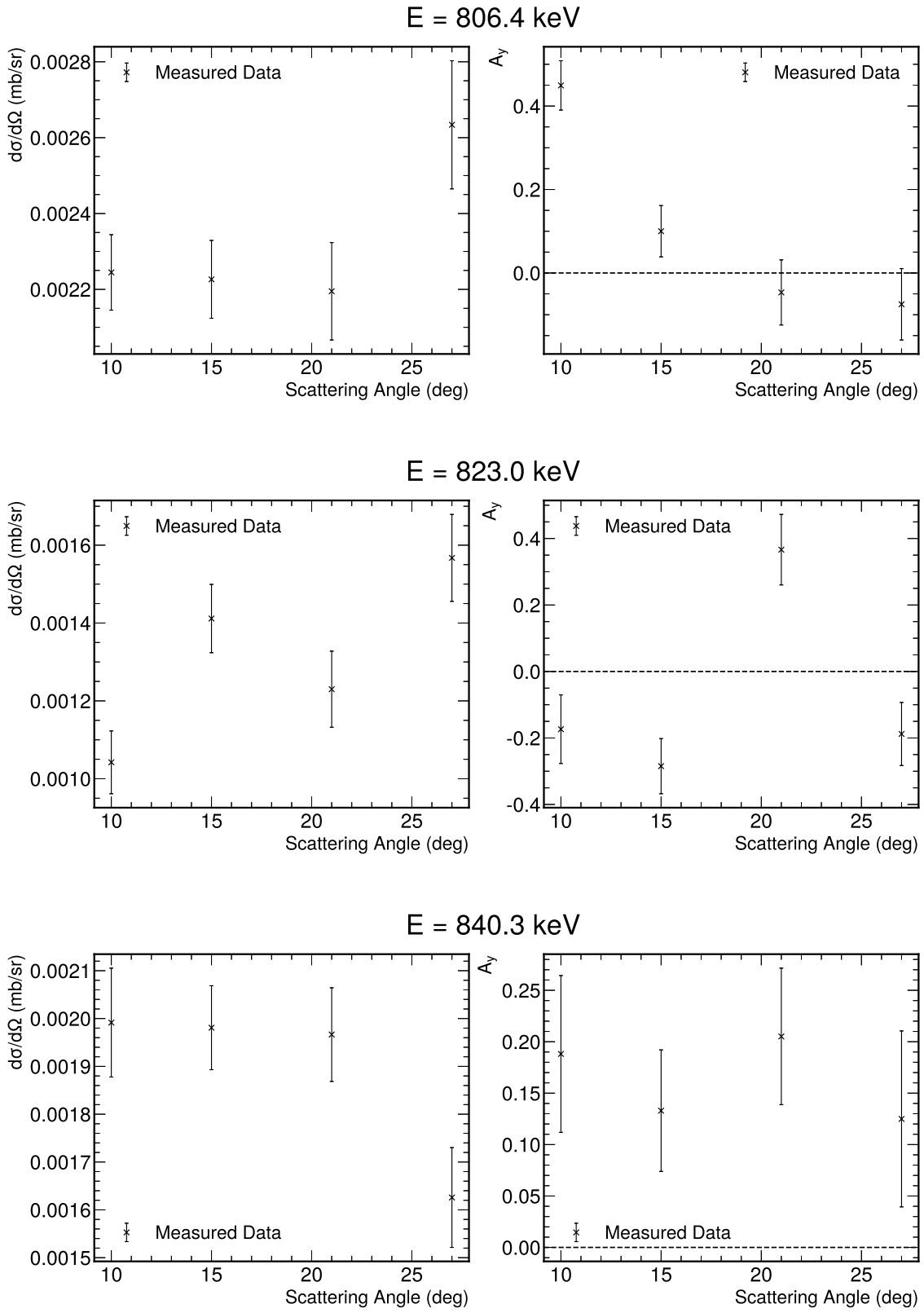


Figure 6.4: Figure continues on next page.

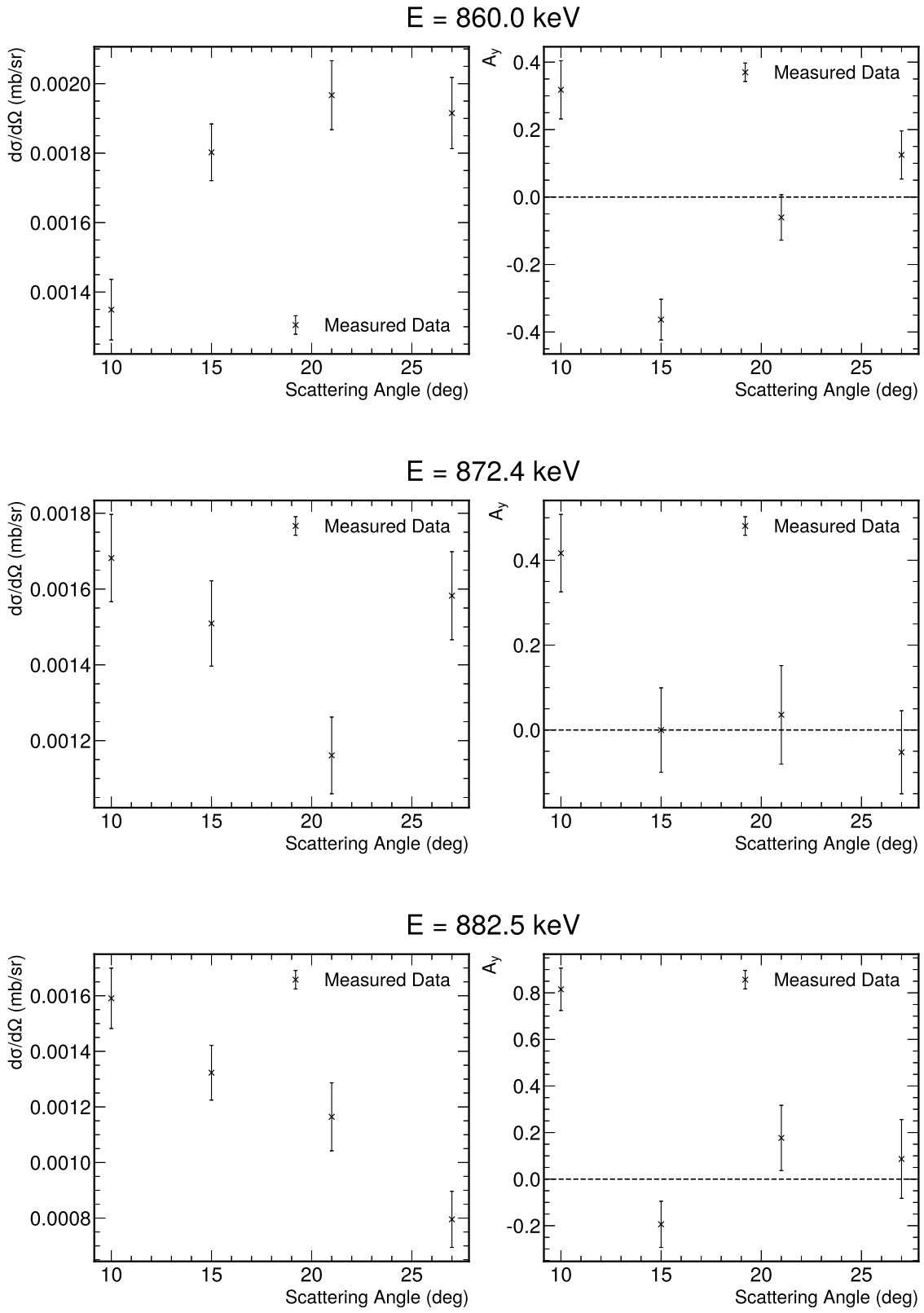


Figure 6.4: Figure continues on next page.

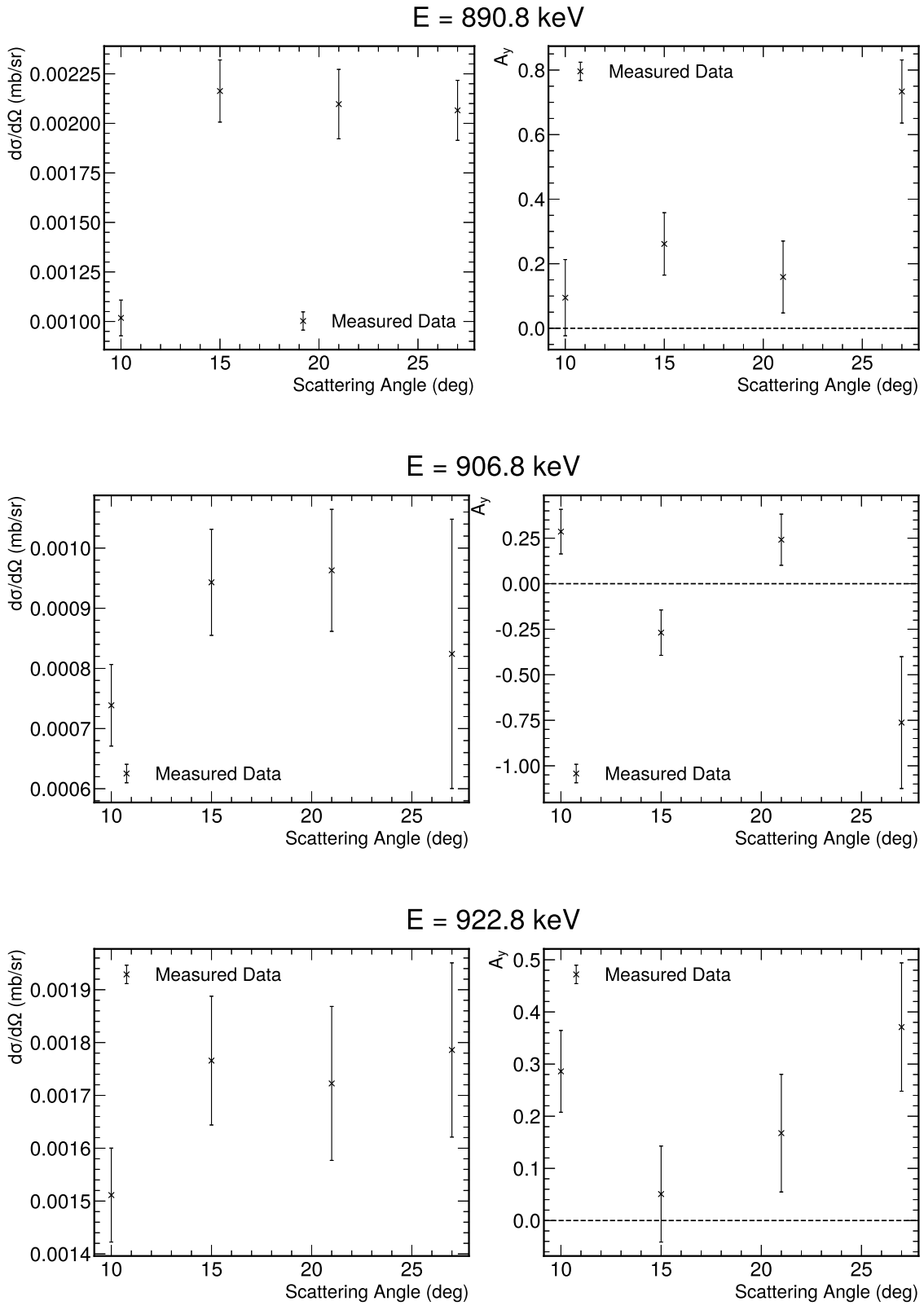


Figure 6.4: Figure continues on next page.

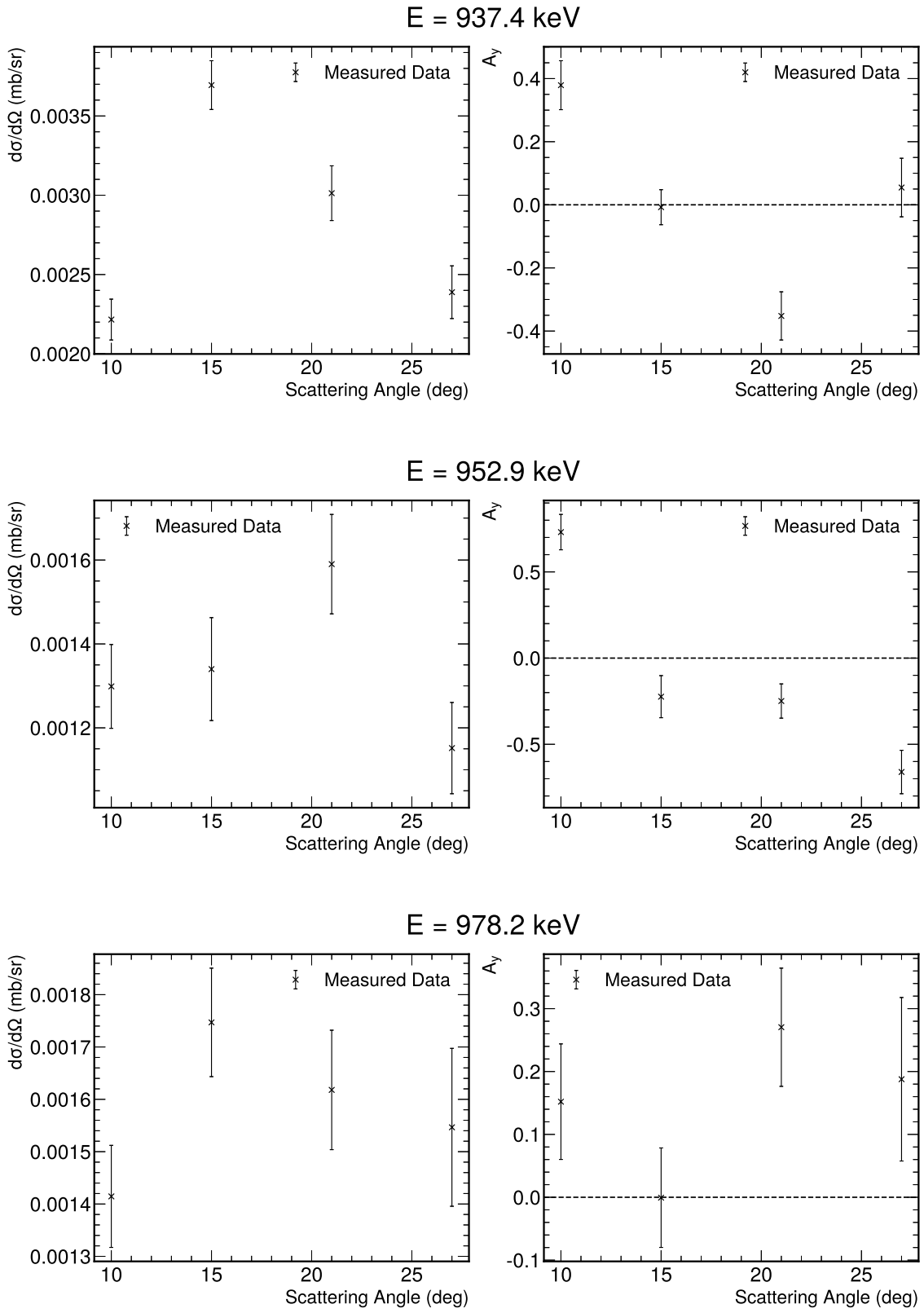


Figure 6.4: Figure continues on next page.

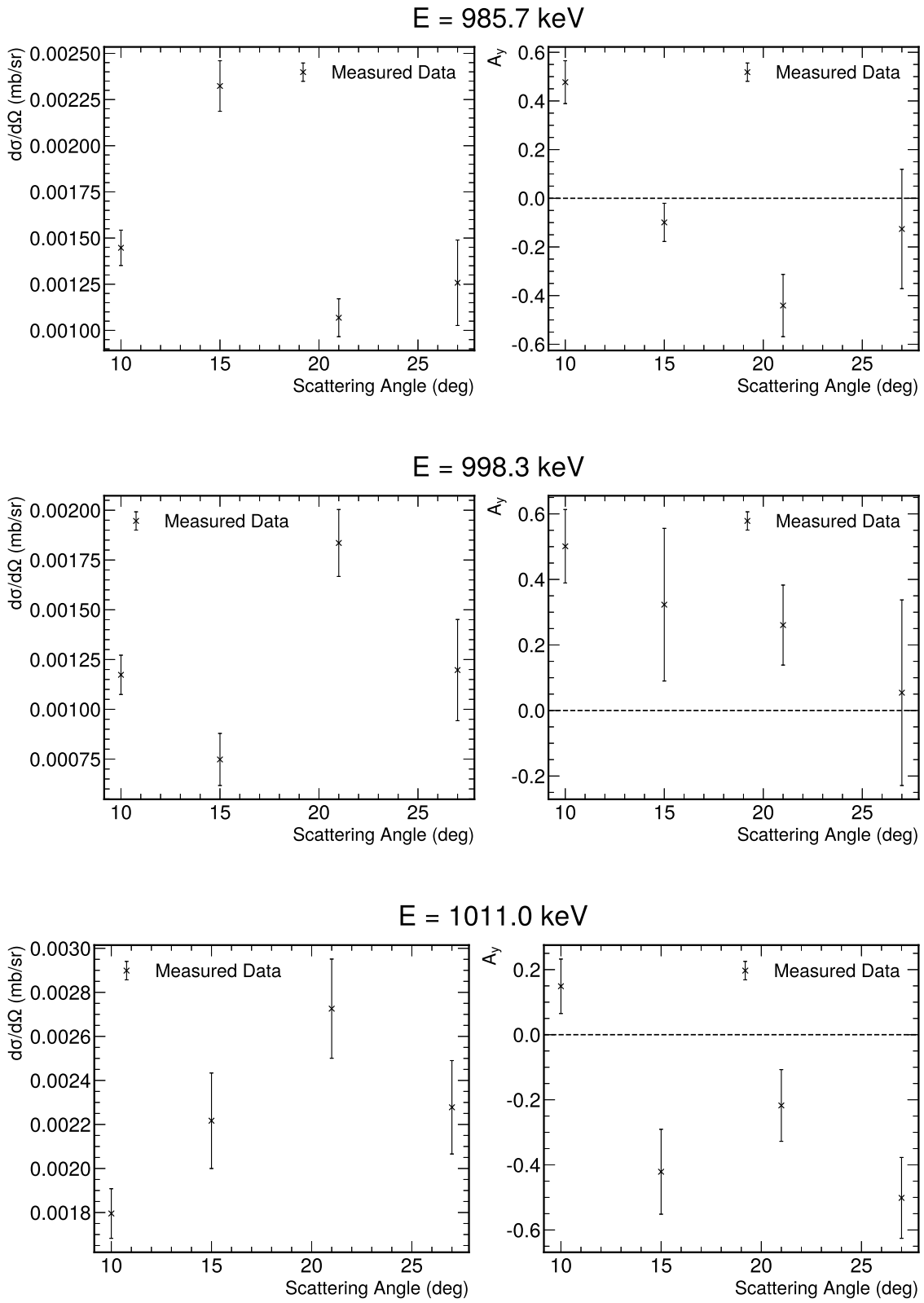


Figure 6.4: Figure continues on next page.

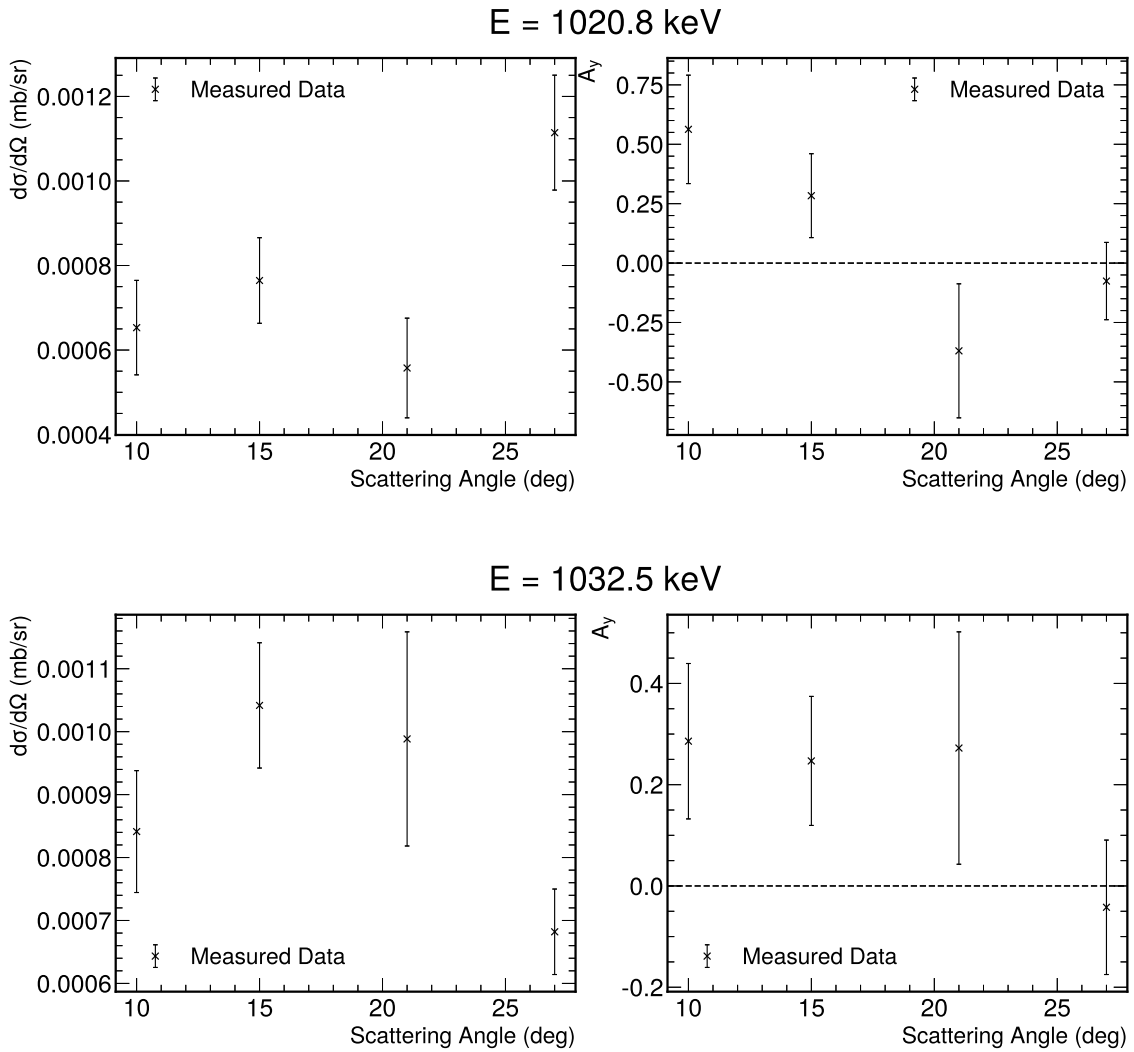


Figure 6.4: Differential cross section and analysing power distributions for all observed peaks in the ^{190}Re spectrum. Each set of plots is presented with the energy of the peak given by the calibration.

6.3 Discussion and Outcomes

In this part of the study, a total of 57 states in the ^{190}Re energy spectrum were observed and fitted. These are the most comprehensive data for ^{190}Re to-date and will aid future spectroscopic studies.

Chapter 7

Positronium Investigations

The majority of the analysis for the project described in previous chapters was conducted during the COVID-19 pandemic, with the experimental work performed in 2010. During the pandemic, experimental nuclear physics facilities were either closed, or time at these facilities was in high demand due to limited operation or backlog from previous closures. Therefore, to gain experience in designing and performing an experiment, a side project was devised involving investigating the properties of positronium using equipment commonly found in nuclear laboratories used for undergraduate teaching. If this experiment was shown to be successful, it would then be implemented as part of the undergraduate nuclear laboratory at the University of Birmingham.

7.1 Theoretical Background

Positronium (Ps) is the bound state of an electron and a positron. As the positron is the antiparticle of the electron, positronium is a type of exotic atom known as an onium. It has a mass of 1.022 MeV, double the electron mass minus $\sim$6.8 eV due to the binding energy of the system [93]. Positronium is metastable but short lived with the two particles annihilating each other, producing differing numbers of gamma rays in the process depending on the overall spin-state of the positronium.

Positronium can form in different states due to the relative orientations of the positron and electron spins. There exists a singlet state, $^1S_0$, where the spins of the electron and positron are antiparallel ($S=0,\ M_S=0$). This is known as para-positronium (p-Ps). There is also a triplet state, $^3S_1$, where the spins are parallel ($S=1,\ M_S=-1,0,1$) which is known as ortho-positronium (o-Ps).

Para and ortho-positronium exhibit different decay properties. Para-positronium decays into an even number of photons in order to conserve angular momentum, with two back-to-back 511 keV photons the most probable decay. The branching ratio rapidly decreases for decays to a greater number of photons [94]. Accounting for all decay modes the theoretical lifetime of para-positronium in a vacuum is found to be 125.1624 ± 0.0006 ps [95], a result that agrees with experimentally observed values [96].

The leading decay for ortho-positronium is into three gamma rays with other decay modes having negligible branching ratios [94]. The mean lifetime of ortho-positronium has been theoretically calculated to be 142.0463 ± 0.0004 ns [95], significantly longer than that of para-positronium. This result is also seen to agree with experimental observations [97]. Although ortho-positronium is produced $\sim$30% of the time a positron is produced (compared to $\sim$10% for para-positronium), three-photon events are only observed 0.5% of the time [98]. This is because the majority of ortho-positronium decays are via 'pick-off' where an external electron is encountered, with which the positron in ortho-positronium will annihilate [99].

7.2 Positrons in Aluminium

7.2.1 Method

In the first part of this experiment, the lifetime of positrons in aluminium was measured. To achieve this, a ^{22}Na source with an activity of 22.5 kBq was used as ^{22}Na β^+ decays into ^{22}Ne. This source was produced by bombarding natural aluminium with protons to induce the $^{27}\mathrm{Al}(p, \alpha pn)^{22}\mathrm{Na}$ reaction, before placing the source (the vast majority of which is still aluminium) within an aluminium casing. Sodium-22 most commonly decays into the 1274.5 keV excited state in ^{22}Ne, which then subsequently undergoes spontaneous emission, releasing a gamma ray and de-exciting to the ground state. The lifetime of the excited state is 3.60 ± 0.05 ps [100]. Information about this decay is shown in figure 7.1.

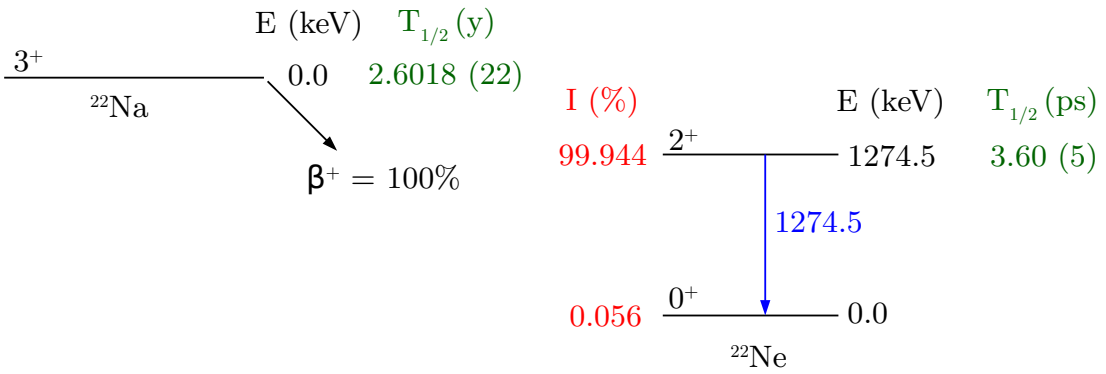


Figure 7.1: Decay information for ^{22}Na. Data taken from reference [100] (page 88).

As the emission of a 1274.5 keV photon accompanies the emission of a positron $> 99\%$ of the time and, as the half-life of the 1274.5 keV state is negligible compared to the

half-life of positronium, detection of this gamma ray was used as an indication that a positron had been produced. As both decays of para-positronium and annihilation result in the production of two 511 keV gamma rays, detection of one of these gamma rays was used as an indication that the positron had decayed.

Due to the short lifetime of positrons, the equipment used in this experiment needed a fast timing response. It is known that $CeBr_3$ detectors exhibit excellent timing resolution compared to similar gamma-ray detectors [101]. Therefore, this experiment made use of detectors containing cylindrical crystals with a length and diameter of 25.4 x 25.4 mm $CeBr_3$ crystals coupled to Hamamatsu R13089-100 photomultiplier tubes, also known for their fast timing response [102].

In this experiment, the aim was to measure the time between the detection of the 1274.5 keV gamma ray (the start signal) and the detection of the 511 keV gamma ray (the stop signal) detailed above. This was achieved by using two of the aforementioned $CeBr_3$ detectors to measure gamma rays given off by the ^{22}Na source. The signals from these $CeBr_3$ detectors were then processed by two Constant-Fraction Discriminators (CFDs). Upon receiving a signal, CFDs generate a pulse once the rising edge of the signal passes some fraction of its overall amplitude. This is beneficial compared to simply generating a pulse when the rising edge passes a set point as it ensures the logic pulse for a given signal with varying amplitude is generated at a consistent reference time, important for precise timing measurements. Also, compared to other electronics that can be used for the same purpose (such as

Timing Single-Channel Analysers) CFDs exhibit less time-jitter [103] and amplitude walk [104], the two main sources of uncertainty in the timing of the signal.

A lower threshold for the amplitude of signals that the CFDs will process can also be set. The threshold of one CFD was set to just below 1274.5 keV, ensuring that this CFD output signals corresponding to the detection of a 1274.5 keV gamma ray, but not 511 keV gamma rays. This CFD and corresponding detector were designated to measure the start signals for the timing process. The other CFD had its threshold set to just below 511 keV and was, along with its corresponding detector, designated to measure the stop signals. Although this CFD still processed signals corresponding to 1274.5 keV gamma rays, this is unavoidable when using CFDs in such a simple set-up as there is no upper signal threshold. This was not observed to be an issue, however, and simply meant that the main background observed using this set-up was from random coincidences between two 1274.5 keV gamma rays.

As the threshold on the CFDs is based on signal amplitude, a preliminary electronic set-up was required to set these thresholds to the correct corresponding gamma-ray energies. This was done by splitting the signal produced by the $CeBr_3$ detectors, taken from the anode output. In this experiment a negative bias of $-900\,\mathrm{V}$ was applied to the detector, although below the rated maximum bias for the detector, minimal non-linear effects in the energy response of the detectors were observed at this bias. By applying a negative bias to the cathode, the anode is effectively at ground. As a result, there is no capacitor at the anode as there would be if a

positive bias. Therefore, the signal from the anode was expected to show better timing response than the signal taken from the dynode.

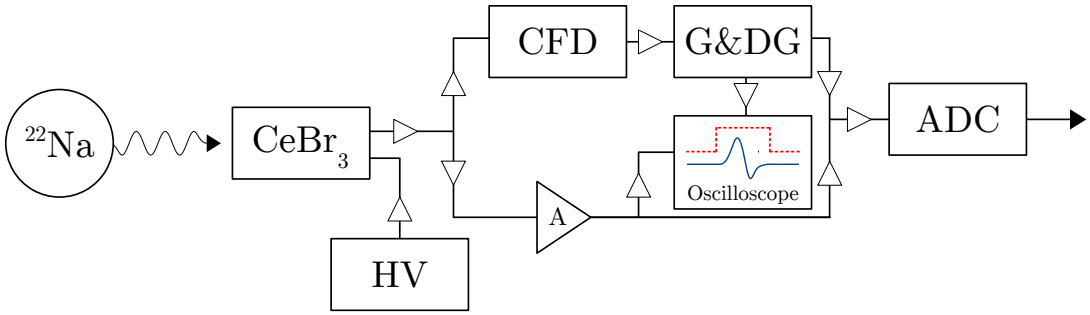


Figure 7.2: The electronic set-up used in this experiment to set the thresholds on the constant-fraction discriminators. In this set-up Scionix $CeBr_3$ detectors, Ortec 572 amplifiers, Ortec 584 CFDs and Ortec 416A G&DGs were used. Here, HV represents a high-voltage power supply. Preampliers were not used in this set-up.

One of the split signals from the anode was fed into the CFD, the signal from which was subsequently fed into a Gate & Delay Generator (G&DG) which takes the logic pulse produced by the CFD and converts it into an elongated 'gate', similar to a top hat function in shape. The other signal was fed through an amplifier. Both the signal from the amplifier and the G&DG were then input into an oscilloscope. The delay on the G&DG was then varied to ensure that signals from both paths were matched in time, verified using the oscilloscope. Once this had been done, the amplified signal was fed into an Analogue-to-Digital Converter (ADC) in order to produce an energy spectrum. The signal from the G&DG was then fed into the 'Gate' input of the ADC. This ensured that the amplified signal was only processed when the ADC received a gate pulse and signal at the same time. As the CFD

fed into the G&DG, raising the CFD threshold limited the incoming gamma-ray energies for which gates were produced. By raising the threshold on the CFDs and viewing what effect this had on the energy spectrum, the CFD threshold was set to a certain energy, as desired. A diagram of this set-up is shown in figure 7.2.

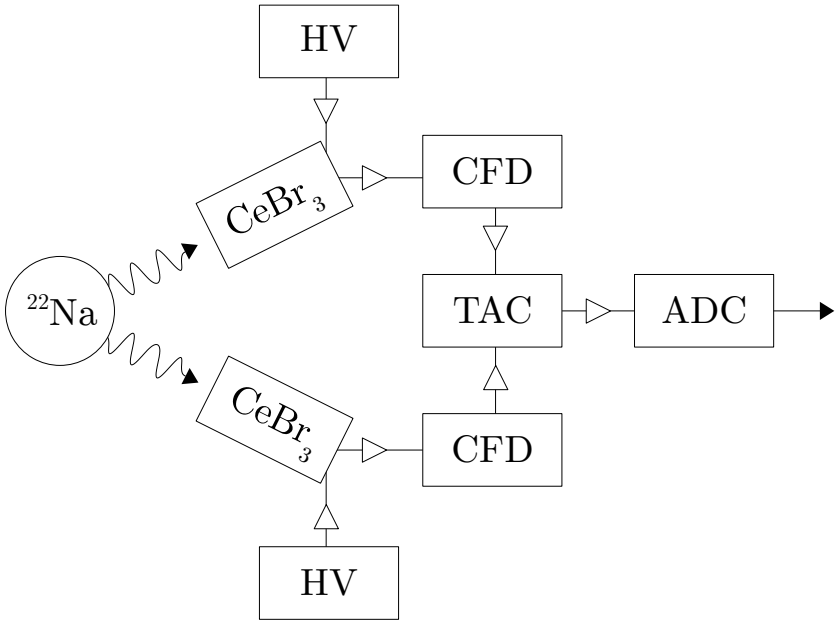


Figure 7.3: The electronic set-up used in this experiment. In this set-up Scionix $CeBr_3$ detectors, Ortec 584 CFDs and a single-width Ortec 566 TAC unit were used. Here, HV represents a high-voltage power supply. Preamplifiers were not used in this set-up.

Once the CFD thresholds had correctly been set, the logic pulses from both were fed into a Time-to-Amplitude Converter (TAC) to measure the time that passed between receiving a logic pulse from the 'start' CFD and the 'stop' CFD. The TAC then produced a signal, the amplitude of which was proportional to this time difference. A longer wire ($\sim$1 m) connecting the 'stop' CFD to the TAC was used to introduce a nominal time delay ($\sim$10 ns) in order to ensure the resulting timing spectrum was

not centred around zero as this would lead to the loss of some information due to situations where the stop signal arrives before the start signal, which was possible due to the timing resolution of the set-up. The TAC output was then fed into an ADC in order to produce a time spectrum. This set-up is shown in figure 7.3.

7.2.2 Analysis and Results

The aforementioned set-up was left to run for a period of ≈ 3 days. The resulting spectrum is shown in figure 7.4. The spectrum was fitted as a convolution between an exponential decay and a Gaussian on top of a linear background, given by the following equation [105]

$$f(x) = \frac{a\lambda}{2} \exp\left(\frac{\lambda}{2}\left(2\mu + \lambda\sigma^2 - 2x\right)\right) \operatorname{erfc}\left(\frac{(\mu + \lambda\sigma^2 - x)}{\sqrt{2}\sigma}\right) + mx + c \quad , \tag{7.1}$$

where a, μ and σ are the height, mean and standard deviation of the Gaussian distribution, λ is the decay constant for the exponential component and m and c are the background gradient and intercept respectively. Note, μ is not the mean of the overall convoluted distribution, which is given by $\mu + 1/\lambda$. Here, $\operatorname{erfc}(x)$ is the complementary error function, defined as

$$\operatorname{erfc}(x) = 1 - \operatorname{erf}(x), \tag{7.2}$$

where $\operatorname{erf}(x)$ is the standard error function, defined in equation 5.18. This function is used as the exponential decay is the expected form of the timing signal for the positronium lifetime and the Gaussian, centred around the effective 'zero time',

comes from the timing resolution of the set-up. This resolution was measured here to be $\approx 160\,\text{ps}$.

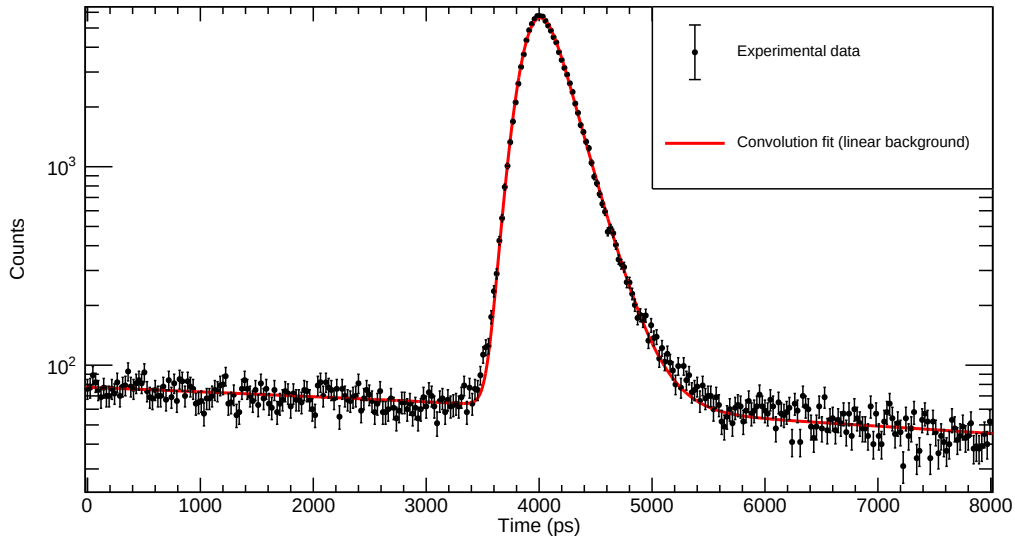


Figure 7.4: Timing spectrum for the lifetime of positrons within aluminium. The fit, denoted by the red dashed line, is a convolution of a Gaussian with an exponential decay on top of a linear background.

From the fit a lifetime for positrons in aluminium was found to be 203 ± 1 ps. Note that this error does not account for systematic uncertainties, the dominant source of which is the time calibration (typically around 5%). This is within errors of previous studies into the lifetime of positrons in aluminium which report a lifetime of 211 ± 10 ps [106].

7.3 Ortho-positronium Measurement

7.3.1 Method

In the second part of this experiment, the aim was to measure the lifetime of ortho-positronium. As mentioned in section 7.1, the vast majority of the time (when pick-off does not occur) ortho-positronium decays into three gamma rays. Due to this, the energy of these gamma rays is no longer fixed at 511 keV as with para-positronium and annihilation, but can be a spectrum of energies in the range $0 < E \leq 511$ keV. Also, the lifetime of ortho-positronium is considerably longer than that of positronium in aluminium at ~ 140 ns. This is an issue as the increased time between measurement of the 'start' and the 'stop' signals will increase the likelihood of stopping due to random coincidences, increasing background. It also gives more time for pick-off to occur, reducing the likelihood of the desired decay occurring and potentially increasing background via the measurement of Compton scattered 511 keV electrons. In order to accurately measure the lifetime of ortho-positronium, both of the effects needed to be accounted for.

To reduce the chances of measuring background events, the CFD measuring the stop signal in figure 7.3 was replaced with a timing single-channel analyser (TSCA) - in this case an Ortec 551 model. This was done as, although TSCAs introduce greater uncertainty into the timing signal, this is insignificant in this case due to the longer lifetime of the ortho-positronium and TSCAs allow both an upper and a lower threshold to be set on the incoming signal amplitude. Therefore, an upper

threshold was set below 511 keV for the 'stop' detector to ensure that gamma rays from decays of para-positronium and the annihilation of positrons are not detected, significantly reducing background. These thresholds were set using the same method described in section 7.2.1, but with a TSCA replacing the CFD.

To reduce the chance of pick-off occurring, the source was contained within a glass vial placed in a container of fumed silica. This was done as using a dense medium with lots of available electrons, such as aluminium, leads to a large probability of pick-off occurring. However, not only is it known that positron implantation into silica nanopowders (such as fumed silica) leads to an abundant production of positronium [107], but it also reduces the rate at which pick-off occurs due to its porous nature [108]. As previously discussed, the source itself was contained within in a small ball of aluminium due to how it was produced which will still result in an increased probability of pick-off occurring.

7.3.2 Analysis and Results

As with the previous experiment, the aforementioned set-up was left to run for a period of ~ 3 days. The resulting spectrum is shown in figure 7.5. The spectrum is fitted using equation 7.1.

From the fit, the lifetime of ortho-positronium was found to be 12.3 ± 0.1 ns. Although this is over an order of magnitude less than the lifetime of positronium in a vacuum, this is expected due to pick-off in both the aluminium the source is embedded in and

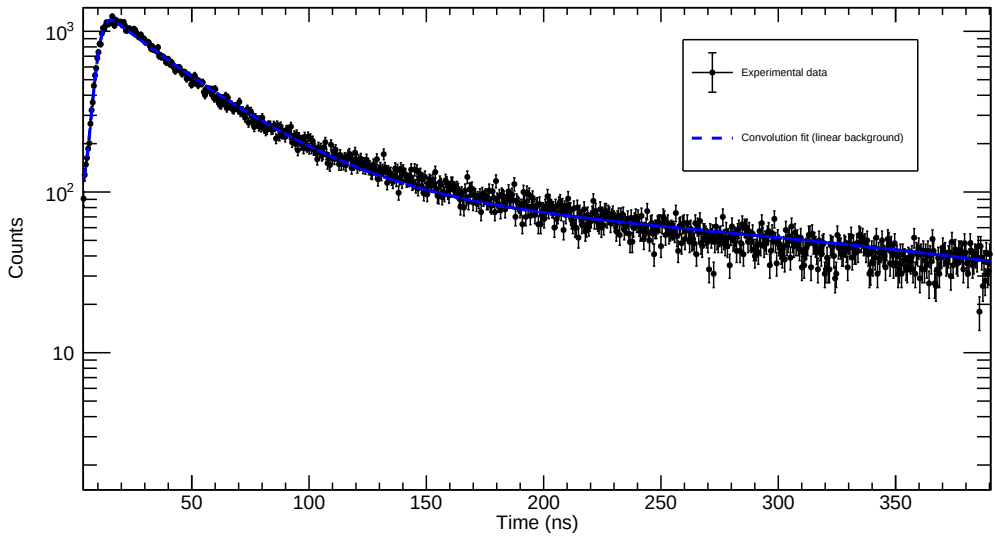


Figure 7.5: Timing spectrum for the lifetime of ortho-positronium within fumed silica. The fit, denoted by the blue dashed line, is a convolution of a Gaussian with an exponential decay on top of a linear background.

also in the air within the fumed silica and the vial used to store the source. In solid materials the lifetime of ortho-positronium is typically reduced to a few nanoseconds [109], so the observed result is to be expected.

7.3.3 Improvements and Future Plans

Although the ortho-positronium experiment was successful at measuring the lifetime of ortho-positronium within solid materials, the overall aim of the experiment was to measure the inherent lifetime of ortho-positronium as accurately as possible. In order to further reduce the effect of pick-off (which was still the main limiting factor of the set-up), two improvements to the set-up were decided upon. Firstly, a new ^{22}Na source was produced using a magnesium oxide crystal instead of aluminium, which results in reduced pick-off due to its ceramic nature compared to the metallic

structure of aluminium. Secondly, a purpose-designed fumed silica container was to be produced in order to place the fumed silica as close as possible to the source, reducing the effects of air between the two media.

The new ^{22}Na source was produced at the Birmingham MC40 cyclotron by irradiating a magnesium oxide crystal with a deuteron beam, inducing the ^{nat}Mg(d,x)^{22}Na reaction, predominantly from ^{24}Mg(d,α)^{22}Na, due to the dominant natural abundance of ^{24}Mg of 79%. A beam energy of 16.7 MeV was used as, after accounting for energy losses in the 25 μm Ti beam-line window ($\sim$ MeV) and the 0.5 mm thickness of the MgO crystal, the energy is reduced from 16.7 keV to $\sim$5.8 MeV. This energy is within a peak in the cross section of the aforementioned reaction [110]. The source production method was designed in order to produce a 20 kBq source which is required for good statistics, but is still suitable for use in an undergraduate laboratory.

The designing and testing of the new fumed silica container is currently in progress. As previously mentioned, the design of the container will place the fumed silica as close as possible to the source in order to reduce the effects of air between the two. This will be done by incorporating a slot, purpose-made for the source, for it to fit into when performing ortho-positronium measurements. It is hoped that, going forward, use of this container combined with the new source will allow for measurements of the ortho-positronium half-life closer to that of the vacuum value.

7.4 Discussion and Outcomes

Through this experiment, it has been shown that the lifetime of positrons in aluminium can be measured accurately using sources and equipment commonly available in undergraduate laboratories. The lifetime was found to be $203 \pm 1(\text{stat.})$ ps, compared to the known literature value of 211 ± 10 ps. This experiment has subsequently successfully been performed by undergraduate students, demonstrating how the experiment can be used to teach students both nuclear theory and also experimental nuclear physics skills.

The lifetime of ortho-positronium in this set-up has also been measured to be $12.3 \pm 0.1(\text{stat})$ ns. Although this is over an order of magnitude below the literature value of 142.0463 ± 0.0004 ns for the lifetime in a vacuum, this is to be expected as the ^{22}Na source used was contained within a ball of aluminium, and the experiment was not performed under vacuum. In solid materials the lifetime of ortho-positronium is expected to be of the order of a few nanoseconds, so this result can be seen as a success.

Another possible modification to the experiment in order to measure the lifetime of ortho-positronium is a four detector set-up, with one detector measuring the 1274.5 keV start signal and the other three detectors measuring the three gamma rays from the decay of the ortho-positronium [109]. A stop signal is only output if signals are received coincidentally on all three of these detectors. This greatly

reduces the number of background signals measured, but will require a much greater measurement time due to the much lower detection efficiency. This, combined with the increased equipment cost, may result in this set-up being unsuitable for an undergraduate laboratory.

Chapter 8

Summary and Conclusions

8.1 Summary and Outlook

Rhenium-190

In the main project detailed in this thesis, an experiment was performed in order to reduce the uncertainty in the atomic mass and mass excess of the neutron rich isotope ^{190}Re. This work was carried out at the Maier-Leibnitz Laboratory in Munich, using the 14 MV tandem Van de Graaff accelerator to produce an 18 MeV deuteron beam to induce both the ^{192}Os($\vec{d}$,α)^{190}Re and ^{194}Pt($\vec{d}$,α)^{192}Ir reactions. The α-particle ejectiles were subsequently detected by the Q3D magnetic spectrograph at a variety of different angles with respect to the beam axis. Alpha-particle-ejectile events were selected and for both reactions, energy spectra were plotted and fitted using a series of Gaussian distributions with a linear background. For the ^{192}Ir spectrum, peaks were assigned to known energy levels and subsequently a calibration between channel number given by the detector and residual nucleus excitation energy was found. Kinematic calculations were used to convert these values into the energies of the ejectile particles. Using the calibration, the difference in the positions in the ^{192}Ir and ^{190}Re spectra corresponding to zero excitation energy was found. This, combined with the difference in recoil energy of the two residual nuclei, was used to give the difference in Q-value between the two reactions. Subsequently, the mass excess and atomic mass of ^{190}Re were found, lying within the error bounds of the previous literature values but showing significant reduction in their uncertainty.

The reduction of the uncertainty in the atomic mass of nuclei synthesised in astrophysical processes, such as the r-process, to below $\pm 10\,\mathrm{keV}$ has been demonstrated to be important in order to prevent these uncertainties dominating over reaction rate uncertainties. As ^{190}Re is populated in the decays of nuclei produced by the r-process, the result of this work may be of importance for models of astrophysical processes. The reduced uncertainty in the mass may also lead to reduced uncertainties in any experiments, similar in structure to this one, involving ^{190}Re as a reactant.

The project also obtained more information about the energy-level structure of ^{190}Re. To do this, an extended section of the ^{190}Re excitation energy spectrum was fitted up to ~ 1 MeV. The ^{192}Ir calibration performed in the previous part of the study was initially used to assign an excitation energy to the observed levels. From this, three previously measured states in ^{190}Re, including the ground state, were identified. These were subsequently used to obtain an improved calibration with greater accuracy at higher excitation energies and was used to assign energies for each of the states, with errors, which are displayed in full in table 6.1. Although known states in ^{190}Re were observed, as discussed, the uncertainty in their excitation energies was not reduced in this study.

An attempt was also made to assign both spin and parity to each of the observed states in ^{190}Re. This was done by using information from both the experimental

set-up and the fitted ^{190}Re spectra, from which the experimental differential cross sections and analysing powers were extracted. These were then compared to theoretically calculated properties of these values for a variety of L-transfers, corresponding to different spin/parity configurations for the ^{190}Re recoil nucleus. To perform these calculations the program DWUCK4 was used, which utilises the distorted-wave Born approximation. Through these comparisons, the $J^{\pi} = 3^{-}$ assignment of the excited state at 119.12 ± 0.05 keV was preliminarily confirmed as the observed and calculated differential cross sections show good agreement, although more work is needed to rule out other spin and parity configurations. However, this was not the case for the analysing powers. For the other previously observed states in ^{190}Re, good agreement was not observed for the differential cross section or analysing power corresponding to any spin and parity configuration. It is thought that this is due to a combination of issues with the DWUCK4 optical model input parameters and also a lack of angular data.

Positrons and Positronium

This thesis also presented a side project involving the designing of an experiment to investigate the properties of positronium using equipment commonly available in an undergraduate nuclear physics laboratory. The first part of the project involved measuring the lifetime of positrons, produced via the β^{+} decay of ^{22}Na, in aluminium. A set of nuclear electronics modules were configured in order to measure the time between the production and the decay of positrons within aluminium.

The second part of this project involved measuring the lifetime of ortho-positronium within a solid. To achieve this, a similar set-up was used to measure the time between the production of the positron and the decay of the ortho-positronium. The apparatus was altered slightly to account for the fact that ortho-positronium most commonly decays into three photons, each with energies below 511 keV. The source holder was also modified, removing the aluminium casing and subsequently placing the source within a container of fumed silica, known to increase the formation of ortho-positronium and reduce an alternative decay channel called 'pick-off' where the positron in ortho-positronium annihilates with an external electron. The source material itself was still aluminium.

This experiment has subsequently been performed by undergraduate students as part of their nuclear physics laboratory module, focused on the measurement of positrons in aluminium. Improvements currently underway include production of a new, ceramic ^{22}Na source and a re-designed fumed silica container to surround it. These changes are anticipated to reduce pick-off and should yield a measurement of ortho-positronium longer than obtained in the previous work.

8.2 Conclusions

In the first study presented in this thesis, the atomic mass of the isotope ^{190}Re was measured to be $176948297 \pm 5\,\text{keV}$, corresponding to a mass excess of $-35583 \pm 5\,\text{keV}$. Compared to previous experiments, this represents an order of magnitude reduction in the uncertainty. This result has since been used to reduce the uncertainty the

Q-value of the β^- decay of ^{190}W into ^{190}Re, the β^- decay of ^{190}Re into ^{190}Os and the α-decay of ^{190}Re into ^{186}Ta as well as being used to reduce the uncertainties of the single proton and neutron separation energies for ^{190}Re.

As part of this study the ^{190}Re energy spectrum was also analysed. A total of 57 energy states in ^{190}Re were observed and fitted, the most comprehensive data to-date. For each state, differential cross section and analysing power plots have also been given. Although assignments of spin and parity were not successfully assigned to each of the states as part of this work, it has been demonstrated that the methods used in this study can be used to do so and it is hoped that the presented data will aid future spectroscopic studies into ^{190}Re.

The second project presented in this thesis focused on studying the lifetime of positrons in aluminium. The lifetime was measured to be $203 \pm 1(\text{stat.})$ ps, compared to the known literature value of 211 ± 10 ps. This particular experiment has also since been performed by undergraduate students as part of a teaching laboratory. The lifetime of ortho-positronium was also measured using a similar set-up. It was found to be $12.3 \pm 0.1(\text{stat})$ ns which, although over an order of magnitude below the literature value of 142.0463 ± 0.0004 ns for the lifetime in a vacuum, is to be expected as the measurement was performed within solid materials.

Appendix A

Recoil Energy Calculations

This appendix will demonstrate that the uncertainty in the literature value of the atomic mass of ^{190}Re previous to this study does not affect the recoil energy calculation for the ^{192}Os(d,α)^{190}Re reaction. The atomic mass values of the deuteron, α-particle, ^{190}Re and Os-192 taken from the 2016 atomic mass evaluation [64] are as follows:

$m_d = 2.01410177811 \pm 0.00000000012\,\mathrm{u}$,

$m_\alpha = 4.00260325413 \pm 0.00000000006\,\mathrm{u}$,

$m_{Os192} = 191.9614789 \pm 0.0000025\,\mathrm{u}$,

$m_{Re190} = 189.961740 \pm 0.000080\,\mathrm{u}$.

Here, u is an atomic mass unit ($\mathrm{u} = 931.494\,\mathrm{MeV/c^2}$). Assuming a beam energy of $E_d = 18\,\mathrm{MeV}$, an emission angle of $\theta = 20^\circ$ for the α-particle ejectiles and that ^{190}Re is produced in its ground state, these masses and a combination of equations given in both section 5.1.2 and this section can be used to find the recoil energy of the ^{190}Re nucleus. First, the energy of the α-particle ejectile for the reaction producing ^{192}Ir can be calculated using equation 5.11. The difference between this energy and the energy an α-particle ejectile corresponding to the reaction producing ^{190}Re is then found by comparing the position of the ^{190}Re ground-state and the zero-energy

point in the ^{192}Ir calibration as described in section 5.1.4. The momentum of the beam also needs to be calculated. This is trivial as the energy and mass of the beam are known. Overall, this gives the following momenta:

$p_d = \sqrt{2m_d E_d} = 259.88\,\mathrm{MeV/c},$

$p_\alpha = \sqrt{2m_\alpha E_\alpha} = 459.05\,\mathrm{MeV/c}.$

Next, an expression for p_{Re} in terms of the previously calculated p_d and p_α needs to be found. To do this, equations 5.9 and 5.10 from section 5.1.2 can be rearranged and squared to give the following equations:

$$p_3^2 \cos^2(\phi) = p_0^2 + p_2^2 \cos(\theta) - 2p_0 p_2 \cos(\theta), \tag{A.1}$$

$$p_3^2 \sin^2(\phi) = p_2^2 \sin(\theta). \tag{A.2}$$

Summing these equations can be used to remove the ϕ dependence and give an equation for p_3 in terms of p_0 and p_2 as desired

$$p_3^2 = p_0^2 + p_2^2 - 2p_0 p_2 \cos(\theta). \tag{A.3}$$

By applying this equation to the reaction and set-up used in this experiment (p_0 becomes p_d, p_2 becomes p_α and p_3 becomes p_{Re}), the momentum of the recoiling ^{190}Re nucleus, and therefore its energy, can easily be found:

$$p_{Re}^2 = p_d^2 + p_\alpha^2 - 2p_d p_\alpha \cos(\theta), \tag{A.4}$$

$$E_{Re} = \frac{p_{Re}^2}{2m_{Re}} = \frac{p_d^2 + p_\alpha^2 - 2p_d p_\alpha \cos(\theta)}{2m_{Re}}. \tag{A.5}$$

To show that the uncertainty in the literature value for the atomic mass of ^{190}Re prior to this study has a negligible effect on the recoil energy, this energy was calculated for several atomic mass values for ^{190}Re across the literature range. The results of this are shown in table A.1

Table A.1: Table showing how calculations for the recoil energy of the ^{190}Re nucleus vary over the literature range of atomic masses for ^{190}Re prior to this study. The previous centroid literature value for ^{190}Re [64] is shown in bold.

^{190}Re **Atomic Mass (u)**	$\boldsymbol{E_{Re}}$ **(MeV)**
189.961660	0.152743215
189.961680	0.152743199
189.961700	0.152743183
189.961720	0.152743166
189.961740	0.152743150
189.961760	0.152743134
189.961780	0.152743118
189.961800	0.152743102
189.961820	0.152743086

As can be seen from table A.1, the ^{190}Re recoil energy is stable at 0.152743 MeV over this uncertainty range, and therefore it was deemed suitable to use this value in further calculations of the atomic mass of ^{190}Re.

In the 2020 atomic mass evaluation [87], the atomic mass of the α-particle and ^{192}Os are unchanged from the 2016 edition. The atomic mass of the deuteron has changed, but to a degree that is insignificant for these calculations. The atomic mass

of ^{190}Re has changed significantly due to the results of this study. However, the new atomic mass is still within the range used in table A.1. Therefore the calculations performed in this section are still valid.

Appendix B

Publications and Presentations

Publications

- **M.R. Griffiths**, C. Wheldon, Tz. Kokalova, A. Turner, S. Pirrie, V. Ziman, N.I. Ashwood, J.D. Malcolm, M. Barr, M. Freer, Th. Faestermann, H-F. Wirth, R. Hertenberger, R. Gernhäuser, R. Krücken - Mass measurement of Re-190. *J. Phys. G*, **47**, 085104 (2020).

- M. Ćwiok, W. Dominik, A. Fijałkowska, M. Fila, Z. Janas, A. Kalinowski, K. Kierzkowski, M. Kuich, C. Mazzocchi, W. Okliński, M. Zaremba, M. Gai, D.K. Schweitzer, S.R. Stern, S. Finch, U. Friman-Gayer,S.R. Johnson, T.M. Kowalewski, D.L. Balabanski, C. Matei, A. Rotaru, K.C.Z. Haverson, R. Smith, R.A.M. Allen, **M.R. Griffiths**, S. Pirrie, and P. Santa Rita Alcibia - Studies of photo-nuclear reactions at astrophysical energies with an active-target TPC. *EPJ. Conf*, **279**, 04002 (2023).

Presentations

- 'Mass measurement of Re-190 using the Q3D Magnetic Spectrograph', Lockdown & Distancing Nuclear Physics Seminars - July 2020

- 'Reducing uncertainty in the atomic mass of Rhenium-190', Virtual Conference on Applied Radiation Metrology (vCARM) - November 2020

- 'Mass measurement and energy level analysis of 190-Re using the Q3D magnetic spectrograph', Institute of Physics Joint APP, HEPP and NP Conference - April 2021

- 'Spectroscopic analysis of Re-190 using the Q3D magnetic spectrograph', Institute of Physics UK Nuclear Physics Conference - April 2022

- 'Spectroscopic Analysis of the Energy-Level Structure in Re-190', International Nuclear Physics Conference - September 2022

Published Paper from this Work

OPEN ACCESS
IOP Publishing
Journal of Physics G: Nuclear and Particle Physics
J. Phys. G: Nucl. Part. Phys. **47** (2020) 085104 (5pp)
https://doi.org/10.1088/1361-6471/ab98e3

Mass measurement of Re-190

M R Griffiths[1,4], C Wheldon[1], Tz Kokalova[1], A Turner[1], S Pirrie[1], V Ziman[1], N I Ashwood[1], J D Malcolm[1], M Barr[1], M Freer[1], Th Faestermann[2], H-F Wirth[3], R Hertenberger[3], R Gernhäuser[2] and R Krücken[2]

[1] School of Physics and Astronomy, University of Birmingham, Birmingham, B15 2TT, United Kingdom
[2] Physik Department, Technische Universität München, D-85748 Garching, Germany
[3] Fakultät für Physik, Ludwig-Maximilians-Universität München, D-85748 Garching, Germany

E-mail: m.r.griffiths@pgr.bham.ac.uk

Received 7 April 2020, revised 21 May 2020
Accepted for publication 2 June 2020
Published 6 July 2020

Abstract

In this paper, a measurement of the atomic mass and mass excess of $^{190}_{75}$Re are presented. This isotope and $^{192}_{77}$Ir were produced at the Maier-Leibnitz Laboratory (MLL) in Munich in the ^{192}Os$(d, \alpha)^{190}$Re and ^{194}Pt$(d, \alpha)^{192}$Ir reactions. The Q3D magnetic spectrograph was used to measure the momenta of the α-particle ejectiles in order to reconstruct states in both ^{190}Re and ^{192}Ir. A mass calibration was performed using known energy levels in ^{192}Ir. These measurements were used to obtain a new value of the mass excess of ^{190}Re, -35583 ± 5 keV. The previously known literature value is -35640 ± 70 keV.

Keywords: $^{190}_{75}$Re atomic mass, $^{190}_{75}$Re mass excess, nuclear reaction ^{192}Os$(d, \alpha)^{190}$Re, Q3D magnetic spectrograph

(Some figures may appear in colour only in the online journal)

1. Introduction

The neutron-rich isotope $^{190}_{75}\mathrm{Re}_{115}$ lies on the decay path of nuclei populated in the astrophysical rapid neutron capture process (the *r*-process). Additionally, the mass ≈170–190 region of the nuclide chart is known for the occurrence of large numbers of metastable (isomeric) nuclear states caused by significant quadrupole deformations [1]. These *K*-isomers (so called due to

[4] Author to whom any correspondence should be addressed.

Original content from this work may be used under the terms of the Creative Commons Attribution 4.0 licence. Any further distribution of this work must maintain attribution to the author(s) and the title of the work, journal citation and DOI.

the large angular momentum projection, K, on the nuclear deformation axis) are deformation aligned states and experience hindered decays to the rotationally aligned nuclear ground state structures. The long lifetimes of some of these levels can form astrophysical waiting points at low excitation energies [2].

Rhenium-190 exhibits an isomeric state with $I^{\pi} = (6^{-})$, $t_{1/2} = 3.2 \pm 0.2$ h, observed at 204 ± 10 keV by Reed *et al* [3] at the Experimental Storage Ring (ESR) at GSI in Darmstadt. The ^{190}Re ground state has $I^{\pi} = (2^{-})$ and $t_{1/2} = 3.1 \pm 0.3$ min [4]. However, not only is there significant uncertainty in the excitation energy of the excited state, but the atomic mass of ^{190}Re is further uncertain by ± 70 keV [5]. Schatz [6] has pointed out the importance of determining masses to better than 10 keV for understanding astrophysical processes, as it means uncertainties in the mass do not dominate over reaction-rate uncertainties (reference [6] is focused on the *rp*-process, but this condition has also been shown to apply to other astrophysical processes, such as the *r*-process [7]). This allows production mechanisms to be more easily investigated. This paper details an experiment that has been performed to accurately measure the mass of ^{190}Re.

2. Experimental method

The experiment was performed using the Q3D magnetic spectrograph [8, 9] at the Maier-Leibnitz Laboratory (MLL) in Munich where ^{190}Re and ^{192}Ir, the latter an isotope with precise literature values for its mass and energy levels [5, 10, 11], were produced. This was done by bombarding targets of ^{192}Os and ^{194}Pt with an 18 MeV deuteron beam to induce the ^{192}Os$(d, \alpha)^{190}$Re and ^{194}Pt$(d, \alpha)^{192}$Ir reactions. The targets had thicknesses of 45 μg cm^{-2} (^{192}Os) and 66 μg cm^{-2} (^{194}Pt) and both were backed with 7 μg cm^{-2} of carbon. The beam was produced using the 14 MV tandem Van de Graaff accelerator at MLL with beam currents between 0.4 μA and 1.35 μA. The Q3D spectrograph was positioned at an angle of 20° to the beam axis in the horizontal plane and used to measure the energy of α-particle ejectiles, from which the energy of the recoiling binary partner nuclei could be inferred. The magnetic optical properties of the Q3D are such that the particles corresponding to a given excitation energy are focused to the same point on the focal plane, independent of angle. Therefore, position on the focal plane corresponds to excitation energy of the unobserved recoil particle. For this experiment, the Q3D was set so that excitation energy in ^{190}Re, $E_x^{\mathrm{Q3D}} = 400$ keV, was focused on the focal plane with an acceptance range of approximately -300–600 keV to ensure the low-lying states in ^{192}Ir were detectable using approximately the same magnetic field settings. The magnetic fields of the Q3D were set for the ^{192}Os$(d, \alpha)^{190}$Re reaction throughout the whole experiment.

3. Results

The resonance peaks in the energy spectra of ^{190}Re and ^{192}Ir have been fitted with Gaussian functions, as shown in figure 1. Due to properties of the Q3D the low energy peaks in ^{190}Re are skewed and therefore these peaks have been fitted as skewed Gaussian functions. Higher energy peaks in the ^{190}Re spectrum have also been identified, but are not the focus of this work. Due to the high level density in some regions of the ^{192}Ir spectrum, it was not possible to assign exact energies to all of the peaks as they contain contributions from multiple resonance components that could not be deconvolved. Such peaks do not contribute to the calibration and their fitted energies are shown in brackets in figure 1. The peak widths of about 10 keV full width at half maximum (FWHM) are dominated by experimental resolution, the most significant contribution to which are the energy-loss differences of α-particle ejecticles due to the target thickness. The difference in the ejectile energy corresponding to the ground states

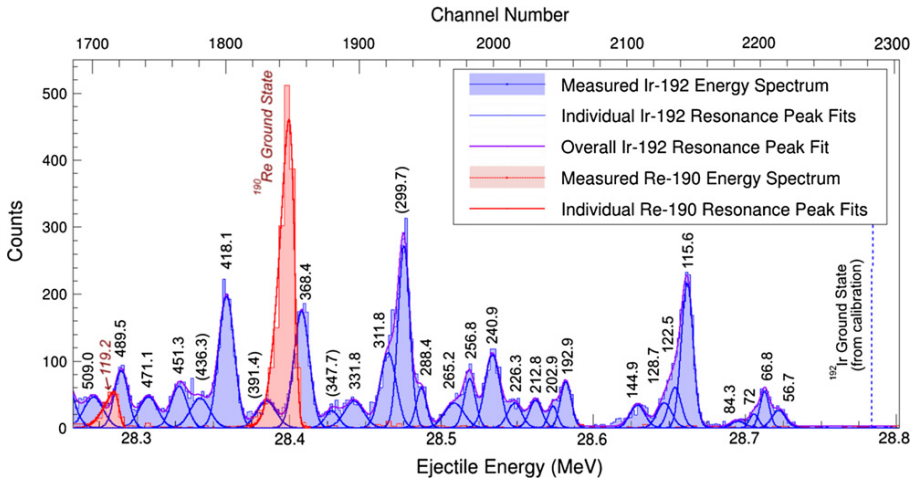


Figure 1. Fitted low energy region of the ^{192}Ir energy spectrum, with the excitation energies of peaks used in the calibration labelled in keV and those omitted due to comprising of multiple close-lying resonances labelled in brackets [11, 13]. The plot shows both the ejectile (α-particle) energy and the corresponding channel number for the focal plane detector on the x-axes. Here, a higher value of channel number corresponds to a lower excitation energy since ejectile energy is being measured. The fitted ground-state and first excited-state peaks in ^{190}Re have been overlaid and labelled in red. The ground-state position of ^{192}Ir (found using the calibration) is also indicated, but was not populated due to its $I^{\pi} = 4^{+}$ configuration being incompatible with the ^{194}Pt target ground-state configuration.

was added to the difference in recoil energy between the two nuclei to give the difference between the Q-values of the reactions used to produce the two nuclei. Using this value, along with known mass excesses [5] for all other isotopes involved in the reactions, a value for the mass excess of ^{190}Re can be found as

$$\Delta M_{\mathrm{Re}} = \Delta Q_{\mathrm{Ir-Re}} - \Delta M_{\mathrm{Pt}} + \Delta M_{\mathrm{Os}} + \Delta M_{\mathrm{Ir}}. \tag{1}$$

Here, ΔM_{Re}, ΔM_{Pt}, ΔM_{Os} and ΔM_{Ir}, represent the mass excesses of ^{190}Re, ^{194}Pt, ^{192}Os and ^{192}Ir, respectively, with ΔQ representing the difference in Q-value between the ^{192}Ir and ^{190}Re reactions. This is the difference in energy between the α-particle ejectiles corresponding to the respective ground states, shown in figure 1, added to the difference between the recoil energy of ^{192}Ir and ^{190}Re. Defining the position of the ^{192}Ir ground state to correspond to an excitation energy of 0 keV gives the position of the ^{190}Re ground state peak as 373 ± 4 keV. Through non-relativistic two-body kinematic calculations, the difference in recoil energy between the ^{192}Ir and ^{190}Re nuclei was found to be 2.1 keV with negligible error compared to the uncertainty in the difference between ground state energies. Therefore, the difference in Q-value between the two reactions was found to be $\Delta Q_{\mathrm{Ir-Re}} = 375 \pm 4$ keV overall. This Q-value difference was then used to calculate information such as the binding energy per nucleon and the atomic mass of ^{190}Re. The values for the parameters used in equation (1) are shown in table 1.

In figure 1, the first excited state in ^{190}Re can also be seen. The fitted energy of this state is found to be 119.2 ± 0.7 keV, compared to the current literature value of 119.12 ± 0.05 [4]. Another noteworthy state is the low lying $I^{\pi} = 1^{-}$, 56.72 keV energy level in ^{192}Ir. This corresponds to the well studied $^{192\mathrm{m1}}$Ir isomeric state [12].

Table 1. Values used to calculate the mass excess of ^{190}Re using equation (1). The value for $\Delta Q_{\mathrm{Ir-Re}}$ was found in this experiment, with the mass excess values taken from literature [5].

$\Delta Q_{\mathrm{Ir-Re}}$ (keV)	ΔM_{Pt} (keV)	ΔM_{Os} (keV)	ΔM_{Ir} (keV)
375 ± 4	-34760.1 ± 0.5	-35882.2 ± 2.3	-34835.6 ± 1.3

Table 2. Properties of ^{190}Re measured in this experiment compared to known literature values [5].

	Mass excess (keV)	Atomic mass (keV)	Atomic mass (μu)	Binding energy per nucleon (keV)
Current work	$-35\,583 \pm 5$	$176\,948\,297 \pm 5$	$189\,961\,800 \pm 5$	7949.78 ± 0.03
Literature	$-35\,640 \pm 70$	$176\,948\,240 \pm 70$	$189\,961\,740 \pm 80$	7950.1 ± 0.4

In table 2 the results of this experiment are shown alongside the previously known literature values. It is clear that the newly obtained quantities all lie within the error bars of the previous values suggesting that there is good agreement between the two sets of results. It is also evident that the uncertainty has been reduced greatly and is now an order of magnitude lower compared to previous values. This is not only true for the measurement of the mass excess but also, by definition, for the atomic mass and binding energy per nucleon.

3.1. Uncertainty

The uncertainties on the mass excesses of the other nuclei used in this experiment, ^{192}Ir, ^{192}Os and ^{194}Pt, are 1.3 keV, 2.3 keV and 0.5 keV, respectively [5]. As can be seen in equation (1), the uncertainty on the ^{190}Re mass excess depends on these three values, with the larger uncertainty for ^{192}Os being most significant. Errors also arise due to the manner in which the difference in Q-value is found. In the experiment the ground state in ^{192}Ir was not populated and, as the mass measurement relies on knowing the difference in measured energy between the ground states in ^{192}Ir and ^{190}Re, the ^{192}Ir ground state was found by extrapolating the calibration beyond the peaks used to produce the calibration itself, as the ^{192}Ir ground state lies at a higher channel number than any peak observed in this experiment. An alternative method, which does not involve extrapolation, is to find the difference in energy between the first excited state in ^{192}Ir, the $^{192\mathrm{m1}}$Ir isomeric state at 56.72 ± 0.01 keV [12], and the ^{190}Re ground-state. However, due to the introduction of the uncertainty on the energy of this state and the fitted centroid value of the corresponding peak, this method does not lead to an overall reduction in uncertainty. The extrapolation introduces uncertainty in the position of the ^{192}Ir ground state which is then propagated into the uncertainty in the difference in Q-value between the reactions.

The calibration was performed using ^{192}Ir as it behaves in a similar manner to ^{190}Re in the Q3D spectrograph due to the two nuclei having similar nucleon numbers and their ability to be produced in the same (d, α) reaction. However, the ^{192}Ir level scheme is complex with high level density in some regions, as seen in figure 1. This, along with relatively low statistics, means the ^{192}Ir spectrum is not ideal for performing a calibration and therefore uncertainty is introduced by the calibration as the peaks used to produce the calibration often have significant uncertainty in their centroid position. This uncertainty is then transferred to the calibration in the form of upper and lower bounds for energy values found using the calibration. Additionally, the fit of the ^{190}Re ground state yields a centroid value with an associated uncertainty. Both of

these factors contribute to the uncertainty in the Q-value difference between the two reactions, which is found to be 375 ± 4 keV as stated above. Therefore, the dominant uncertainties in this experiment are the error in the difference between the Q-values and the error in the mass excess of ^{192}Os.

As previously mentioned, the uncertainty in the calculation of the mass excess of ^{190}Re depends on known uncertainties in the values of the mass excesses of ^{192}Os, ^{192}Ir and ^{194}Pt as well as experimental uncertainties. Therefore, the uncertainty in the mass excess measurement of ^{190}Re measured here is larger, but of the same order of magnitude, compared to other nuclei that lie in the same mass region as ^{190}Re.

As a consequence of this measurement of the ground-state mass, overall uncertainty in the mass of the $I^{\pi} = (6^{-})$ isomeric state has been correspondingly reduced. This can be included in astrophysical network calculations such as the Brussels Nuclear Library (BRUSLIB) [14].

4. Conclusion

The atomic mass of the isotope ^{190}Re has been measured as 176 948 297 ± 5 keV corresponding to a mass excess of −35 583 ± 5 keV. This represents an order of magnitude reduction in the uncertainty compared to previous experiments.

Acknowledgments

The authors would like to thank the operators of the tandem Van de Graaff accelerator at the Maier-Leibnitz Laboratory in Munich for providing a stable deuteron beam. This work has been supported through UK STFC Grant Nos. ST/E500651/1 and ST/F011989/.

ORCID iDs

M R Griffiths https://orcid.org/0000-0002-2962-113X
C Wheldon https://orcid.org/0000-0001-9137-6051
M Freer https://orcid.org/0000-0001-5439-5579
Th Faestermann https://orcid.org/0000-0002-6603-8787

References

[1] Walker P M and Dracoulis G D 1999 *Nature* **399** 35–40
[2] Reifarth R, Lederer C and Käppeler F 2014 *J. Phys.* G **41** 053101
[3] Reed M W *et al* 2012 *Phys. Rev.* C **86** 054321
[4] Singh B 2003 *Nucl. Data Sheets* **99** 275–481
[5] Wang M *et al* 2017 *Chin. Phys.* C **41** 030003
[6] Schatz H 2006 *Int. J. Mass Spectrom.* **251** 293–9
[7] Martin D *et al* 2016 *Phys. Rev. Lett.* **116** 121101
[8] Wiedner C A *et al* 1972 *Nucl. Instrum. Methods* **105** 205–10
[9] Löffler M, Scheerer H J and Vonach H 1973 *Nucl. Instrum. Methods* **111** 1–12
[10] Garrett P E and Burke D G 1994 *Nucl. Phys.* A **568** 445–98
[11] Baglin C M 2012 *Nucl. Data Sheets* **113** 1871–2111
[12] Audi G *et al* 2017 *Chin. Phys.* C **41** 030001
[13] Balodis M and Krasta T 2014 *Nucl. Phys.* A **933** 189–211
[14] Xu Y *et al* 2013 *Astron. Astrophys.* **549** A106

Bibliography

[1] G. Sterman. Quantum Chromodynamics. In *Encyclopedia of Mathematical Physics*. Academic Press (2006).

[2] R.D. Woods and D.S. Saxon. Diffuse surface optical model for nucleon-nuclei scattering. *Phys. Rev.*, **95**, 577–578 (1954).

[3] M.R. Pahlavani. The Nuclear Mean Field Theory and Its Application to Nuclear Physics. In *Selected Topics in Applications of Quantum Mechanics*. IntechOpen (2015).

[4] B.Blank and P.H.Regan. Magic and Doubly-Magic Nuclei. *Nucl. Phys. News*, **11**, 15–22 (2001).

[5] K. S. Krane. Introductory Nuclear Physics. John Wiley and Sons, 3rd edition (1988).

[6] M. G. Mayer. Nuclear Configurations in the Spin-Orbit Coupling Model. I. Empirical Evidence. *Phys. Rev.*, **78**, 16–21 (1950).

[7] Tz. Kokalova. Gamma-ray spectroscopy of deformed states in light nuclei and cluster emission. PhD thesis, Freie Universität Berlin (2003).

[8] P.E.Hodgson. Nuclear structure. *Contemp. Phys.*, **35**(5), 329–346 1994.

[9] F.G. Kondev et al. The NUBASE2020 evaluation of nuclear physics properties. *Chin. Phys. C*, **45**(3), 030001 (2021).

[10] P. M. Walker and Z. Podolyák. 100 years of nuclear isomers — then and now. *Physica Scripta*, **95**, 044004 (2020).

[11] C. F. v. Weizsäcker. Metastabile Zustände der Atomkerne. *Naturwissenschaften*, **24**, 813–814 (1936).

[12] S. Mukhopadhyay et al. Coexisting shape- and high-K isomers in the shape transitional nucleus 188Pt. *Phys. Lett. B*, **739**, 462–467 (2014).

[13] P. M. Walker and G. D. Dracoulis. Energy traps in atomic nuclei. *Nature*, **399**, 35–40 (1999).

[14] T. Ruen. Oblate and prolate spheroid examples. Available at `https://commons.wikimedia.org/wiki/File:Spheroids.svg`. Accessed 12/05/23.

[15] I.Ragnarsson and S.V.Nilsson. Shapes and Shells in Nuclear Structure. Cambridge University Press (1995).

[16] M. P. Fewell. The atomic nuclide with the highest mean binding energy. *Am. J. Phys.*, **63**, 653–658 (1995).

[17] N. Ghahramany, S. Gharaati, and M. Ghanaatian. New approach to nuclear binding energy in integrated nuclear model. *J. Theor. Appl. Phys.*, **8**, 97–106 01 (2012).

[18] G. Gamow. Mass defect curve and nuclear constitution. *Proc. R. Soc. Lond.*, **126**(803), 632–644 (1930).

[19] C. F. v. Weizsäcker. Zur Theorie der Kernmassen. *Zeitschrift für Physik*, **96**(7), 431–458 (1935).

[20] J.W. Rohlf. Modern Physics from alpha to Z0. Wiley (1994).

[21] P. Möller et al. Nuclear ground-state masses and deformations. *At. Data Nucl. Data Tables*, **59**(2), 185–381 (1995).

[22] R.F. Casten. The Deformed Shell Model or Nilsson Model. In *Nuclear Structure from a Simple Perspective*. Oxford University Press (2001).

[23] X-H. Xiang and X-T. He. Backbendings of Superdeformed bands in ^{36,40}Ar. *Chin. Phys. C*, **42** 02 (2018).

[24] W. E. Burcham. Elements of Nuclear Physics. Longman, 1st edition (1979).

[25] M. Gómez-Ramos, A. Obertelli, and Y. L. Sun. Breakup reactions and their ambiguities. *Eur. Phys. J. A*, **57**(4), 148 (2021).

[26] H. Feshbach. Theoretical Nuclear Physics: Nuclear Reactions. Theoretical Nuclear Physics. Wiley, 2nd edition (1992).

[27] N. Bohr. Neutron Capture and Nuclear Constitution. *Nature*, **137**(3461), 344–348 (1936).

[28] M. Balodis et al. Transfer and neutron capture reactions to ^{194}Ir as a test of $u_\nu(6/12) \bigotimes u_\pi(6/4)$ supersymmetry. *Phys. Rev. C*, **77**, 064602 (2008).

[29] F. Luoni et al. Total nuclear reaction cross-section database for radiation protection in space and heavy-ion therapy applications. *New J. Phys.*, **23**(10), 101201 (2021).

[30] P. E. Hodgson. The nuclear optical model introductory overview. Technical report, *Oxford Univ. Nucl. Phys.*, (1996).

[31] W.H. Dickhoff and R.J. Charity. Recent developments for the optical model of nuclei. *Prog. Part. Nucl. Phys.*, **105**, 252–299 (2019).

[32] C.M. Perey and F.G. Perey. Compilation of phenomenological optical-model parameters 1969–1972. *At. Data Nucl. Data Tables*, **13**(4), 293–337 (1974).

[33] P. E. Garrett and D. G. Burke. Nuclear structure of ^{192}Ir studied with direct transfer reactions. *Nuclear Physics A*, **568**, 445 – 498 (1994).

[34] I. J. Thompson and F. M. Nunes. Nuclear Reactions for Astrophysics: Principles, Calculation and Applications of Low-Energy Reactions. Cambridge University Press (2009).

[35] P. D. Kunz and E. Rost. The Distorted-Wave Born Approximation, pages 88–107. Springer New York (1993).

[36] R. Capote et al. RIPL – Reference Input Parameter Library for Calculation of Nuclear Reactions and Nuclear Data Evaluations. *Nucl. Data Sheets*, **110**, 3107 – 3214 (2009).

[37] F. Hoyle. On Nuclear Reactions Occuring in Very Hot Stars. I. the Synthesis of Elements from Carbon to Nickel. *Astrophys. J. Suppl.*, **1**, 121 (1954).

[38] M. Freer and H.O.U. Fynbo. The Hoyle state in 12C. *Prog. Part. Nucl. Phys.*, **78**, 1–23 (2014).

[39] C. Battistini and T. Bensby. The origin and evolution of r- and s-process elements in the Milky Way stellar disk. *Astron. Astrophys.*, **586**, A49 (2016).

[40] M. Arnould and S. Goriely. The p-process of stellar nucleosynthesis: astrophysics and nuclear physics status. *Phys. Rep.*, **384**, 1 – 84 (2003).

[41] T. Rauscher. Origin of the p-Nuclei in Explosive Nucleosynthesis. *Proc. Sci.*, **NIC XI**, 059 (2010).

[42] T. Kajino et al. Current status of r-process nucleosynthesis. *Prog. Part. Nucl. Phys.*, **107**, 109–166 (2019).

[43] I. Panov and I.Y. Korneev. Fission recycling in the r-process and formation of the second peak with A $\sim$ 130. *International Symposium on Nuclear Astrophysics - Nuclei in the Cosmos, Proceedings* (2006).

[44] J. Cowan and F. Thielemann. R-Process Nucleosynthesis in Supernovae. *Phys. Today*, **57**, 47–53 (2004).

[45] P. Möller et al. Nuclear ground-state masses and deformations: FRDM(2012). *At. Data Nucl. Data Tables*, **109-110**, 1–204 (2016).

[46] H. Schatz. The importance of nuclear masses in the astrophysical rp-process. *Int. J. Mass Spectrom.*, **251**(2), 293 – 299 (2006).

[47] D. Martin et al. Impact of nuclear mass uncertainties on the r-process. *Phys. Rev. Lett.*, **116**, 121101 (2016).

[48] Jean Blachot. Nuclear Data Sheets for A = 108. *Nucl. Data Sheets*, **91**, 135–296 (2000).

[49] G. Wendell Misch et al. Astromers: Nuclear Isomers in Astrophysics. *Astrophys. J., Suppl. Ser.*, **252**(1), 2 (2020).

[50] A.H.W. Aten Junior and G.D. De Feyfer. Rhenium 190. *Physica*, **21**(1), 543 (1954).

[51] G. B. Baró and J Flegenheimer. A 2.8 Hour Rhenium Isotope. *Radiochim. Acta*, **1**, 2 – 3 (1962).

[52] P. E. Haustein and A.F. Voigt. The decay of 3.1 min 190Re. *Nucl. Phys. A*, **136**, 414 – 422 (1969).

[53] S.W. Yates et al. Levels of ^{190}Os populated in the decays of 3.3 h ^{190m}Re and 12d ^{190}Ir and in the ^{189}Os$(d,p)^{190}$Os reaction. *Nucl. Phys. A*, **222**(2), 276–300 (1974).

[54] P. E. Haustein et al. New neutron-rich isotope: ^{190}W. *Phys. Rev. C*, **14**, 645–649 (1976).

[55] B. Singh and J. Chen. Nuclear Data Sheets for A=190. *Nucl. Data Sheets*, **169**, 1–390 (2020).

[56] L.A. König, J.H.E. Mattauch, and A.H. Wapstra. 1961 nuclidic mass table. *Nucl. Phys.*, **31**, 18–42 (1962).

[57] J.H.E. Mattauch, W. Thiele, and A.H. Wapstra. 1964 atomic mass table. *Nucl. Phys.*, **67**(1), 1–31 (1965).

[58] A.H. Wapstra and N.B. Gove. The 1971 atomic mass evaluation: Part I. Atomic mass table. *At. Data Nucl. Data Tables*, **9**(4), 267–301 (1971).

[59] A.H. Wapstra and K. Bos. The 1977 atomic mass evaluation: Part I. Atomic mass table. *At. Data Nucl. Data Tables*, **19**(3), 177–214 (1977).

[60] A.H. Wapstra and G. Audi. The 1983 atomic mass evaluation: Part I. Atomic mass table. *Nucl. Phys. A*, **432**(1), 1–54 (1985).

[61] G. Audi and A.H. Wapstra. The 1993 atomic mass evaluation: Part I. Atomic mass table. *Nucl. Phys, A*, **565**(1), 1–65 (1993).

[62] G. Audi, A.H. Wapstra, and C. Thibault. The AME2003 atomic mass evaluation: (II). Tables, graphs and references. *Nucl. Phys. A*, **729**(1), 337–676 (2003).

[63] M. Wang et al. The AME2012 atomic mass evaluation. *Chin. Phys. C*, **36**(12), 1603 (2012).

[64] M. Wang et al. The AME2016 atomic mass evaluation (II). Tables, graphs and references. *Chin. Phys. C*, **41**(3), 030003 (2017).

[65] J. Luo et al. Activation cross sections for ^{190}Os$(n,p)^{190m,g}$Re, ^{188}Os$(n,p)^{188}$Re and ^{190}Os$(n,n')^{190m}$Os reactions from 13.5 to 14.8MeV. *Nucl. Instrum. Methods Phys. Res.*, **267**(7), 1051–1055 (2009).

[66] P. M. Walker and F. R. Xu. Shapes of neutron-rich $A\approx$190 odd-odd nuclei. *Phys. Rev. C*, **74**, 067303 (2006).

[67] M. W. Reed et al. Long-lived isomers in neutron-rich Z=72-76 nuclides. *Phys. Rev. C*, **86**, 054321 (2012).

[68] B. Franzke. The heavy ion storage and cooler ring project ESR at GSI. *Nucl. Instrum. Methods Phys. Res.*, **24-25**, 18–25 (1987).

[69] Y. Xu et al. Databases and tools for nuclear astrophysics applications BRUSsels Nuclear LIBrary (BRUSLIB), Nuclear Astrophysics Compilation of REactions II (NACRE II) and Nuclear NETwork GENerator (NETGEN). *Astron. Astrophys.*, **549**, A106 (2013).

[70] C. M. Baglin. Nuclear Data Sheets for A = 192. *Nucl. Data Sheets*, **113**, 1871 – 2111 (2012).

[71] M. Löffler, H. J. Scheerer, and H. Vonach. The ion optical properties of the Munich Q3D-spectrograph investigated by means of a special experimental ray tracing method. *Nucl. Instr. and Meth.*, **111**, 1 – 12 (1973).

[72] C. A. Wiedner et al. Performance of a QDDD spectrograph. *Nucl. Instr. and Meth.*, **105**, 205–210 (1972).

[73] R. Hertenberger et al. The Stern–Gerlach polarized ion source for the Munich MP-tandem laboratory, a bright source for unpolarized hydrogen and helium ion beams as well. *Nucl. Instrum. Methods Phys. Res.*, **536**(3), 266–272 (2005).

[74] R.J. Van de Graaff. Tandem electrostatic accelerators. *Nucl. Instrum. and Meth.*, **8**(2), 195–202 (1960).

[75] F. Hinterberger. Electrostatic accelerators. *CAS 2005 - CERN Accelerator School: Small Accelerators, Proceedings* (2006).

[76] G. Dollinger and Th. Faestermann. Physics at the Munich Tandem Accelerator Laboratory. *Nucl. Phys. News*, **28**(1), 5–12 (2018).

[77] H.-F. Wirth. Bau eines hochauflösenden Fokalebenendetektors für den Münchner Q3D-Magnetspektrographen Untersuchungen zur Kernstruktur von ^{129}Te. PhD thesis, Technischen Universität München (2001).

[78] B. Rebeiro et al. Spectroscopy of low lying states in ^{136}Cs. *J. Phys. Conf.*, **689**, 012026 (2016).

[79] J. Ott et al. A position sensitive cathode strip detector with single strip readout. *Nucl. Instrum. Methods Phys. Res.*, **367**, 280–284 (1995).

[80] R.Lutter et al. MARaBOU: MBS and ROOT based Online/Offline Utility. Available at `https://www-old.mll-muenchen.de/marabou/htmldoc/` (Accessed: 12/05/2023).

[81] S.M.Singer. Sunsort reference manual. Available at `http://npg.dl.ac.uk/MIDAS/manual/SunSort/` (Accessed: 12/05/2023).

[82] P. Sigmund. Particle Penetration and Radiation Effects. Springer Berlin (2006).

[83] C. Wheldon and Tz. Kokalova. *ckin* – Two-Body Kinematics Program. (2020).

[84] A. Azzalini and A. Dalla Valle. The Multivariate Skew-Normal Distribution. *Biometrika*, **83**(4), 715–726 (1996).

[85] M. Balodis and T. Krasta. Levels of two-particle and gamma bands in 192Ir. *Nucl. Phys. A*, **933**, 189 – 211 (2014).

[86] M. R. Griffiths et al. Mass measurement of Re-190. *J. Phys. G: Nucl. Part. Phys.*, **47**, 085104 (2020).

[87] M. Wang et al. The AME 2020 atomic mass evaluation (II). Tables, graphs and references. *Chin. Phys. C*, **45**(3), 030003 (2021).

[88] G. Savard and G. Werth. Precision nuclear measurements with ion traps. *Annual Review of Nuclear and Particle Science*, **50**(1), 119–152 (2000).

[89] R. Krücken. Private communication. .

[90] M.R. Griffiths. *PyDwuck* – A DWUCK4 Input File Generator. (2023).

[91] C. M. Perey and F. G. Perey. Deuteron Optical-Model Analysis in the Range of 11 to 27 MeV. *Phys. Rev.*, **132**, 755–773 (1963).

[92] L. McFadden and G.R. Satchler. Optical-model analysis of the scattering of 24.7 MeV alpha particles. *Nucl. Phys.*, **84**(1), 177–200 (1966).

[93] A. Czarnecki. Positronium properties. *Acta Phys. Polon. B*, **30**, 3837–3847 (1999).

[94] A. Czarnecki and S.G. Karshenboim. Decays of positronium. *14th International Workshop on High-Energy Physics and Quantum Field Theory (QFTHEP 99),* 538–544, (1999).

[95] S.G. Karshenboim. Precision study of positronium: Testing bound state QED theory. *Int. J. Mod. Phys. A*, **19**(23), 3879–3896 (2004).

[96] A. H. Al-Ramadhan and D. W. Gidley. New precision measurement of the decay rate of singlet positronium. *Phys. Rev. Lett.*, **72**, 1632–1635 (1994).

[97] O. Jinnouchi, S. Asai, and T. Kobayashi. Precision measurement of orthopositronium decay rate using SiO2 powder. *Phys. Lett. B*, **572**(3-4), 117–126 (2003).

[98] P Moskal et al. Feasibility study of the positronium imaging with the J-PET tomograph. *Phys. Med. Biol.*, **64**(5), 055017 (2019).

[99] K. Wada et al. Pick-off quenching probability of ortho-positronium per collision with atoms and molecules. *Eur. Phys. J. D*, **66**, 108 (2012).

[100] M.S. Basunia. Nuclear Data Sheets for A = 22. *Nucl. Data Sheets*, **127**, 69–190 (2015).

[101] P. Guss et al. CeBr3 as a room-temperature, high-resolution gamma-ray detector. *Nucl. Instrum. Meth. Phys. Res*, **608**(2), 297–304 (2009).

[102] Hamamatsu. Datasheet: Photomultiplier Tubes R13478, R13449, R13408, R13089, R1560, (2020).

[103] J. Beaman and J. Lloyd-Evans. Timing Jitter from Photomultiplier Signal Discriminators. *23rd International Cosmic Ray Conference (ICRC23)*, **2**, 615 (1993).

[104] D. Binkley. Development and Analysis of Non-Delay-Line Constant-Fraction Discriminator Timing Circuits, Including a Fully-Monolithic CMOS Implementation. PhD thesis, University of Tennessee (1992).

[105] S. Ament, J. Gregoire, and C. Gomes. Exponentially-modified gaussian mixture model: Applications in spectroscopy. Available at `https://arxiv.org/abs/1902.05601` (Accessed: 12/05/2023), (2019).

[106] J.L. Rodda II. Positron Mean Lives in Metals. *Retrospective Theses and Dissertations.* Iowa State University (1963).

[107] R. Paulin and G. Ambrosino. Annihilation libre de l'ortho-positonium formé dans certaines poudres de grande surface spécifique. *J. Phys. France*, **29**(4), 263–270 (1968).

[108] L. Liszkay et al. Positron annihilation in latex-templated macroporous silica films: pore size and ortho-positronium escape. *New J. Phys.*, **14**(6), 065009 (2012).

[109] J. Engbrecht and N. Hillson. A flexible positron spectrometer for the undergraduate laboratory. *Am. J. Phys.*, **86**(7), 549–558 (2018).

[110] A. Hermanne et al. Excitation functions for 7Be, 22,24Na production in Mg and Al by deuteron irradiations up to 50MeV. *Appl. Radiat. Isot.*, **70**(12), 2763 (2012).